# CZECH TECHNICAL UNIVERSITY IN PRAGUE

# FACULTY OF NUCLEAR SCIENCES AND PHYSICAL ENGINEERING

Department of Physics
Study programme: Nuclear and Particle Physics

MASTER THESIS

# Quantum tomography of the two-lepton system with ALICE

Author:       Bc. Sára Haidlová
Supervisor:   Mgr. Michal Broz, Ph.D.
Year:         2023

# ČESKÉ VYSOKÉ UČENÍ TECHNICKÉ V PRAZE

# FAKULTA JADERNÁ A FYZIKÁLNĚ INŽENÝRSKÁ

Katedra fyziky

Studijní program: Jaderná a částicová fyzika

DIPLOMOVÁ PRÁCE

# Kvantová tomografie systému dvou leptonů na experimentu ALICE

| | |
|---|---|
| Vypracovala: | Bc. Sára Haidlová |
| Vedoucí práce: | Mgr. Michal Broz, Ph.D. |
| Rok: | 2023 |

FAKULTA JADERNÁ A FYZIKÁLNĚ INŽENÝRSKÁ

KATEDRA FYZIKY

# ZADÁNÍ DIPLOMOVÉ PRÁCE

**Akademický rok:** 2022/2023

*Student:*      Bc. Sára Haidlová

*Studijní program:*      Jaderná a částicová fyzika

*Název práce:*
*(česky)*      Kvantová tomografie systému dvou leptonů na experimentu ALICE

*Název práce:*
*(anglicky)*      Quantum tomography of the two-lepton system with ALICE

*Jazyk práce:*      Angličtina

*Pokyny pro vypracování:*

1) Zpracujte rešerši těchto témat:

a) Kvantová tomografie v částicové fyzice

b) Charakteristika UPC

c) Experiment ALICE na urychlovači LHC

2) Aplikujte metody kvantové tomografie na Pb-Pb data z experimentu ALICE

a) Studujte výtěžek koherentní a nekoheretní fotoprodukce

b) Studujte Monte Carlo simulace pro koherentní a nekohoretní fotoprodukce J/Psi pro různé polarizace mezonu

c) Studujte efektivitu a akceptanci

*Doporučená literatura:*

[1] K. Aamodt et al. (ALICE Collaboration) The ALICE experiment at the CERN LHC, JINST 3 (2008) S08002

[2] J.G. Contreras, J. D. Tapia Takaki: Ultra-peripheral heavy-ion collisions at the LHC, International Journal of Modern Physics A 30(8), 1542012 (2015).

[3] S. Acharya et al. (ALICE Collaboration), Coherent J/ψ and ψ' photoproduction at midrapidity in ultra-peripheral Pb-Pb collisions at √sNN = 5.02 TeV, Eur. Phys. J. C (2021) 81:712

[4] J.C.Martens, J.P.Ralston and J.D.T.Takaki, Quantum tomography for collider physics: Illustrations with lepton pair production, Eur. Phys. J. C 78 (2018) no.1, 5

[5] Y.Afik and J.R.M.de Nova, Entanglement and quantum tomography with top quarks at the LHC, Eur. Phys. J. Plus 136 (2021) no.9, 907

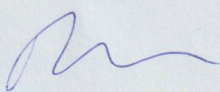*Jméno a pracoviště vedoucího diplomové práce:*

Mgr. Michal Broz, Ph.D.

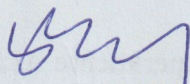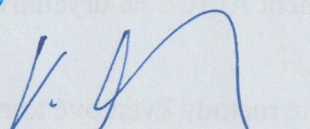Katedra fyziky, Fakulta jaderná a fyzikálně inženýrská ČVUT v Praze

*Datum zadání diplomové práce:*　　　20.10.2022

*Termín odevzdání diplomové práce:*　　03.05.2023

*Doba platnosti zadání je dva roky od data zadání.*

.............................................
*garant studijního programu*

....................................　　　　　　　....................................
*vedoucí katedry*　　　　　　　　　　　　　　　*děkan*

*V Praze dne*　　20.10.2022

# ČESKÉ VYSOKÉ UČENÍ TECHNICKÉ V PRAZE

Fakulta jaderná a fyzikálně inženýrská

Břehová 7
115 19 Praha 1



# PROHLÁŠENÍ

Já, níže podepsaný

| | |
|---|---|
| *Jméno a příjmení studenta:* | Sára Haidlová |
| *Osobní číslo:* | 486339 |
| *Název studijního programu (oboru):* | Jaderná a částicová fyzika |

prohlašuji, že jsem diplomovou práci s názvem:

**Kvantová tomografie systému dvou leptonů na experimentu ALICE**

vypracoval(a) samostatně a uvedl(a) veškeré použité informační zdroje v souladu s Metodickým pokynem o dodržování etických principů při přípravě vysokoškolských závěrečných prací.

V Praze dne 3.5.2023

.................................................
podpis

**Acknowledgments**

<div align="right">Bc. Sára Haidlová</div>

*Název práce:*

**Kvantová tomografie systému dvou leptonů na experimentu ALICE**

*Autor:*  Bc. Sára Haidlová

*Studijní program:*  Jaderná a částicová fyzika
*Druh práce:*  Diplomová práce

*Vedoucí práce:*  Mgr. Michal Broz, Ph.D.
Katedra fyziky, Fakulta jaderná a fyzikálně inženýrská,
ČVUT v Praze

*Abstrakt:*  Zkoumání struktury hadronů a jejich vlastností je rozsáhlé odvětví částicové fyziky a fyziky těžkých iontů. Studium exkluzivní fotoprodukce $J/\psi$ poskytuje nástroje pro zkoumání jevů spojených s vlastnostmi partonových distribučních funkcí. Zde popsaná analýza poskytuje novou perspektivu na studium srážek těžkých iontů za použití postupu, který nepoužívá proměnné závislé na modelu a soustředí se výhradně na přímo měřitelné pozorovatelné. Tento postup zvaný kvantová tomografie byl aplikován na data měřená v roce 2018 při srážkách Pb-Pb při $\sqrt{s_{NN}} = 5.02$ TeV. Analýza využívající tomografii kvantových stavů umožňuje určení kvantových stavů z úhlového rozdělení v konečném stavu a určení polarizace. Mezi další aplikace patří studium entropie nebo kvantového provázání.

*Klíčová slova:*  UPC, $J/\psi$, polarizace, kvantová tomografie

*Title:*
**Quantum tomography of the two-lepton system with ALICE**

*Author:* Bc. Sára Haidlová

*Study program:* Nuclear and Particle Physics
*Sort of project:* Master thesis

*Supervisor:* Mgr. Michal Broz, Ph.D.
Department of Physics, Faculty of Nuclear Sciences and Physical Engineering, Czech Technical University in Prague

*Abstract:* Probing of hadron structure and their properties is a vast field of interest in particle and heavy-ion physics. The study of exclusive photoproduction of $J/\psi$ provides tools for probing phenomena connected to properties of parton distribution functions. The presented analysis provides a new perspective on studies of heavy-ion collisions by introducing a procedure omitting model-dependent variables and focuses solely on available directly measured observables. This procedure, quantum tomography, was applied to measured data from 2018 data taking of Pb-Pb collision at $\sqrt{s_{NN}} = 5.02$ TeV. Analysis utilizing the quantum state tomography shows a possibility of quantum state determination from final state angular distribution together with polarization determination. It could be further applied in studies of entropy or quantum entanglement.

*Key words:* UPC, $J/\psi$, polarization, quantum tomography

# Contents

# List of Tables

# List of Figures

# Introduction

The inner structure of matter and its evolution since the beginning of time is a widely studied topic in particle physics. An insight into this problematics can be achieved by studying the collisions of heavy ions and the creation and behaviour of the Quark Gluon Plasma. Throughout the years, scientists have developed a wide range of detectors and instruments together with analysis tools in order to provide information about the inner structure of hadrons.

A great tool for studies of parton structure are ultra-peripheral collisions (UPCs) of heavy ions. Several experiments and physicists observed phenomena related to the structure of hadrons such as the nuclear shadowing or gluon saturation. A brief overview of the beginnings of studies of hadron structure ending in the presentation of evolution equations is introduced in Chapter 1.

The bulk of the studies and determination of properties of matter are based on phenomenological models. A procedure for the determination of properties of studied particles, quantum state tomography, provides a unique way to study a variety of properties of quantum states using only available measured variables without utilization of complex models.

This thesis introduces a study of Monte Carlo generated data samples of coherently and incoherently produced $J/\psi$ together with the study of measured data sample from 2018 data taking of Pb-Pb collisions at $\sqrt{s_{NN}} = 5.02$ TeV provided by the ALICE Collaboration. Studied measured data are provided by the ALICE experiment. The quantum tomography procedure is applied to data for the determination of polarization of studied states.

# Chapter 1

# Structure of Hadrons

The study of hadron structure has begun with the discovery of an atomic inner structure. The studies of nuclei, their properties, and their structure led to the discovery, that protons are composed of protons and neutrons. This discovery naturally leads to an idea of the inner structure of hadrons within nuclei. This structure is generally probed by deep-inelastic scattering (DIS), even though the first scattering was elastic. This type of scattering results in a hadron dissociation and the creation of new particles. Based on the DIS measurements it was observed that the hadrons have an inner structure and the first theory describing this phenomenon was the parton model designed in the 1960s by Richard Feynman.

## 1.1 Scattering Experiments

The most convenient way of describing the evolution of scattering experiments is by lepton-proton scattering. Some of these experiments took place before the invention of Quantum Chromodynamics (QCD) and are thus described in the framework of Quantum Electrodynamics (QED). For further description, we will consider a process [1]

$$l(k) + p(P) \rightarrow l'(k') + X, \tag{1.1}$$

where $X$ denotes an allowed final state by conservation laws and $l, l'$ are scattered leptons. The lepton and proton may interact by an exchange of intermediate vector bosons $W^{\pm}$ or $Z$ that mediate charged and neutral current processes, respectively. The dynamics of scattering experiments are described by a differential cross-section. The first step in deriving a cross-section is writing out the matrix element of a corresponding process. To begin with the easiest process, we will introduce the cross-section of elastic scattering on a point-like proton, i.e. a proton without an inner structure [1]

$$\frac{d\sigma}{dQ^2} = \frac{2\pi\alpha^2}{Q^4} \left[ 1 + (1-y)^2 - \frac{M^2 y}{kp} \right]. \tag{1.2}$$

The cross-section introduces several variables that are crucial for the description of scattering processes. Among these is $Q^2$ which is the virtuality (in absolute value the same as the transferred momentum) and $y$ is the inelasticity of the scattering measuring if the scattering is elastic or not. $\alpha$ is the coupling constant describing the

strength of an interaction. Variables $k, p$ denote the momenta of lepton and proton and $M$ is the invariant mass.

For comparison with formulas from classical mechanics, e.g. Mott's formula, it is convenient to transform the cross-section into a laboratory frame, which yields [1]

$$\frac{d\sigma}{d\Omega_{lab}} = \frac{\alpha^2 \cos^2 (\theta_{lab}/2) E'}{4E^2 \sin^4 (\theta_{lab}/2) E} \left[ 1 + \frac{Q^2}{2M^2} \tan^2 (\theta_{lab}/2) \right], \tag{1.3}$$

where $\theta_{lab}$ is an angle between the scattered lepton and the direction of travel of the probe. In the limit of infinite mass, this cross-section yields Mott's cross-section that describes the relativistic scattering of an electron on a proton.

Further generalization led to the introduction of form factors. These form factors describe the inner structure of a proton by providing the distribution of electric and magnetic charge. The elastic form factors describing electromagnetic structure are denoted $F_1(Q^2)$, $F_2(Q^2)$. In order to give solely electric and magnetic form factors, it is crucial to introduce $G_E(Q^2)$ and $G_M(Q^2)$. With these in mind, Mott's cross-section can be corrected as [2]

$$\frac{d\sigma}{d\Omega_{lab}} = \sigma_{Mott} \frac{E'}{E} \left[ \frac{G_E^2(Q^2) + \tau G_M^2(Q^2)}{1 + \tau} + 2\tau G_M^2(Q^2) \tan^2 (\theta_{lab}/2) \right], \tag{1.4}$$

where $\tau = Q^2/4M^2$.

The elastic scattering of electrons on nuclei and protons was vastly studied in the 1950s at Stanford University [3]. The group of experimentalists was led by Robert Hofstadter and achieved several discoveries amongst which was the proof of a finite size of nuclei without a sharp edge [1]. With further advancements, they achieved a measurement of the scattering of electron on a proton showing that a proton has an inner structure and measured its radius. Unfortunately, at that time the experiment did not provide high enough energies for inelastic scattering. An upgrade to a new accelerator and accompanying foundation of Stanford Linear Accelerator Center (SLAC) allowed for a rise in energies of probing electrons and further studies. That was later achieved by a group from Stanford and MIT that was even able to measure inelastic scattering, even though it was not originally planned, showing the need for the parton model.

The inelastic scattering, or deep-inelastic scattering, the final state has to be described by two independent variables for the description of the final state yielding a double differential of the cross-section. The cross-section corresponding to inelastic scattering is [1]

$$\frac{d\sigma}{dQ^2} = \frac{4\pi\alpha^2}{Q^4} \left[ \left( 1 - y - \frac{M^2 xy}{s} \right) \frac{F_2(x, Q^2)}{x} + \frac{1}{2}y^2 2F_1(x, Q^2) \right]. \tag{1.5}$$

The functions $F_i(x, Q^2)$ are again electromagnetic form factors or, more often, structure functions. The inelastic form factors and their behaviour are further described in the parton model.
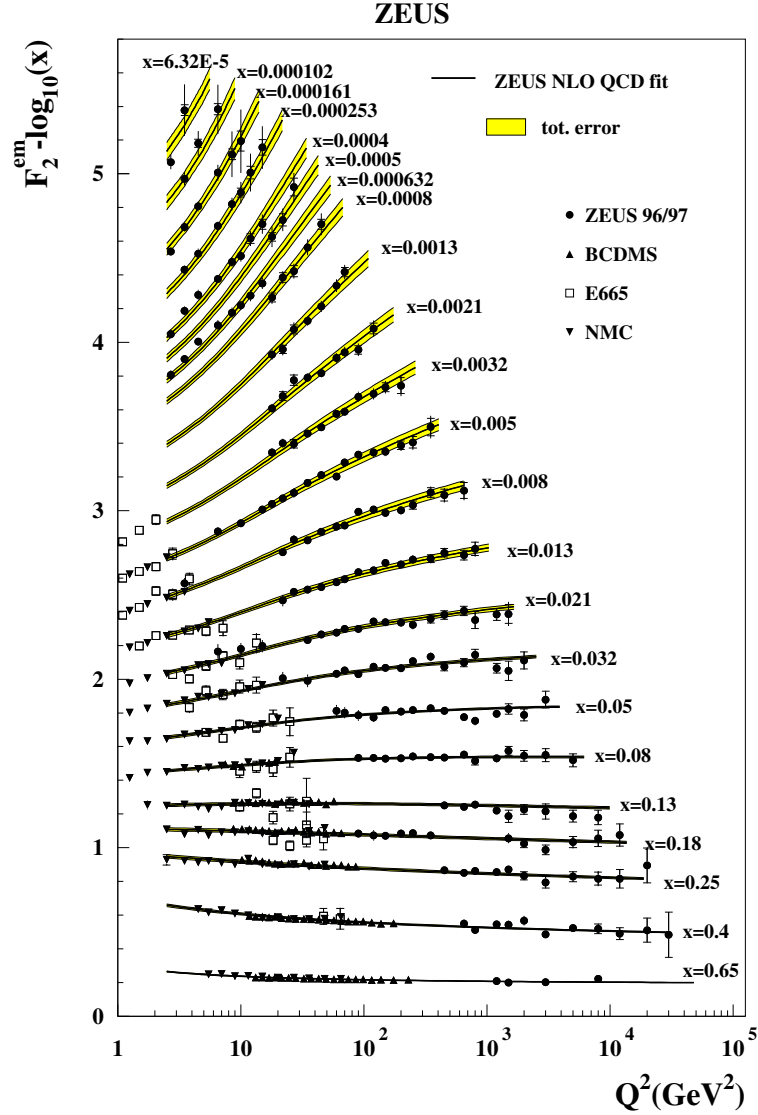
**Figure 1.1:** Dependence of the structure function $F_2(x, Q^2)$ on transferred momentum $Q^2$ for different Bjorken-$x$ values [4].

## 1.2 The Parton Model

The measurements of inelastic scattering and the inelastic structure functions were measured by the ZEUS collaboration and their results are shown in Figure 1.1. The figure shows measurements for various Bjorken-$x$ values from different experiments and their dependence on transferred momentum $Q^2$. These measurements showed a striking feature of the structure functions the so-called Bjorken scaling. For large values of Bjorken-$x$, the structure functions show no dependence on $Q^2$.

The behaviour of measured structure functions led Feynman to the idea of the parton model. He stated that in DIS the electron does not interact coherently with the whole proton, but with its constituents, partons. The structure functions are then defined by parton distribution functions as $F_2(x) = x \sum_i e_i^2 f_i(x)$ [1], both only dependent on Bjorken-$x$ due to the aforementioned scaling.

This model led to a further, deeper, look into the structure of hadrons. The measurements leading to the determination of the existence and distribution of partons showed results differing from expectations by a factor of 2. This led closer to the formulation of Quantum Chromodynamics (QCD) by identifying new neutral partons called gluons to explain this difference.

With the idea of gluons in mind, the measured distribution functions describe not only quarks but also these neutral gluons. The result of such measurement is seen in Figure 1.2. This figure shows the distribution functions of a probed proton. The quark distribution functions at large Bjorken-$x$ show expected dependence with the number of constituent $u$ quarks being approximately double the size of $d$ quarks. This was expected from the mathematically described structure, the additive quark model. However with decreasing Bjorken-$x$ their PDFs decrease and there is a steep rise in PDFs of gluons and sea quarks.
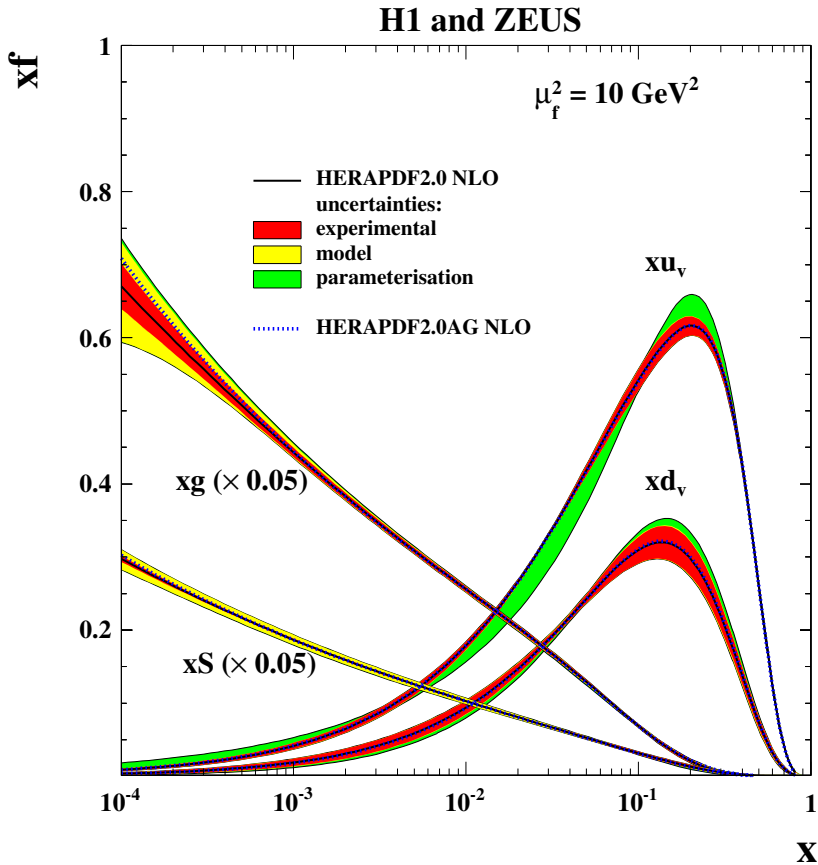


**Figure 1.2:** The parton distribution functions $xu_v$, $xd_v$, $xS = 2x(\bar{U} + \bar{D})$ and $xg$ of HERAPDF2.0 NLO at $\mu_f^2 = 10\,\mathrm{GeV}^2$. The gluon and sea distributions are scaled down by a factor of 20. The experimental, model and parameterization uncertainties are shown [5].

The rise in gluon and sea quark distributions can be only seen in the case of highly energetic probes. This steep dependence can be explained by assuming that the highly energetic probe exchanges virtual quarks that fluctuate into a $q\bar{q}$ pair or radiate a gluon. However, this process has to stop at some point due to the limited density inside the proton. It means the gluon recombination would play a key role and balance the PDFs. This process is called gluon saturation.

Another striking feature of the distribution functions can be examined by defining the ratio $R^A(x, Q^2)$ [6] as

$$R^A(x, Q^2) = \frac{F_2^A(x, Q^2)}{A F_2^{nucleon}(x, Q^2)}, \qquad (1.6)$$

where $A$ is the atomic mass of the nucleus and $F_2$ are the corresponding structure functions. In an ideal case, this ratio is expected to be 1 as the structure function of the nucleus should be only a multiplication of the structure functions of its constituents.

The measurements of these ratios showed that for the region of small Bjorken-$x$, the ratio is smaller than one. This phenomenon is referred to as nuclear shadowing. The experimental data show several characteristics of nuclear shadowing such as the increase of this effect with decreasing Bjorken-$x$ or atomic mass number and decrease with increasing $Q^2$. These features can be seen in comparison with dipole models shown in Figure 1.3. On the right-hand side, there is a measurement with lighter calcium nuclei showing a smaller decrease than in the case of heavier lead nuclei. Furthermore, both nuclei reach the expected value of 1 for larger Bjorken-$x$ and show stronger shadowing effects for lower $Q^2$ measurement provided by the EMC collaboration. The origin of these effects comes from the simple assumption, that the hadronic component of interacting virtual photon will undergo multiple scattering with several constituents of the nuclei resulting in a decrease in observed cross-section.
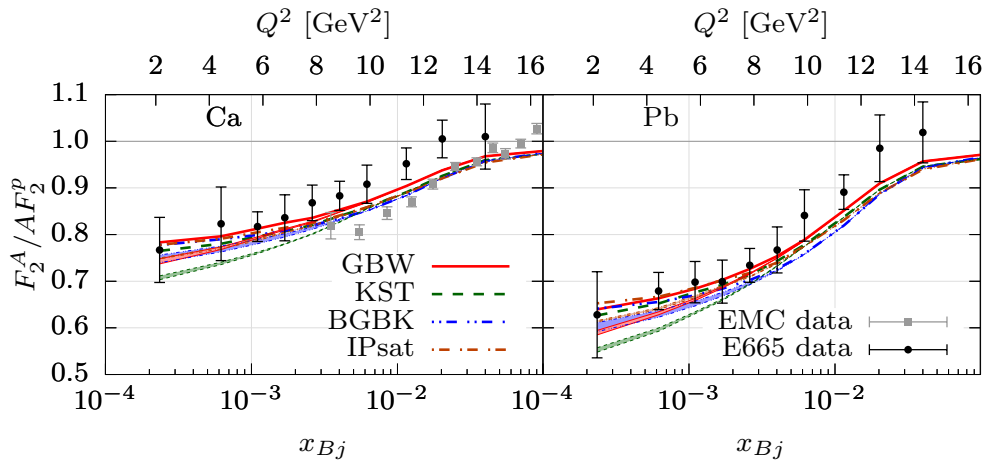


**Figure 1.3:** Comparison of measured data to model predictions of nuclear shadowing for Ca and Pb targets. The predictions are calculated for dipole models listed in figure [7].

## 1.3 Improved Quark-Parton Model

With further evolution of physics and quantum field theories, the original parton model was improved by the framework of perturbative QCD. This improvement contained the basic ideas of the original quark-parton model with a division of the space-time evolution of the process into three stages. The first stage is the initial evolution described by distribution functions that depend on the Bjorken-$x$ and factorization scheme. This scheme is crucial for these functions as they are

given by interactions acting at large distances and thus cannot be described by perturbative QCD. The second part is a hard scattering describing an interaction on short distances and described by a cross-section on the parton level [1]. The last part is hadronization, again not describable by the perturbative QCD and is usually based on hadronization models. The general scheme is shown in Figure 1.4.
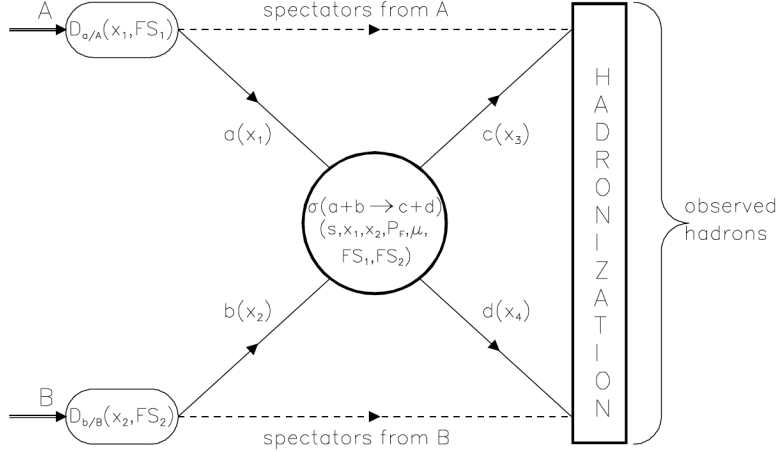


**Figure 1.4:** The general scheme of QCD improved parton model [1].

With an inner structure of partons in mind and the power of quantum field theories, one may proceed with descriptions of interactions of partons within partons and partons within hadrons.

Partons within partons framework can be based on the Equivalent photon approximation derived by Weizsäcker and Williams and further described in 4, yielding branching functions for quarks and gluons. This framework treats quarks and gluons as free particles both before and after a collision.

To describe partons within hadrons, it is necessary to assume that quarks and gluons exist inside hadrons and they behave freely at short distances. This is taken into account by evolution equations. These equations are derived from the concept of primordial quark. The primordial (or bare) quark has a corresponding distribution function which is solely a function of Bjorken-$x$ and can be described by a simple parton model. The next step is a derivation of renormalized (or dressed) quark distribution that considers multiple gluon emission of the primordial quark and is denoted $q_N S(x, M)$ and is given by a sum of contributions from gluon emission. This introduces an upper limit for the dressed distribution given by $M^2$. Derivating the dressed distribution by a logarithm of $M$ (similarly to QED), one obtains

$$\begin{aligned}
\frac{dq_{NS}(x, M)}{d\ln M^2} &= \frac{\alpha_s(M)}{2\pi} \int_x^1 \frac{dy}{y} P_{qq}^{(0)}\left(\frac{x}{y}\right) q_{NS}(y, M) \\
&= \frac{\alpha_s}{2\pi} \int dz \int dy P_{qq}^{(0)}(z) q_{NS}(y) \delta(x - yz) \\
&= \frac{\alpha_s}{2\pi} P_{qq}^{(0)} \otimes q_{NS},
\end{aligned} \tag{1.7}$$

where $P_q q^{(0)}$ is the QCD branching function. This formula is the famous Dokshitzer-Gribov-Lipatov-Altarelli-Parisi (DGLAP) equation [1]. The dependence of DGLAP

and other important evolution equations on virtuality and Bjorken-$x$ is shown in Figure 1.5. The figure shows that for larger $Q^2$ the size of partons is decreasing whereas their number rises. In comparison, the BFKL evolution equation, which applies for decreasing Bjorken-$x$ leads to increased an number of partons without a change in size thus leading to their overlap in the saturation region.
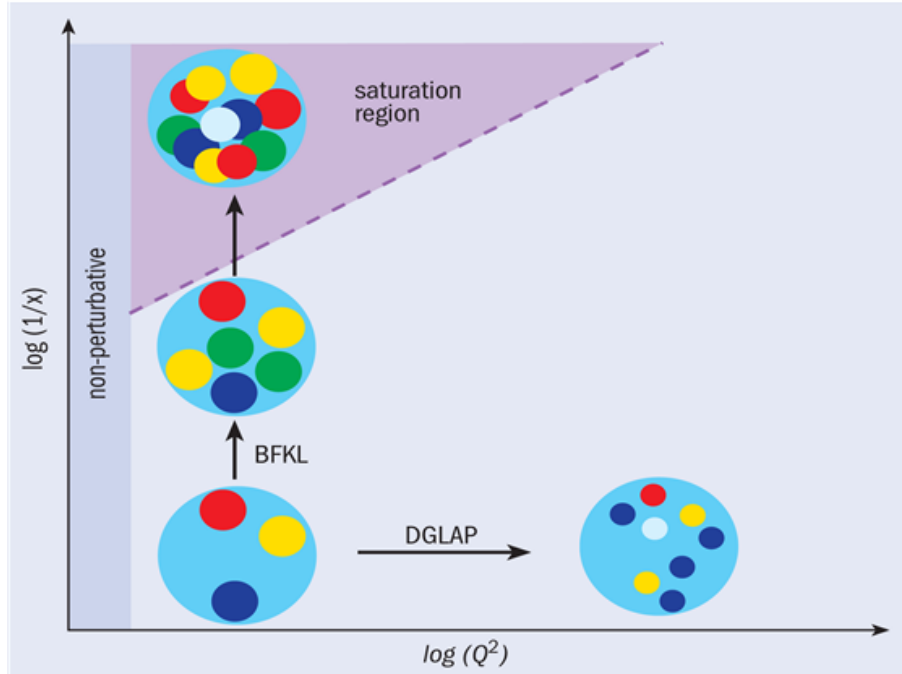


**Figure 1.5:** Illustration of evolution equations in QCD and their influence on the inner structure of nuclei with given $Q^2$ or Bjorken-$x$ [8].

# Chapter 2

# Quarkonium Polarization

The quarkonium of interest for the purposes of this thesis is the J/$\psi$ vector meson, a bound state of charm $q\bar{q}$ pair. This particle is considered a vector meson with quantum numbers $J^{PC} = 1^{--}$ with $J$ being the angular momentum, $P$ parity and $C$ the charge conjugation. The value of angular momentum hints that the state of the vector meson is a superposition of three possible projections of its eigenstates in a given direction. This direction for our purposes will be denoted by the polarization axis $z$. With the eigenstates being $J_z = +1, -1, 0$ we can write the vector meson state as

$$|\text{J}/\psi\rangle = b_{+1}|+1\rangle + b_{-1}|-1\rangle + b_0|0\rangle. \tag{2.1}$$

Both the angular momentum and its projections comply with the conservation laws and together with symmetries of strong and electromagnetic interactions. It may be observed, that a vector meson is observed in a preferred projection of the angular momentum given a characteristic axis. If this phenomenon is observed, the particle is said to be polarized.

The polarization can be investigated through the angular distribution of lepton pairs that are created through the decay of the vector meson. These processes have a unique topology as they are moving back-to-back. One of the impacts affecting the polarization in the final state is the production mechanism of J/$\psi$.

## 2.1 Production and Polarization

When describing a fermion (a particle with non-integer spin, e.g. lepton) that is relativistic (moving at speeds close to the speed of light), one uses, in the Quantum Field Theory, two-component spinors. Were we looking at the fermion in classical physics with its speed being significantly smaller, these spinors could be understood as two possible spin states referred to as spin-up and spin-down. For relativistic particles, this former notation is not useful and it is needed to derive a new notation, helicity. Helicity is defined as a projection of the particle spin onto the momentum direction. If the spin is aligned with the momentum, the helicity is in $h^+$ state and in $h^-$ the other way around. One of the disadvantages of the helicity is its change under Lorentz transformation. Lorentz invariant quantity to describe the 2 possible states is the chirality that is either lefthanded or righthanded for spin aligned with

momentum or not, respectively. These quantities coincide in case the fermions are considered massless. In the massless case, the direction of momenta is not reversible by Lorentz transformation thus the chiral components become eigenstates of helicity. A great advantage of these quantities is in invariance under parity transformation.

Figure 2.1 displays Feynman diagrams at the tree level of three types of processes resulting in observable polarization states.
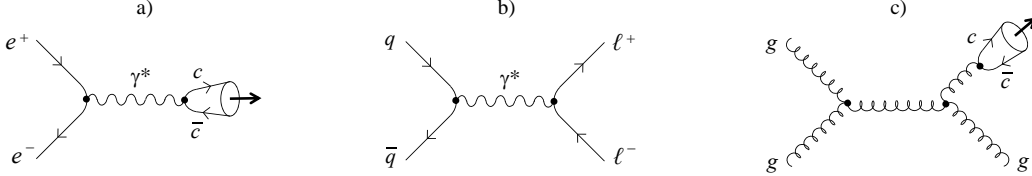


**Figure 2.1:** Several leading-order diagrams for production mechanisms giving rise to observable polarizations:(a) Charmonium production in electron-positron annihilation; (b) Drell-Yan $q\bar{q}$ annihilation; (c) charmonium production by gluon fragmentation to colour-octet [9].

The first diagram (a) shows a process where an electron and a positron annihilate into a virtual photon that further fluctuates into a charm $q\bar{q}$ pair. This process is governed by the QED which, considering the fermion pair mass to be zero, conserves helicity. This leads to a conclusion that the resulting state will be polarized. Helicity plays a crucial role in determination of polarization in the final state. The virtual photon has a helicity equal to zero. If the process is observed in the laboratory frame, the incoming fermions have opposite momenta, by definition, thus having parallel spins in order to obtain opposite helicities resulting in a zero helicity virtual photon. As the angular momentum is conserved the resulting charmonium will inherit the angular momentum alignment thus being in a pure $J_z = \pm 1$ state aligned with the direction of colliding fermions.

The second diagram (b) shows the so-called Drell-Yan production process. In this case, the incoming fermions are not leptons but a quark and an antiquark annihilating into a virtual photon (or a Z boson) further creating a dilepton pair. This process is often observed in a scattering of two hadrons with high energies. Similarly to the previous case, the annihilating quarks must have opposite helicities, again in the zero mass limit, and the dilepton pair in the final state will have $J_z = \pm 1$ along their relative velocities. Considering a QCD process, where quarks annihilate into a virtual gluon, the resulting polarization will be similar, as in aligned with the beam direction, based on the same assumption that the helicity is conserved in QCD.

The last diagram (c) shows a process particularly important at high transverse momentum called gluon fragmentation. This fragmentation is described by a fragmentation fraction given by a fraction of the longitudinal momentum carried by the quarkonium and by a factorization scale. The resulting J/$psi$ is produced in a colour-octet state, based on assumptions from NRQCD (non-relativistic QCD). It considers the fragmenting gluon to be on-shell, thus having nonzero helicity, that is further inherited by created vector meson. This leads to observation of charmonium with projections $J_z = \pm 1$ along its own flight direction.

It is also possible for the charmonium to be unpolarized, i.e. the angular momentum has no preferred direction. This means the charmonium can be found in any of the

eigenstates $J_z = \langle -J, +J \rangle$ with the same probability. This situation can be described by the colour evaporation model.

In order to study the polarization of charmonium created in any possible process, one can study the kinematics of its decay products. In the case of J/$\psi$, the dilepton pair. The polarization affects the shape of the angular distribution of these products giving the observer the ability to determine the preferred alignment.

## 2.2 Coordinate System and Reference Frames

In order to study the angular dependence of the decay products, one has to define a coordinate system for the measurement. Considering the $z$ axis of the system to be a polarization axis, the $x$-axis is chosen in a plane containing the colliding beams and the $y$ axis in the plane perpendicular to the beam. The definition of the polarization axis depends on the chosen reference frame. We will introduce three generally chosen reference frames.

To describe how to obtain these special frames, we will mention terms such as the laboratory (LAB) and the centre-of-mass (CMS) system. The laboratory frame is the reference frame where the experiment is at rest. The centre-of-mass frame is a frame where the momentum of the whole system is zero while keeping the axis orientation of the laboratory frame.

### 2.2.1 Collins-Soper Frame

The Collins-Soper (CS) frame was first presented in 1977 by Collins and Soper in their studies of Drell-Yan production processes. This frame was defined in order to be able to describe the cross-section with angular dependence approximated by the tree-level approximation and not be sensitive to hard QCD radiation. This frame is defined on an event-by-event basis as it describes the rest frame of the final dilepton pair. The schematic of the Collins-Soper frame is shown in Figure 2.2.
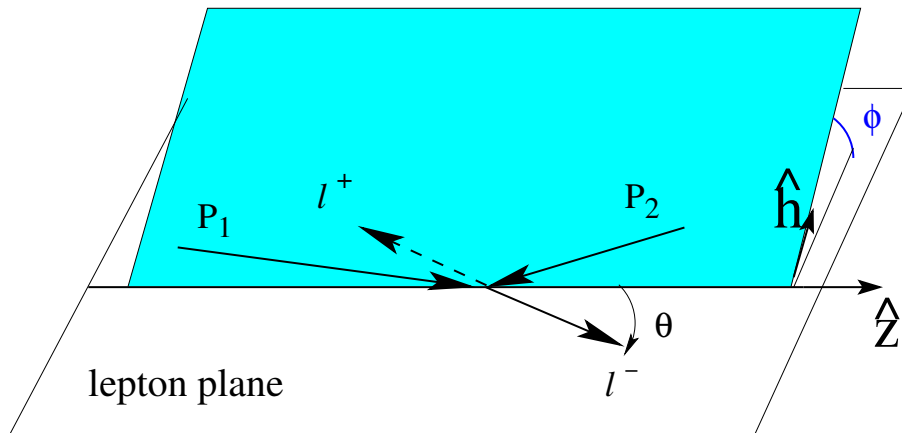


**Figure 2.2:** The schematic for visualization of the Collins-Soper frame [10].

The figure shows the lepton plane in white with the polar angle $\theta$ being defined inside said plane and the azimuthal angle $\phi$ to be between the lepton and the hadron plane

(shown in blue), which is defined by $P_1$ and $P_2$ denoting the colliding beams. The $z$ axis in this case is defined in the place where the hadron and lepton plane meet.

This frame can be obtained from the LAB frame either by boosting the LAB frame to the CMS and further rotating it around the polarization axis to form the same azimuthal and polar angles as the initial state particles. Another way is using two boosts to the vector meson rest frame and then to the CMS frame. These transformations are represented by Lorentz transformation matrices $\Lambda(LAB \to CS) = \Lambda_\perp(y_\perp)\Lambda_\parallel(y_\parallel)$ [11]. They results in simplification of four-momenta of both dilepton pair and a vector meson such as $p_y^V = p_y^{l-} + p_y^{l+} = 0$ and $p_x^V = p_x^{l-} + p_x^{l+} = p_T$ showing that one needs only transverse momenta components in order to derive both $\sin\theta_{CS}$ and $\cos\theta_{CS}$.

## 2.2.2 Helicity Frame and Gottfried-Jackson Frame

The helicity and Gottfried-Jackson (GJ) frames are introduced together due to their similarities. Both reference frames are measured in the rest frame of the vector meson. Their $y$-axis is the same (perpendicular to the production plane) and the reaction plane contains the momenta of the colliding nuclei. These two frames differ in the definition of their $z$ (polarization) axis. The GJ frame takes the direction of colliding particle as the $z$-axis whereas helicity takes the opposite of the boost direction. This boost is used in order to obtain a helicity frame from the CMS. The illustration of these different polarization axes is shown in Figure 2.3 which is shown also as a comparison of the aforementioned CS frame.
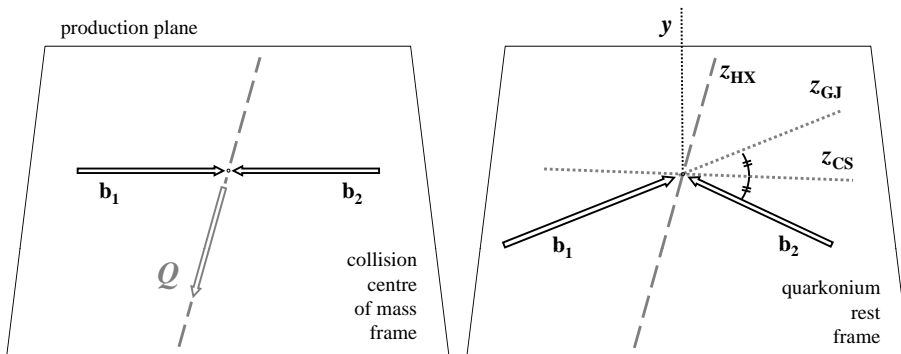


**Figure 2.3:** Illustration for comparison of CS, GJ and helicity polarization axis with respect to colliding beams and quarkonium ($Q$) [9].

From the comparison of the three reference frames, one can see that in all cases the polarization axis lies within the production plane. In order to switch between reference frames a simple geometrical rotation can be applied around the common $y$-axis using the rotation matrix $R_y(\delta)$, where $\delta$ is the rotation angle between frames

$$R_y(\delta) = \begin{pmatrix} \cos\delta & 0 & -\sin\delta \\ 0 & 1 & 0 \\ \sin\delta & 0 & \cos\delta \end{pmatrix}. \tag{2.2}$$

This rotation matrix is applied on the unit vector describing the position of the lepton $\hat{r} = (\sin\vartheta\cos\varphi, \sin\vartheta\sin\varphi, \cos\vartheta)$. The rotation angle depends on the kinematics

of the system, which can be shown in an example for rotation from helicity to CS frame, where the beam is oriented as a $z$-axis in the LAB system. Then the rotation angle is defined as

$$\delta = \arccos\left(\frac{mp_L}{m_T p}\right). \tag{2.3}$$

## 2.3 Study of Quarkonia Polarization

Studied vector meson decays to a dilepton pair through electromagnetic interaction. By measuring the distribution of decay products, the experimentalist is able to determine the "spin alignment" of said particle. The kinematics of such a decay is shown in Figure 2.4. The schematic shows a J/*psi* in its rest frame decaying into
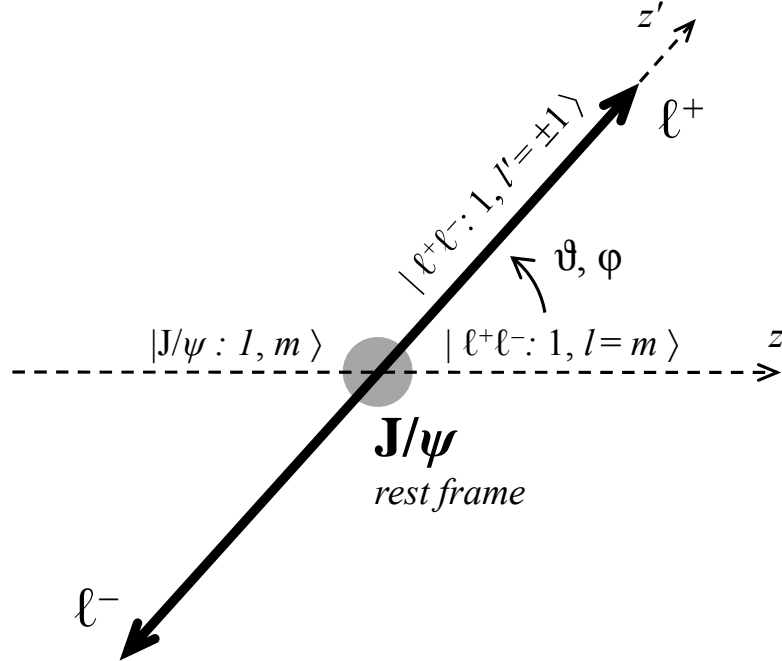


**Figure 2.4:** Schematic of a J/$\psi$ decay into two leptons showing axes, angles and angular momentum states [9].

two leptons emitted back-to-back along a new axis $z'$ that is obtained by rotating by angles $\theta$ and $\phi$. As mentioned at the beginning of this section, charmonium has an angular momentum 1 with three possible projections. The key to obtaining a preferred alignment through decay products is expressing the eigenstate of $J_{z'}$ by a superposition of $J_z$ eigenstates. This can be done by applying rotation transformation to a final state eigenstate as

$$|\ell^+\ell^-;1,l'\rangle = \sum_{l=0,\pm 1} \mathcal{D}^1_{ll'}(\varphi,\vartheta,-\varphi)\,|\ell^+\ell^-;1,l\rangle\,, \tag{2.4}$$

where the primed notation is taken from the schematic together with the rotation angles in the complex rotation matrix element $\mathcal{D}^1_{ll'}(\varphi,\vartheta,-\varphi)$. By calculating the amplitude of such process and summing over all observable production processes

one arrives at the angular distribution

$$
\begin{aligned}
W(\cos\vartheta, \varphi) \quad &= \quad \sum_{i=1}^{n} f^{(i)} W^{(i)}(\cos\vartheta, \varphi) \\
&\propto \quad \frac{1}{(3+\lambda_\vartheta)} \left( 1 + \lambda_\vartheta \cos^2\vartheta \right. \\
&+ \quad \left. \lambda_\varphi \sin^2\vartheta \cos 2\varphi + \lambda_{\vartheta\varphi} \sin 2\vartheta \cos\varphi \right),
\end{aligned}
\tag{2.5}
$$

where $W^{(i)}$ corresponds to a distribution in each elementary process. This formula introduces three parameters $\lambda_\vartheta, \lambda_\varphi, \lambda_{\vartheta\varphi}$. By obtaining these parameters one is able to determine the observed polarization state of quarkonium. The values of these parameters are coupled and they are allowed to exist only within certain intervals. Allowed regions for these parameters are shown in Fig. 2.5. Furthermore, independently of the reference frame, it is possible to deduce $|\lambda_\varphi| \leq \frac{1}{2}(1+\lambda_\vartheta)$ and $|\lambda_{\vartheta\varphi}| \leq \frac{1}{2}(1-\lambda_\varphi)$.
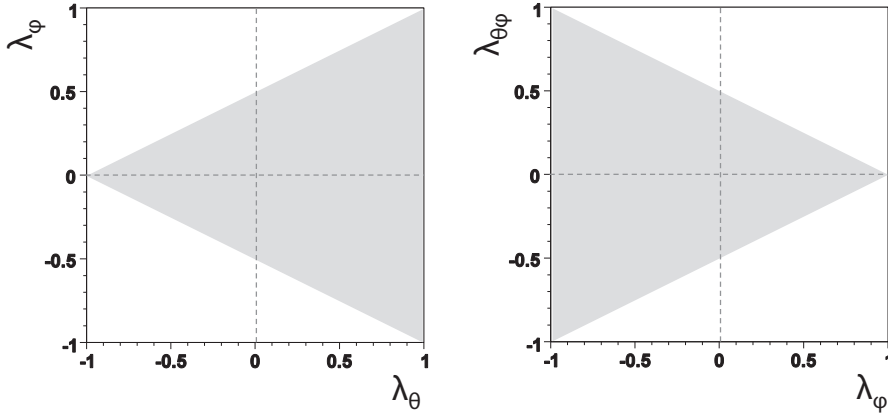


**Figure 2.5:** Allowed regions for $\lambda_\vartheta, \lambda_\varphi, \lambda_{\vartheta\varphi}$ describing the angular parameters [9].

However, these quantities and the distribution itself are strongly dependent on the reference frame and on the kinematics of the measured particle. The problem of dependence on the observation frame is shown in Fig. 2.6. The figure shows the decay distribution of fully longitudinally (b,d) and transversely (a,c) polarized vector meson. From seeing these distributions one can deduce, that they are parity independent due to their angular symmetry. The distributions in figures (a,b) show distribution in the natural polarization frame whereas the figures (c,d) show distribution rotated 90 degrees. The polarization is rarely fully longitudinal or fully transversal. In order to obtain one of these results, it is necessary to observe an angular distribution (2.6) with only $\lambda_\vartheta$ or $\lambda_\varphi$. In order to obtain an unpolarized state, the parameters of (2.6) would all have to vanish and the distribution would thus have no angular dependence.

The dependence of decay parameters on the reference frame can be further described by considering CS and helicity frames, which are (as seen in Fig. 2.3) perpendicular to each other. Considering the natural polarization to be transversal (i.e. $\lambda_\vartheta = 1, \lambda_\varphi = \lambda_{\vartheta\varphi} = 0$, after rotating it one obtains $\lambda'_\vartheta = -1/3, \lambda'_\varphi = 1/3$ thus showing angular anisotropy. By rotating we obtain a state that is half transversely polarized and half longitudinally polarized. Seeing this strong reference frame dependence,
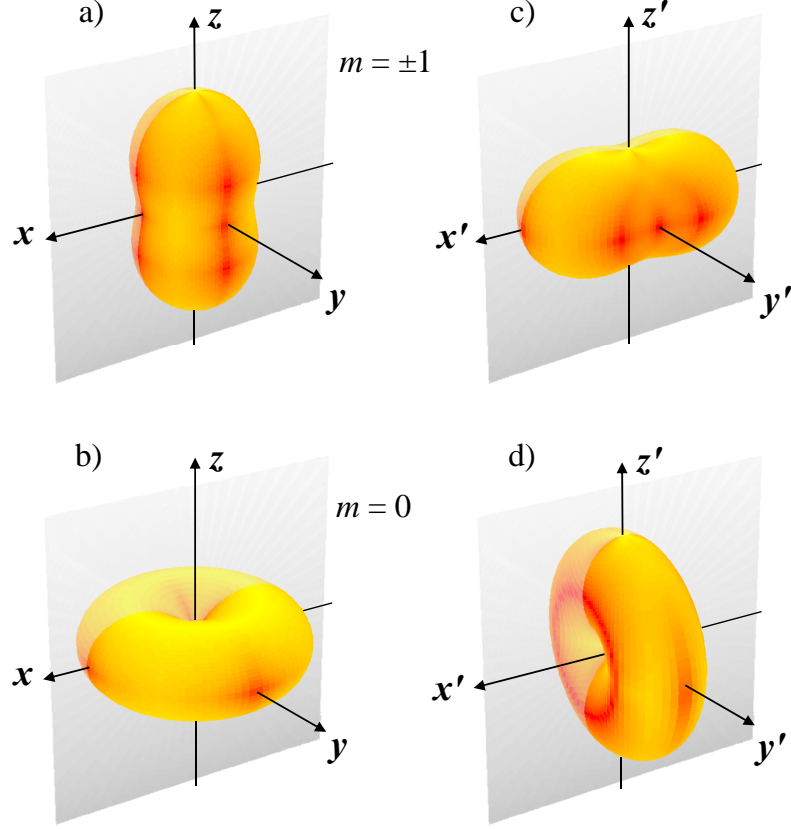
**Figure 2.6:** Representation of dilepton decay distribution of polarized quarkonium using the probability of emitted lepton and representing it by the distance of a surface point from the origin of the coordinate system. Figure a) shows transversely polarized and b) longitudinally polarized examples in the natural frame and c) and d) corresponding polarizations in a rotated frame by 90 degrees [9].

there is obviously a need to define a frame invariant variable $\tilde{\lambda}$ defined as

$$\tilde{\lambda} = \frac{\lambda_\vartheta + 3\lambda_\varphi}{1 - \lambda_\varphi} \,. \tag{2.6}$$

with values values $(-1, +1)$ corresponding to longitudinal and transversal polarizations respectively.

# Chapter 3

# Quantum Tomography in Particle Physics

In general, quantum tomography can be used to describe all observable features of a given quantum mechanical system while bypassing formalisms based on quantum field theory such as the scattering amplitudes or structure functions. The knowledge of the characteristics of a quantum state is crucial for the verification of experimental outcomes. By avoiding challenging theoretical formalisms, one can focus on experimental data and their characterization. Before we dive into a review of quantum tomography in particle physics, we shall introduce several basic concepts used in quantum mechanics.

## 3.1   Basic Concepts

In further text, we will talk about terms used in quantum mechanics such as quantum state or a density matrix. This section will give the reader a short introduction to this notation.

In order to describe a certain quantum state of a system, one needs to talk about a state representation. In general, we distinguish two types of states, pure and mixed. The pure state can be represented by a so-called ket $|\psi\rangle$ which is a vector in a complex vector space denoted a Hilbert space $\mathcal{H}$. This ket has furthermore unit length, i.e. $\langle\psi|\psi\rangle = 1$. Considering a two-dimensional Hilbert space, a pure state can be represented by $|\psi\rangle = \alpha|0\rangle + \beta|1\rangle$ where $\alpha, \beta$ are complex numbers with $|\alpha|^2 + |\beta|^2 = 1$ [12]. Note that this representation in quantum information is referred to as a qubit (in analogy with a classical bit). For Hilbert space with dimension three, it is a qutrit, for dimension four a ququart and generally for dimensions larger than two a qudit. A general representation of a ket can be in analogy to a two-dimensional space written as

$$|\psi\rangle = \sum_j c_j |\psi_j\rangle, \qquad (3.1)$$

with $\psi_j$ being the basis vectors.

One might also introduce dual vectors to kets called bra $\langle\phi|$ mapping from Hilbert space to a complex space $\mathbb{C}$. The definition of dual vectors allows us to define op-

erators and projectors in quantum mechanics. A projector defined as $\hat{P}_\psi = |\psi\rangle\langle\psi|$ [12] is a type of operator that maps from and to a Hilbert space. It can be used to describe probabilities or expectation values from a measurement of a given state.

So far we have introduced only a pure state and how to denote it. By introducing the operators and projectors, we can also introduce a special density operator or a density matrix. The density matrix describes not only pure but also mixed states (an incoherent mixture of pure states) by denoting a $|\phi_k\rangle$ a set of pure states, the density matrix is defined as [12]

$$\rho = \sum_{k=1}^{N} p_k |\psi_k\rangle\langle\psi_k|, \qquad 0 < p_k \leq 1, \qquad \sum_{k=1}^{N} p_k = 1, \qquad (3.2)$$

together with conditions for coefficients $p_k$. For pure states, kets $|\psi_k\rangle$ describe the basis vectors of Hilbert space and $p_k = 1$. The incoherent mixture can be obtained by interactions between pure states, quantum noise or decoherence. Decoherence is a process when nondiagonal elements, quantum coherences, of the density matrix are reduced. This leads to a possible loss of quantum effects, such as quantum interference, resulting in a loss of information about said state. The definition of density matrix allows to introduce expectation values of measured operators $\hat{A}$. The expectation values are given as $\langle A \rangle = \text{Tr}(A\rho)$ [12].

The density matrix can be further used for the construction of Lorentz invariants such as the degree of polarization or the entanglement entropy. The degree of polarization $d$ is defined as [13]

$$d = \sqrt{(3\text{Tr}(\rho^2) - 1)/2}. \qquad (3.3)$$

The degree of polarization has values between 0 and 1 with $d = 0$ denoting the unpolarized system and $d = 1$ a pure state. This comes from the properties of density matrices when a trace of $\rho^2$ is equal to 1 for pure states and smaller than 1 for mixed states. The more the state is mixed, the more it is unpolarized.

The entanglement entropy $\mathcal{S}$ can be interpreted as a measure of the order of the quantum mechanical system. Using the density matrix it is defined as [13]

$$\mathcal{S}(\rho) = -\text{Tr}(\rho \log \rho), \qquad (3.4)$$

where for the base of the logarithm we can take 2. This yields a unit of entropy called a bit and allows for entropy interpretation as the missing information. Thus for zero entropy, we gain a maximum knowledge that is allowed to gain by quantum mechanics, for larger values we see the amount of missing information. Maximum information is obtained from pure states.

Furthermore, there are some properties of density matrices coming from the definition. One of these properties is the positivity of *rho*. This means that the density operator yields solely positive eigenvalues.

When talking about density matrix, states and polarization, it is convenient to describe states and polarizations using a graphical description, the so-called Poincaré sphere shown in Figure 3.1. This sphere has a unit radius and is shown in a three-dimensional coordinate space of Stokes parameters (further discussed below). Points located on the surface of the sphere are previously mentioned pure states, whereas

mixed states are placed within the sphere. The sphere not only visualizes the pureness of a state but also its polarization. On the equator are places linearly polarized states while coming closer to the poles, the polarization becomes circular. Furthermore, the closer we are to the centre of the sphere, the more unpolarized the states are.
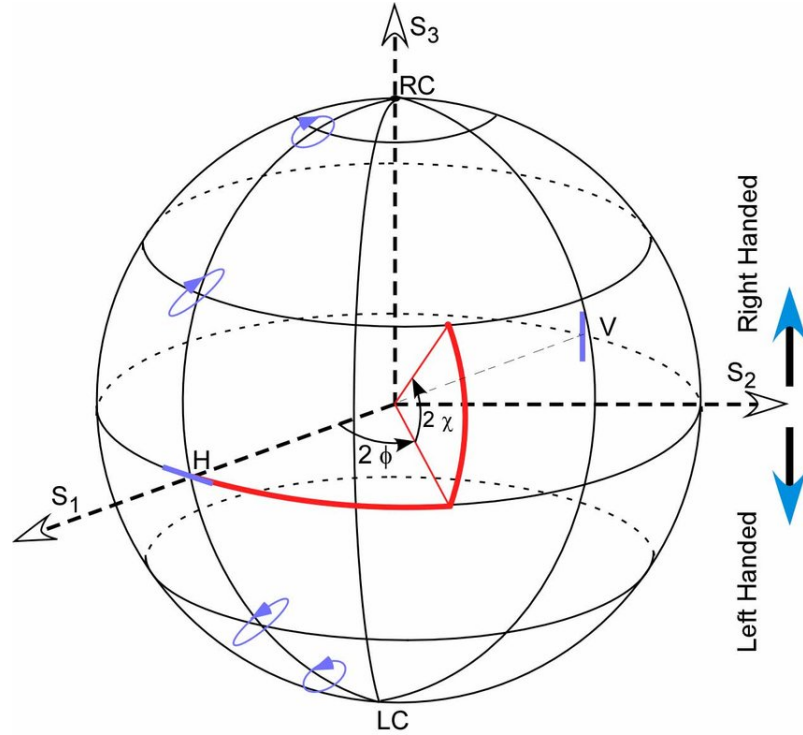


**Figure 3.1:** Graphical visualization of polarized states using the Poincaré sphere. Axes $S_i$ represent Stokes parameters [14].

## 3.2 Evolution of Quantum Tomography

Even though the term quantum tomography seems recent, the possibility of determining a quantum state by experimental measurements has been introduced more than half a century ago by Ugo Fano [15]. Fano in his paper explored the possibility of utilization of a Stokes parameter method in quantum mechanics for a polarization of electromagnetic radiation. In general, the Stokes parameter method is used to describe polarization. They were derived by George Gabriel Stokes [16] to describe polarization in terms of the degree of polarization, total intensity and the shape of the polarization ellipse. Fano introduces Stokes parameters into the theory of density matrices together with possible detector effects and processes leading to interaction with matter from the quantum mechanical point of view. An important observation was, that in order to describe a state by density matrix, one has to provide a complete set of observables, the so-called quorum of observables. However, the identification of these observables seemed to pose a large problem, as only position, momentum and energy came to mind.

The experimental determination of a quantum state has begun in the area of quantum optics [17]. This area of physics studies properties of photons that are assigned

to particles and enables measurements of all possible linear combinations of momentum and position of a harmonic oscillator. The first experiments regarding this topic were performed by Raymer's group [18]. These experiments measured probability distribution for states of a mode of the electromagnetic field while showing a technique called homodyne tomography. This technique was used to yield Wigner distribution and the density matrix of measured mode providing a complete characterization of the quantum mechanical state. A basic schematics of a homodyne experiment is shown in Figure 3.2.
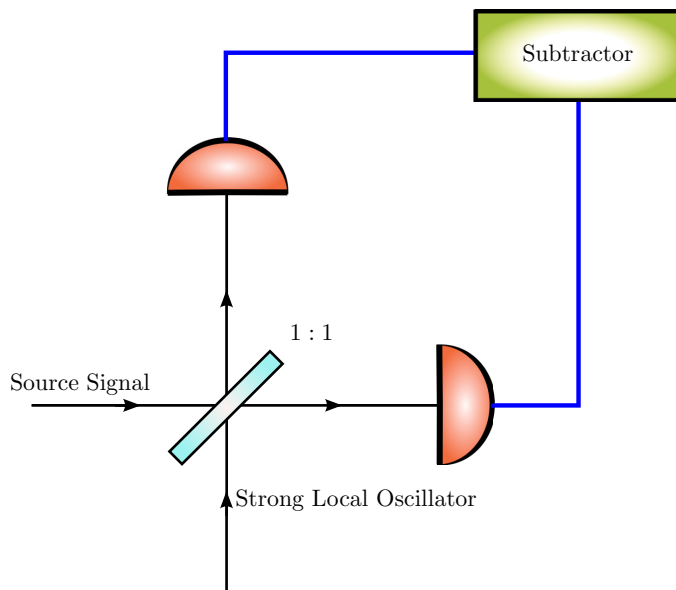


**Figure 3.2:** Schematic of a simple homodyne experiment [19].

The usage of homodyne data proved to be a great idea that further lead to the development of a technique for measuring the matrix elements of the density matrix by averaging the homodyne results. After modifying the technique to be able to use it for detectors with quantum efficiency smaller than one and simplifications in numerical algorithms, the method was suddenly available for implementation on personal computers. This made homodyne tomography accessible to a wide range of laboratories for measurements with semiconductor lasers or of squeezed vacuum states.

Apart from that, the development of a new method of quantum tomography leads to new procedures to reconstruct quantum states of atomic or molecular vibrational states. These techniques allowed us to determine states not only of single trapped ions but also of an ensemble. These further lead to improvements in spectroscopy [20]. Further simplifications and generalizations such as estimations with any number of modes, and measurements of arbitrary quantum systems lead to establishing quantum tomography as an informationally complete measurement, thus yielding a quorum of observables.

The problem of density matrix estimation will be further discussed in the following section, however, for the context of this section, the main method for determining the density matrix was averaging. This method was imperfect due to the fluctuation of the averaging strategy resulting in a violation of positivity of the density matrix. A new method using a maximum likelihood estimation of parameters was

not only constraining the density matrix to be positive but offered the opportunity to reduce the amount of experimental data yielding the same statistical errors as in the previous case.

The estimation of a quantum state (quantum state tomography) allowed studies of its time evolution, a quantum process (quantum process tomography). The determination of a quantum process using a previously defined quantum state is a type of indirect characterization of quantum dynamics. Examples of these tomographies are Standard Quantum Process Tomography (SQPT) [21, 22, 23] and Ancilla-Assisted Process Tomography (AAPT) [24, 25, 26]. The process tomographies are widely used in quantum computing or black box experiments in NMR.

## 3.3   Parameter Estimation

The problem of parameter estimation is a wide topic in the theory of statistical data analysis. Before mentioning some of the methods for parameter estimation, we shall introduce several general concepts and notations.

Similarly to our measurement, let us consider an experiment with $n$ measurements of a variable $x$ with an unknown probability distribution function (p.d.f.). In order to infer the properties of said p.d.f., one constructs a hypothesis based on unknown parameters $\theta$ for the shape of p.d.f. $f(x; \theta)$. The goal is to construct a so-called estimator (in general statistic) $\hat{\theta}$ which is a function defined based on measurements $x_1, \ldots, x_n$ for parameter estimation. Parameter estimating for a given data sample $x_1, \ldots, x_n$ is called parameter fitting.

In order to provide a proper value of estimator, estimate, there are several desirable properties of an estimator. The first to be mentioned is consistency. The consistency of an estimator is given by its convergence to an estimation $\theta$ that is for given $\varepsilon > 0$ as

$$\lim_{n \to \infty} P(|\hat{\theta} - \theta| > \varepsilon) = 0. \tag{3.5}$$

The second crucial property is unbiasedness. The bias of an estimator $b$ is the difference between its expectation value and the estimation. It depends on the size of the sample rather than on the measured values. The estimator can be either unbiased independently of the size of a sample or asymptotically unbiased for the infinity limit. The unbiased estimators are crucial in case one wants to compare the results of several experiments.

The size of a measured sample is further connected with another property, efficiency. The efficiency of an estimator is given by a possible variance of estimates with an increasing number of measurements. The desired property is, that the estimator should give the same results for any sample size. Furthermore, the estimator is expected to be robust. This means that it should not depend on the distribution.

There are also practical desirable properties of estimators such as simplicity, being uncorrelated with other estimates and normally distributed, and it should not be very time-demanding.

There are several methods for parameter estimation, for example, the method of moments, maximum likelihood or $\chi^2$ method. The maximum likelihood method (MLM) is based on finding a maximum of the so-called likelihood function. Considering a set of measurements $x_1, \ldots, x_n$, as in the previous case, the joint p.d.f. of these measurements is given by a product of individual distribution functions as

$$P(\vec{x}|\theta) = \prod_{i=1}^{N} f(x_i|\theta), \tag{3.6}$$

which is equivalent to the likelihood function $L(\theta)$ for measured data. For the case of density matrix, we denote $f(x_i|\theta) = \text{Tr}(M_i\rho)$ as the trace is a result of measurements. The estimate of a parameter is inferred from the maximum value of the likelihood function given a parameter $\theta$. By definition, there is nothing to avoid possible findings of multiple local maxima. In that case, the highest possible value is taken. Due to the product in the likelihood definition, it is often useful to use a logarithm of likelihood.

The MLM estimation can be connected with the previously mentioned $\chi^2$ method. Consider the measured data to be a set of Gaussian random variables. The p.d.f. of each measurement will be given by Gaussian distribution, each measurement having different unknown mean $\lambda_i$ and known variance $\sigma_i^2$. Writing out the logarithm of the likelihood function in this case yields (dropping spare terms independent of the parameters)

$$\log L(\theta) = -\frac{1}{2} \sum_{i=1}^{N} \frac{(y_i - \lambda(x_i, \theta))^2}{\sigma_i^2}, \tag{3.7}$$

where $y_i$ is a measured value of $x_i$ that is considered to be without error. Maximizing this function is equal to minimizing $\chi^2$ that is in this case considered $\chi^2(\theta) = -2\log L(\theta)$. This case is special for Gaussian p.d.f., the $\chi^2$ method can be applied even for other p.d.f.s as long as they are independent. Both the MLM and $chi^2$ methods can be used (with slight modifications) both on binned and unbinned data.

## 3.4 Quantum Tomography in Collider Physics

The application of quantum tomography in collider physics provides a unique opportunity to deal with observable quantities such as invariant mass distribution, the angular distribution of final state particles or the unknown intermediate state of the system, instead of mode-dependent scattering amplitudes. The idea is based on the parametrization of a studied, in general unknown, system by a density matrix $\rho(X)$, while the probe of such system is given by another density matrix $\rho(probe)$ which is known. It is the probe matrix that defines what will be observed based on its dimensions and symmetries while keeping its simplicity using only measured variables.

### 3.4.1 Probe and Unknown Density Matrices

Before showing the quantum tomography procedure in steps, it is convenient to introduce what one can imagine under the term "probe matrix". The probe of an

unknown system, independent of the process yielding dilepton pair, can be in general parameterized as

$$\rho(lep)^{\beta\beta'}_{\alpha\alpha'} \sim (\slashed{k}_1)_{\alpha\alpha'}(\slashed{k}_2)_{\beta\beta'}, \tag{3.8}$$

where $\slashed{k}_1, \slashed{k}_2$ are momenta of created leptons and $\alpha\alpha', \beta\beta'$ are indices corresponding to polarization indices appearing in Dirac density matrix [27]. This relation is obtained using the Feynman rules with a high energy limit and without normalization.

As the density matrix is by default hermitian, we may rewrite it using $\rho(lep) = \rho^{\mu\nu}(lep)\gamma_\mu\gamma_\mu$. The component $\rho^{\mu\nu}(lep)$ can be rewritten in terms of components of original $k_1, k_2$ dilepton momenta. These momenta are combined in real and complex parts first of which has their symmetric combination, whereas the complex part has an antisymmetric one. In the rest frame of dilepton pair where $q^\mu = (q, \vec{0})$ the probe matrix can be rewritten as

$$\rho^{jk}(lep) = \frac{1}{3}\delta^{jk} + a\, J_p^{jk}\ell^p - b\, U^{jk}; \tag{3.9}$$

$$U^{jk}(\hat{\ell}) = \hat{\ell}^j\hat{\ell}^k - \frac{\delta^{jk}}{3}. \tag{3.10}$$

The formula for the probe density matrix obtains several nontrivial terms. The term $J_p^{jk}$ is a well-known rotation generator. Together with $a\,\ell^p$ it creates a tensor transforming as a spin-1 particle under rotations. The first term represents a tensor transforming as spin-0 and the third as spin-2. The second and third terms contain scalar variables $a, b$ dependent on transferred momentum $q^2$. These scalars depend on the vertex from which the dilepton pair originates.

Regarding the density matrix of the unknown intermediate system, we will observe only part coupling to the lepton density matrix via polarization indices. The observable part will be given by a projection of $\rho(X)$ onto a subspace coupled to the probe. In order to derive a similar formula as (3.9) for $\rho(X)$, let us begin with probe operators. The probe operators are orthogonal and measure a component of interest of the unknown system classified by its transformation properties, for studies of angular distributions, it is the transformation under rotation.

The generator of a group of rotations is the aforementioned $\vec{J}$. Given its orthogonality properties one gets $\frac{1}{2}\text{Tr}(\vec{\ell} \cdot \vec{J}\vec{S} \cdot \vec{J}) = \hat{\ell} \cdot \vec{S}$. With these notations, the density matrix can be written out similarly to the probe matrix is

$$\rho_{ij}(X) = \frac{1}{3}\delta_{ij} + \frac{1}{2}\vec{S} \cdot \vec{J}_{ij} + U_{ij}(X); \tag{3.11}$$

$$U(X) = U^T(X); \quad tr(U(X)) = 0. \tag{3.12}$$

The spin-0 components of density matrices are invariant under rotations. The spin-1 contribution of the second term is made out of parameters coupled to the angular momentum operator. The spin-2 contribution contains $U_{ij}(X)$ that measured the fluctuations in angular momentum. The definitions of density matrices mentioned above provide a clear comparison of these two matrices.

For estimation of parameters of $\rho(X)$, it is useful to apply the so-called Cholesky decomposition [28]. This decomposition preserves the positivity required by basic principles of quantum mechanics. The Cholesky decomposition decomposes the density matrix as $\rho = MM^\dagger$ with $M$ being a triangular matrix with real parameters on

its diagonal. The parameters inside $M$ are expected to take values between -1 and 1. The matrix for a three-dimensional case looks like

$$M(m) = \frac{1}{\sqrt{\sum_k m_k^2}} \begin{pmatrix} m_1 & m_4 + im_5 & m_6 + im_7 \\ 0 & m_2 & m_8 + im_9 \\ 0 & 0 & m_3 \end{pmatrix}. \qquad (3.13)$$

We thus have an array of numbers for the probe matrix and an array of parameters for the unknown density matrix.

There is one more variable that has not been mentioned and it is used in definitions of density matrices (3.9), (3.11) and that is the unit vector $\hat{\ell}$ that indicates the direction of lepton. This variable can be found from the kinematics of each event. Starting in the rest frame, and again in the high energy limit, of the dilepton pair, we may define a set of $x, y, z$ axes, that are orthogonal and together with the total pair momentum $q = k_1 + k_2$ give

$$q \cdot x = q \cdot y = q \cdot z = 0. \qquad (3.14)$$

Using vectors $P_A = (1, 0, 0, 1)$ and $P_B = (1, 0, 0, -1)$ for a description of colliding nuclei, one may get axes defining the Collins-Soper (CS) frame and satisfying orthogonality and (3.14)

$$\tilde{z}^\mu = P_A^\mu q \cdot P_B - P_B^\mu q \cdot P_A; \qquad (3.15)$$

$$\tilde{x}^\mu = q^\mu - P_A^\mu \frac{q^2}{2q \cdot P_A} - P_B^\mu \frac{q^2}{2q \cdot P_B}; \qquad (3.16)$$

$$\tilde{y}^\mu = \epsilon^{\mu\nu\alpha\beta} P_{A\nu} P_{B\alpha} q_\beta. \qquad (3.17)$$

Afterwards these vectors get normalized to a set $(x^\mu, y^\mu, z^\mu)$ that is further used for definition of $\hat{\ell}_J$. In general, $\ell_J$ is given by a difference of dilepton momenta with $J$ denoting the event. By multiplying $\ell_J$ by each of the CS axes defined above one gets $\vec{\ell}_{xyz,J}$ and after further normalization, $\hat{\ell}_J = (\sin\theta\cos\phi, \sin\theta\sin\phi, \cos\theta)$.

### 3.4.2 The Angular Distribution of Decay Products

So far we have defined a new reference frame, which is further discussed in Chapter 2 and density matrices of the probe and unknown system. These need to be further connected to the angular distribution in the final state. For that one has to make a connection between the angular distribution and cross-section and the density matrices. Again starting from the quantum mechanics, the cross-section is given by a squared matrix element $\mathcal{M}$ and for a scenario where $\chi_J$ describes the initial state (it is again defined event-by-event) and $f_{s,s'}$ describes the final state particles with spins $s, s'$, the cross-section is given as

$$d\sigma \sim \sum_{s,s'} \left| \sum_J \mathcal{M}(\chi_J \to f_{s,s'}) \right|^2 \cdot d\Pi_{LIPS}, \qquad (3.18)$$

$$= \text{Tr}\left[ \left( \sum_{s,s'} T^\dagger |f_{s,s'}\rangle\langle f_{s,s'}| T \right) \cdot \left( \sum_{J,K} |\chi_J\rangle\langle\chi_K| \right) \right] \cdot d\Pi_{LIPS}. \qquad (3.19)$$

In the formula, the matrix element is rewritten using the transfer matrix $T$ that is commonly used for studies of the propagation of wave functions. The $d\Pi_{LIPS}$

denotes Lorentz invariant phase space and originates from the Fermi golden rule. The terms seen in the formula can be rewritten using the density matrices. The first term in the trace of the last line in (3.19) refers solely to the final state particles and by definition defines the density matrix of the probe. Similarly, the second term in the trace describes the unknown matrix $\rho(X)$. In order to infer the connection between angular distribution and cross-section, the cross-section can be rewritten as

$$k_0 k_0' \frac{d\sigma}{d^3 k d^3 k'} = \frac{d\sigma}{d^4 Q d\Omega}, \tag{3.20}$$

where the term on the left describes the probability to find a lepton pair with variables $q, \ell$ give a set of initial state variables $P(q, \ell | init)$. This probability can be rewritten in terms of conditional probabilities $P(\ell | q, init)$ and $P(q | init)$ yielding a formula for angular distribution

$$\frac{dN}{d\Omega} = \frac{1}{\sigma} \frac{d\sigma}{d\Omega} = P(\ell | Q, init) = \frac{3}{4\pi} \text{Tr}(\rho(\ell)\rho(X)). \tag{3.21}$$

Writing out the terms from each density matrix and using the parameters from $\rho(X)$ the angular distribution in the final state can be written as

$$\begin{aligned}
\frac{dN}{d\Omega} = \ & \frac{1}{4}(1 + m_3^2) \\
& + 0.22 m_3 m_9 \sin\theta \cos\phi \\
& - 0.22 m_3 m_7 \sin\theta \sin\phi \\
& + 0.22(m_2 m_5 + m_7 m_8 - m_6 m_9) \cos\theta \\
& + \frac{1}{4}(1 - 3m_3^2) \cos^2\theta \\
& - \frac{1}{2} m_3 m_6 \sin(2\theta) \cos\phi \\
& + \frac{1}{2}\left(m_2^2 + m_8^2 + m_9^2 + \frac{1}{2}m_3^2 - \frac{1}{2}\right) \sin^2\theta \cos(2\phi) \\
& - \frac{1}{2}(m_2 m_4 + m_8 m_6 + m_7 m_8) \sin^2\theta \sin(2\phi) \\
& - \frac{1}{2} m_3 m_8 \sin(2\theta) \sin\phi.
\end{aligned} \tag{3.22}$$

The whole procedure is shown in [13]. In order to obtain the parameters $m_\alpha$ of the density matrix, one has to fit such distribution to the measured data. The fitting procedure (either MLM or $\chi^2$) has one great advantage in this case. As was already mentioned, when minimizing $\chi^2$ (or maximizing likelihood), one may come across a problem of finding several local extrema. While fitting the density matrix, this problem of so-called convex optimization is solved due to the convexity of measured trace $\text{Tr}\rho(\ell)\rho(X))$. Thus any observed local extremum will be also a global extremum.

For further simplification of yielding the density matrix, it is convenient to study the properties of said matrix under discrete transformations amongst which we consider parity $P$, time reversal $T$ and charge conjugation $C$. $P$ transformation describes a change of the coordinate system with respect to its origin while changing the sign of axes. The terms that change sign under the parity transformation in (3.22)

are contributions from $\sin\theta\sin\phi, \sin 2\theta\sin\phi, \sin^2\theta\sin 2\phi$. The fact that we may observe only some terms under a given discrete transformation gives an opportunity to study violations of these symmetries. By applying a basic property of density matrix $\mathrm{Tr}(\rho(X)) = 1$ and considering the parity conservation (parity is conserved in QCD and QED), five additional parameters in (3.22) are eliminated and only three parameters $m_2, m_3, m_6$ while 2 are independent. This results in a simplification

$$
\begin{aligned}
\frac{dN}{d\Omega} = \; & \frac{1}{4}(1 + m_3^2) \\
& + \frac{1}{4}(1 - 3m_3^2)\cos^2\theta \\
& - \frac{1}{2}m_3 m_6 \sin(2\theta)\cos\phi \\
& + \frac{1}{2}(m_2^2 + m_8^2 + m_9^2 + \frac{1}{2}m_3^2 - \frac{1}{2})\sin^2\theta\cos(2\phi) \\
& - \frac{1}{4}(2m_2^2 + m_3^2 + -1)\sin^2\theta\sin(2\phi).
\end{aligned}
\tag{3.23}
$$

This can be further simplified by the normalization as

$$
m_3 m_6 = \sqrt{m_3^2(1 - m_2^2 - m_3^2)}.
\tag{3.24}
$$

As the fitting of a 2D distribution (3.22) or (3.23) can be rather cumbersome, it is often convenient to provide a 1D fit in two variables $\phi$ and $\cos\theta$. As the differential $d\Omega$ can be by definition rewritten as $d\cos\theta \cdot d\phi$, one may calculate the distributions in these variables by integrating (3.22) or (3.23) over $\phi$ in the $(0, 2\phi)$ interval (to yield $\frac{dN}{d\cos\theta}$ and over $\sin\theta$ for $\theta$ in $(0, \pi)$.

### 3.4.3 Density Matrices and Polarization Studies

As already mentioned, quantum tomography provides a unique opportunity to study processes while omitting any model. It allows using only quantities that are measured and constructs density matrices that contain all possible information. These are tools for further studies under symmetry groups.

In Chapter 2 we discuss the traditional approach to polarization studies and its disadvantages. Using the density matrices, the obtained results are independent of the frame, contrary to traditional approaches. This is given by the fact, that the coordinates for leptons, even though they depend on conventions for $x, y, z$, are Lorentz scalars. However, it is possible to connect density matrices and traditional conventions with $\lambda_k$ as denoted in 2 by comparing (2.6) and (3.23) we get, using only independent terms of $\rho(X)$

$$
m_3^2 = \frac{1 - \lambda_\theta}{\lambda_\theta + 3},
\tag{3.25}
$$

$$
m_2^2 = \frac{2\lambda_\phi + \lambda_\theta + 1}{\lambda_\theta + 3},
\tag{3.26}
$$

$$
\lambda_{\theta\phi} = -\frac{1}{2}\sqrt{(1 - \lambda_\theta)(\lambda_\theta - 2\lambda_\phi + 1)}.
\tag{3.27}
$$

# Chapter 4

# Ultra-peripheral Collisions

The source of vector mesons for further analysis of polarization are relativistic collisions of heavy ions, specifically Pb. The nuclei of a heavy element are collided at relativistic speeds while following an approximately straight line in the vicinity of the interaction point. Based on the perpendicular distance between the centres of colliding nuclei, the collisions can be grouped into three groups. This separation is called impact parameter $b$. If the collision is head-on, the impact parameter is $b \sim 0$, the collision is called central. For $b \lesssim R_A + R_B$ with $R_A, R_B$ being the radii of colliding nuclei. The last group are ultra-peripheral collisions (UPC), the schematic of such collisions is shown in Figure 4.1. The schematic shows two colliding nuclei with impact parameter larger than the sum of their radii.
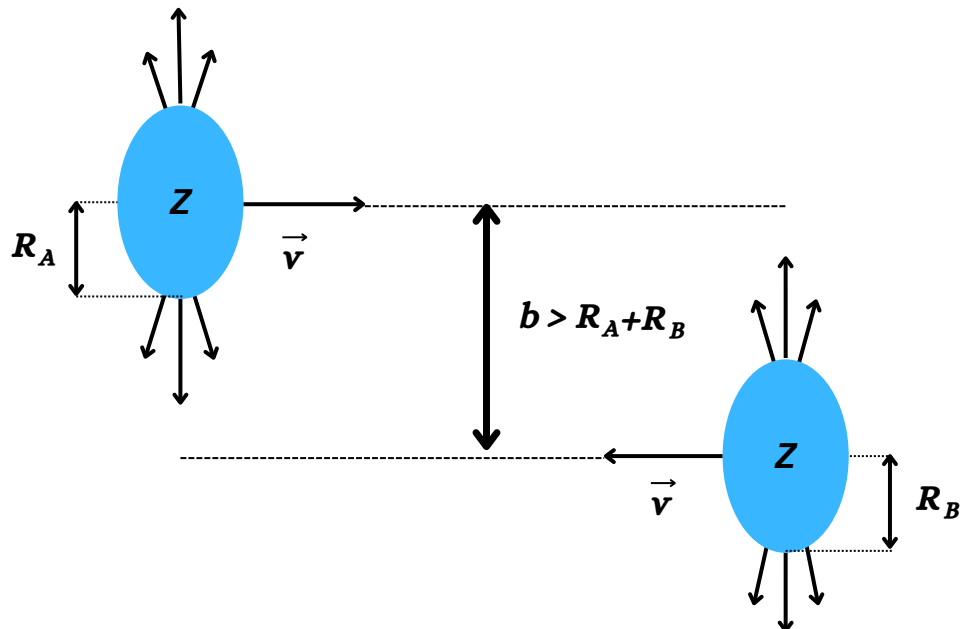


**Figure 4.1:** Schematic of UPC with $R_A(R_B)$ being the radii of colliding nuclei, $\vec{v}$ colliding speed, $Z$ corresponding charges and $b$ the impact parameter.

The UPCs are beneficial due to the large suppression of interaction mediated by the strong force acting between hadrons. Thus the interaction between nuclei is mediated solely by photons in their respective electromagnetic fields. The probability of no hadronic interactions to occur can be inferred from assuming that the density of nuclei is distributed by a Wood-Saxon distribution $\rho(b)$ yielding the nuclear thickness function $T_A(\vec{b})$ [29]

$$\rho(b) = \frac{\rho_0}{1 + \exp(\frac{b - r_A}{z_0})}, \qquad T_A(\vec{b}) = \int dz \rho(\sqrt{|\vec{b}|^2 + z^2}), \qquad (4.1)$$

where $b$ is the impact parameter and $z$ is the longitudinal direction of travel of the nucleus. The probability of no hadronic interaction to occur is given by

$$P_{NH}(b) = \exp(-T_{AA}\sigma_{NN}), \qquad (4.2)$$

where $T_{AA}$ is the nuclear overlap function and $\sigma_{NN}$ is the inelastic cross-section of a collision of two nuclei. This probability is determined using the fact, that it is a Poisson process with a mean given by the probability of interaction multiplied by the nuclear overlap. The dependence of such probability on impact parameter for $\sigma_{NN} = 64$ mb is shown in Figure 4.2 with the probability being zero for impact parameter bellow 14 fm.
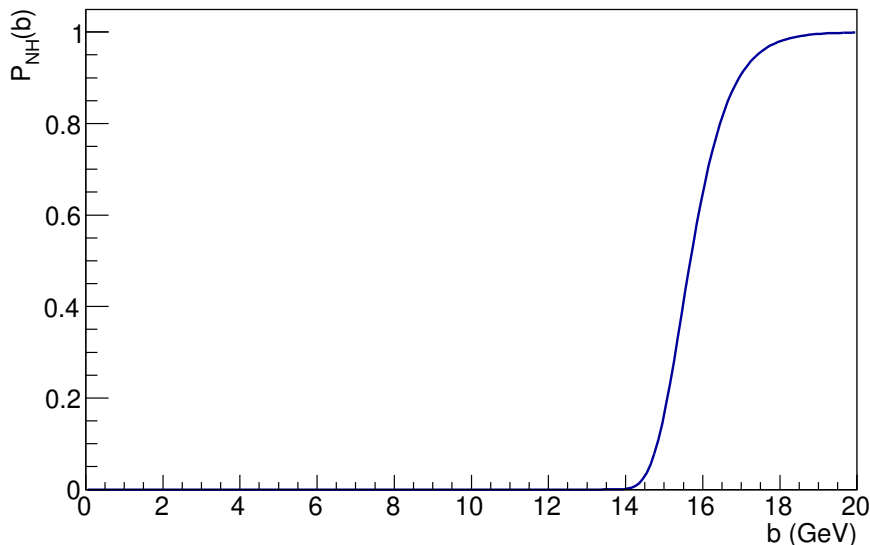


**Figure 4.2:** The probability $P_{NH}$ of no hadronic interaction to occur for a given impact parameter $b$ [29].

The impact parameter of a collision is not directly measurable, however, the collision can be characterized by a set of selection criteria using measurable parameters.

The interaction in UPC is thus electromagnetic, mediated by photons in the fields of nuclei. Even though the electric field is emitted coherently by the whole nucleus, they are affected by acceleration. The relativistic speeds of nuclei cause a Lorentz contraction of said field in the longitudinal direction, the direction of motion, where the maximum possible momentum is multiplied by a Lorentz factor $\gamma_L$ dependent on the speed of nuclei. Moving charged nuclei generate also a magnetic field, that is perpendicular to an electric field. These interactions can lead to the production of new particles.

The creation of new particles in these processes is called photoproduction. The Feynman diagram of photoproduction of J/$\psi$ vector meson is shown in Figure 4.3. The figure depicts two contributions to the vector meson photoproduction, where one of the nuclei acts as a target for a photon coming from the second nuclei and vice versa. The nuclei take turns in photon emission.
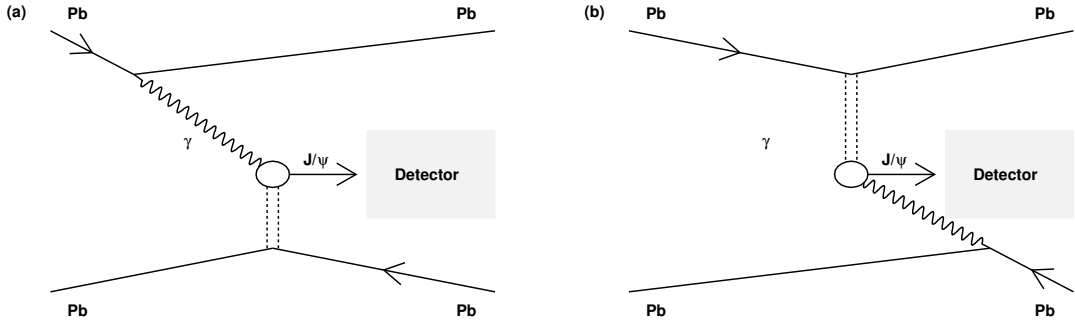


**Figure 4.3:** Feynman diagrams contributing to J/$\psi$ photoproduction in ultra-peripheral Pb-Pb collision [29].

The photoproduction process has two steps. Before interacting with the target, the photon fluctuates into a quark-antiquark ($q\bar{q}$) pair, which later interacts with the nucleus via the strong interaction. The preferable result is a vector meson with quantum numbers $J^{PC} = 1^{--}$, the same as of a photon. This type of process is a good way for observation of exclusive vector meson production, where only a vector meson appears in the final state, i.e. $A + A \to A + A + VM$.

The wavelength of interacting photons has a great impact on the type of collision. For wavelengths in the order of magnitude of the radius of the target, the $q\bar{q}$ pair interacts with a whole nucleus by coherent coupling to the electromagnetic field of the target. These collisions are called coherent and are specified by a transverse momentum of a resulting vector meson of $p_T \sim 1/2R_A$. This value of transverse momentum together with no additional nuclear breakup implies that in the transverse plane, the topology of an event will be well-defined and clean.

The resulting vector meson cannot be measured directly, due to its short lifetime. It is detected via its decay products, where given the well-defined topology, there will be only the decay products in an otherwise empty detector emitted back-to-back. The same resulting decay products as from the decay of J/$\psi$ are expected from a two-photon process, that is considered as an irreducible background.

For wavelengths in the order of nucleon radius, photons interact with nuclear constituents and the interaction is denoted as incoherent. A smaller radius of a nucleon, in comparison with a nucleus, results in large transverse momenta of the vector meson. This collision is thus accompanied by nuclear breakup followed by a neutron emission in the forward direction.

The nuclear breakup may also appear in the case of coherent production as a result of strong electromagnetic fields. These fields may excite the target nucleus, which will emit a neutron after the collision.

As mentioned, the photoproduction is a two-step process. This allows for a factoriza-

tion of such a process into a vertex described by Quantum Electrodynamics (QED), as only photons are involved, and the other part described by Quantum Chromodynamics (QCD) where gluons enter. The resulting cross-section of such collision can be generally given as

$$\frac{d\sigma_{PbPb}(y)}{dy} = N_{\gamma/Pb}(y, M)\sigma_{\gamma Pb}(y) + N_{\gamma/Pb}(-y, M)\sigma_{\gamma Pb}(-y), \qquad (4.3)$$

where $N_{\gamma/Pb}$ is a flux of photons and $\sigma_{\gamma Pb}$ is a photonuclear cross-section.

## 4.1   Photon Flux

As mentioned above, the electric and magnetic components of electromagnetic fields of nuclei are transverse to each other. In the transverse plane, with respect to the direction of motion of nuclei, the components are of similar magnitude and the target particle placed close to the passing particle is affected by these in a similar way as by a plane electromagnetic wave. It was pointed out by Fermi in 1924 that this wave can be approximated by the flux of virtual photons whose intensity is given by the square of the charge of the moving nuclei $Z$. This method was independently extended by Weizsäcker and Williams and denoted Equivalent Photon Approximation (EPA).

This approach describes the interaction of two nuclei via the interaction of two-photon clouds surrounding the colliding nuclei. These photons mediate a long-range interaction that allows not only for interaction between two photons but also for interaction between a photon and nucleon inside opposite nuclei without nuclear overlap. The EPA is a good approximation for the computation of a cross-section of electromagnetic processes.

The energy of interacting photons depends on the time spent by a target in the vicinity of the colliding nucleus. This can be interpreted in terms of impact parameter to yield maximum energy of a photon in a lab frame as [30]

$$\omega^{max} = \frac{\hbar}{\Delta t} \sim \frac{\hbar\gamma v}{b}, \qquad (4.4)$$

where $\Delta t$ is the mentioned time. For UPCs of heavy nuclei, this value is about $0.3/A$ of the energy of the ion. This formula furthermore shows a dependence of the photon energy on the velocity of the colliding nuclei. Thus the collisions and ultra-relativistic speeds give high enough energy for photons to result in the photoproduction of massive vector mesons or heavy quarks with high interaction rates.

The number of photons per unit area is given by the impact parameter of a collision as

$$N(\omega, b) = \frac{Z^2\alpha\omega^2}{\pi^2\gamma^2\hbar^2\beta^2c^2}\left(K_1^2(x) + \frac{1}{\gamma^2}K_0^2(x)\right), \qquad (4.5)$$

where $x = \omega b/\gamma\beta\hbar c$. The functions $K_1^2$ and $K_0^2$ are Bessel functions describing a flux of photons that are transversely and longitudinally polarized, respectively. The $1/\gamma^2$ factor denotes the effects of Lorentz contraction on colliding nuclei, where for ultra-relativistic particles, where $\gamma \gg 1$, the longitudinally polarized photons are suppressed. This allows for the assumption that the bulk of interacting photons are transversely polarized.

The total photon flux is given by an integral over all impact parameters while taking into account the impact parameters where no hadronic interaction takes place. For UPCs of heavy nuclei, one can utilize the so-called hard sphere approximation. This approximation considers interacting nuclei as hard spheres for $b > 2R_A$ and yields the total photon flux by integrating over impact parameter $b > b_{min} = 2R_A$ [30]

$$n(\omega) = \frac{2Z^2\alpha}{\pi\beta^2}\left[\xi K_0(\xi)K_1(\xi) - \frac{\xi^2}{2}\left(K_1^2(\xi) - K_0^2(\xi)\right)\right],\qquad(4.6)$$

where $\xi = 2\omega R_A/\gamma\beta\hbar c$.

## 4.2  Photonuclear Cross-Section

The photonuclear cross-section is determined by theoretical predictions from several models. These models can be grouped based on their theoretical origin. Most of them can be categorized into three groups.

### 4.2.1  Vector Meson Dominance Models

The Vector Meson Dominance (VMD) assumptions are based on observed similarities between photon-photon and hadron-hadron interactions. Even though this resemblance is unexpected assuming differences between strong and electromagnetic interaction. Studying the behaviour of total cross-sections showed that both processes display resonances at low energies and above a certain threshold they level out. Furthermore, photon-hadron interactions show no difference between proton or neutron, similar to strong interactions. Other similarities are for example the absorption by a nucleus or the behaviour of non-diffractive interactions.

These unexpected similarities led to an assumption that the physical photon can be understood as a superposition of a bare photon interacting solely via electromagnetic interaction and of components corresponding to hadronic components. The decomposition is as follows [30]

$$|\gamma\rangle = C_{bare}|\gamma_{bare}\rangle + C_\rho|\gamma_\rho\rangle + C_\phi|\gamma_\phi\rangle + \cdots + C_{q\bar{q}}|\gamma_{q\bar{q}}\rangle.\qquad(4.7)$$

Each of these states inherits the same quantum numbers as the photon due to state invariance. The bare photon couples to the electromagnetic part of the conserved current, whereas the vector mesons to the hadronic ones correspond to isospin, baryon number and hypercharge. The photon-vector meson coupling, $f_V$, is given by the fact that the photon has to couple with the strength given by the electromagnetic coupling constant $\alpha$. both of these constants are part of the amplitude corresponding to photon-VM fluctuation

$$|C_V|^2 = \frac{4\pi\alpha}{f_V^2} = \frac{3\Gamma_{V\to l^+l^-}}{\alpha^2 M_V},\qquad(4.8)$$

where $\Gamma_{V\to l^+l^-}$ is the measured dilepton decay width. Furthermore, this relation shows, that for heavy vector mesons, this amplitude is very low.

A great power of VMD is its ability to connect scattering amplitudes of photonuclear processes, $\gamma N \to X$, of highly energetic photons to amplitudes of similar processes with VM, $VN \to X$. This connection is expected only for processes, where the photon fluctuates to a $q\bar{q}$ pair of the same type as the resulting VM. In order to describe processes where the types of mesons differ, a more general approach called Generalized Vector Meson Model is used. In the nuclear rest frame, these processes are connected as [30]

$$\frac{d\sigma(\gamma + \mathrm{Pb} \to V + \mathrm{Pb})}{dt} = C_V^2 \frac{d\sigma(V + \mathrm{Pb} \to V + \mathrm{Pb})}{dt}. \tag{4.9}$$

The cross-section corresponding to $\gamma A \to VA$ can be rewritten using a form factor, $F(t)$ and forward scattering amplitude. The form factor is given by the nucleus as it is obtained by Fourier transformation from the nuclear density distribution. Using the optical theorem for relating the forward scattering amplitude and the total cross-section one obtains [31]

$$\left.\frac{d\sigma(\gamma + \mathrm{Pb} \to V + \mathrm{Pb})}{dt}\right|_{t=0} = \frac{\alpha \sigma_{TOT}^2(\mathrm{Pb} + V)}{4f_V^2}. \tag{4.10}$$

The total cross-section $\sigma_{TOT}(Pb + V)$ is given by a classical Glauber model. The model was designed to describe high-energy scattering with composite particles. It requires inputs from experimental data such as the energy dependence of the inelastic nucleon-nucleon scattering and the densities of nuclear charge. The model looks at the interaction of 2 nuclei as individual interactions of its constituents and allows us to define the total cross-section

$$\sigma_{TOT}(\mathrm{Pb} + V) = \int d^2\vec{b}(1 - \exp[-\sigma_{TOT}(p + V)T_{Pb}(\vec{b})]), \tag{4.11}$$

where $T_{Pb}(\vec{b})$ is the nuclear thickness function dependent on the impact parameter.

### 4.2.2  Leading Order Perturbative QCD Models

The models based on Leading order (LO) perturbative QCD (pQCD) use pQCD to calculate the forward scattering amplitude with [31]

$$\left.\frac{d\sigma(\gamma + \mathrm{Pb} \to V + \mathrm{Pb})}{dt}\right|_{t=0} = \frac{16\pi^3\alpha_s^2\Gamma_{ee}}{3\alpha M^5}\left[xG_A(x, Q^2)\right]^2, \tag{4.12}$$

where $\Gamma_{ee}$ is the decay width corresponding to decay to electrons and $G_A$ is the gluon distribution function inside nucleus dependent on $Q^2$ scale and Bjorken-$x$. This shows that by measuring the cross-section of these processes we may study the gluon distribution functions by fitting to data. The $G_A(x, Q^2)$ can be parameterized by the nuclear modification factor of the gluon distribution, $R_g^A$ and a function describing the gluon distribution inside proton, $g_p(x, Q^2)$.

### 4.2.3  Colour Dipole Models

The colour dipole is a structure made of $q\bar{q}$ pair that originates from photon fluctuation. It is expected that this dipole creation takes place a long time before its

further strong interaction with the target resulting in the formation of vector meson. The theory of colour dipoles holds only for small Bjorken-$x$ ($x < 0.02$). The cross-section of photonuclear interaction is based on a dipole cross-section. This dipole cross-section is defined as

$$\frac{d\sigma_{\text{dip}}}{d^2\vec{b_T}} = 2N(x_P, \vec{r_T}, \vec{b_T}), \tag{4.13}$$

where $N(x, \vec{r}, \vec{b})$ is a dipole-proton amplitude. The estimation of this amplitude is based on proper factorization. The amplitude satisfies Balitsky-Kovchegov (BK) evolution equation. This equation is crucial for the description of the evolution of a wave function of the virtual photon or for the evolution of the gluon distribution function inside hadrons. The initial conditions of the BK equation can be fitted to measured data and its solution can be used to compute the amplitude. Whereas this approach seems rather easy and straightforward, the impact parameter dependence presents a problem as this dependence in the BK equation leads to a growth in the size of the proton without any physical reasoning.

This requires a factorization of the dependence. This can be done in several ways using phenomenology one of which is the IIM parametrization [32]

$$\frac{d\sigma_{\text{dip}}}{d^2\vec{b_T}} = 2T(\vec{b_T})N(x_P, \vec{r_T}), \tag{4.14}$$

where the $T(\vec{b_T})$ once again describes the profile density. This approximation utilizes important features of the BK equation and employs parameters based on measurements, for example from HERA. Other possible parametrization is the IPsat model that uses eikonalized Dokshitzer-Gribov-Lipatov-Altarelli-Parisi (DGLAP) evolution equation describing the evolution of gluon distribution functions. The result of this approximation is [33]

$$\frac{d\sigma_{\text{dip}}}{d^2\vec{b_T}} = 2\left[1 - \exp{-r^2 F(x, r)T_p(\vec{b_T})}\right], \tag{4.15}$$

where $F(x, r)$ is the aforementioned gluon distribution from DGLAP.

This cross-section is further transformed by Fourier transformation in order to obtain the imaginary part of scattering amplitude dependent on the momentum transfer $\Delta_T$ instead of the impact parameter. It also inherits the dependence on Bjorken-$x$ which for the probed gluon is $x_P = M_V e^{-y}/\sqrt{s_{NN}}$. It is further contracted by a possible overlap of wavefunctions describing the photon fluctuating to $q\bar{q}$ pair and the formation of vector meson. This is often parametrized by Gauss-dependent parametrizations such as the Boosted Gaussian or Gauss-LC. The amplitude is further averaged and used in the vector meson production cross-section

$$\frac{d\sigma^{\gamma A \to VA}}{dt} = \frac{R_g^2(1+\beta^2)}{16\pi}\langle|A(x_P, Q^2, \Delta_T)|^2\rangle_N. \tag{4.16}$$

The $R_g$ is a correction applied due to the observed skewdness effect that is observed due to different $x_P$ of target gluons.

The predictions of cross-sections in the colour dipole model framework with inputs from HERA measurements can be seen in Figure 4.4. The right-hand side picture

shows predictions based both on IIM and fIPsat parametrisations. The blue and black lines correspond to Boosted Gaussian and Gauss-LC amplitude parametrization, respectively. The prediction shows the same crucial dependence on rapidity as the data with different normalizations causing the prediction to be higher than the measured data. The most favourable model is the fIPsat model with Gauss-LC. The difference is expected to be caused by the skewedness factor as it is based on measurements from HERA that are measured at different $x$. The prediction for incoherent production (left-hand side) shows again variations in normalization while displaying similar rapidity dependence.
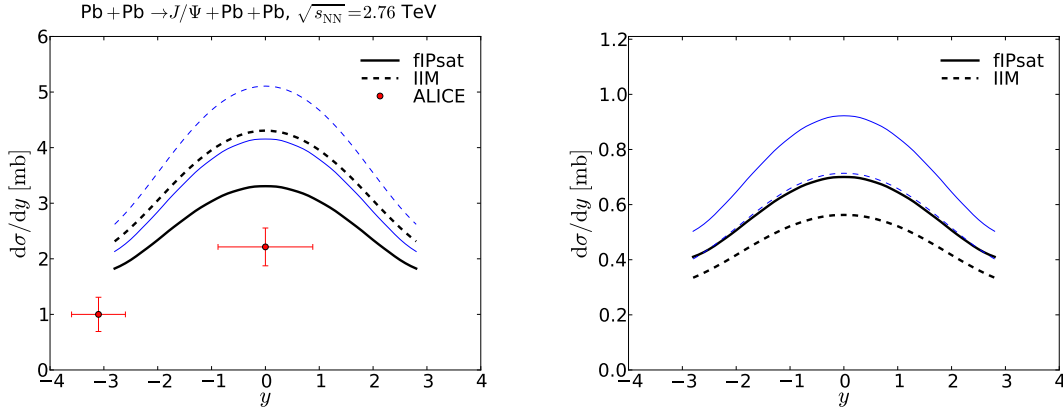


**Figure 4.4:** (Left) Prediction for coherent photoproduction of J/$\psi$ for Pb-Pb collisions at $\sqrt{s_{NN}} = 2.76$ TeV. Compared with measured data by the ALICE experiment. (Right) Prediction for incoherent photoproduction of J/$\psi$ for Pb-Pb collisions at $\sqrt{s_{NN}} = 2.76$ TeV [34].

## 4.3 Two-Photon Processes

The two-photon processes in UPC are governed by QED. A Feynman diagram of such a process is shown in Figure 4.5. For the purposes of this analysis are these processes considered as an irreducible background of processes of interest. The two emitted photons fuse into new particles, in this case, a dielectron or dimuon pair. The fusion of the tau lepton pair has not been performed yet.

The cross-section of such processes can be described in similar a way as in the previous case. It is dependent on the photon flux coming from each colliding nucleus. It is defined as [35]

$$\sigma_{\gamma\gamma} = \frac{\pi\alpha^2}{4s}\beta \left[ \frac{3-\beta^4}{2\beta} \ln \frac{1+\beta}{1-\beta} - 2 + \beta^2 \right]. \tag{4.17}$$

These photon fluxes described by the EPA are folded together to gain luminosity. Their strength depends on the charge of colliding nuclei which plays a significant role in higher-order terms of QED. The so far measured two-photon processes at the LHC have been well described by the STARLIGHT generator including only the leading order terms.
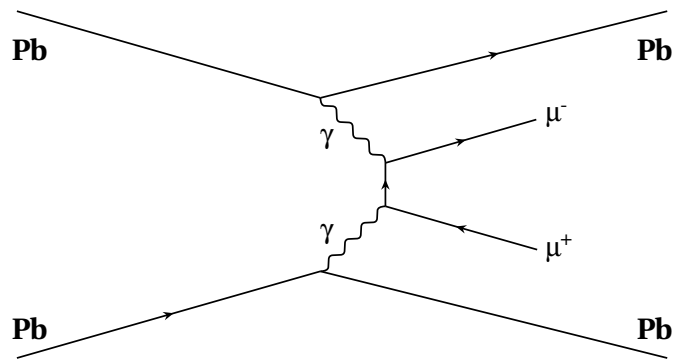
**Figure 4.5:** Feynman diagram of a two-photon process contributing to a dilepton signal in Pb-Pb collisions [31].

# Chapter 5

# The ALICE Experiment at the LHC

CERN, the European Organization for Nuclear Research, brings together scientists from around the world to search for answers to fundamental questions concerning the laws of nature together with technological development in a vast amount of fields. CERN was founded in 1954 with 12 member states. This number increased to 23 as of 2018. During its operation, the facility enabled several remarkable achievements such as the discovery of the W, Z bosons and Higgs boson, the creation of antimatter and the World Wide Web [36]. These achievements along with developments in technology made a huge impact not only on the world of physics but worldwide.

## 5.1 Large Hadron Collider (LHC)

The Large Hadron Collider (LHC) is situated 100 m underground on the Franco-Swiss border and is a part of the CERN accelerator complex depicted in Figure 5.1. With its 27 km in circumference, it is so far the largest accelerator in the world. Its operation is not continuous. The periods of operation, called Runs, are disrupted by Long Shutdowns, which are crucial for repairs and further development not only of the LHC but also of the experiments.

The main focus of this thesis is on the data from the Run2 period, which took place between 2015 and 2018. During this period lead beams achieved the energy of 5.02 TeV per nucleon pair and in 2018 even reached the energy of 6.37 TeV with more than twice the luminosity than in 2015 [37].

The accelerator complex provides accelerated ions (Pb, Xe, Ar and O in the future), protons, neutrons and electrons for a variety of target and collider experiments. The succession of accelerators differs slightly according to the type of accelerated particle. The acceleration of lead ions begins with a source of vaporized lead, that is created in plasma. The ions start their journey in Linac3 which is a linear accelerator used for first acceleration and at the end it strips the lead ions to bare nuclei and sends them in long pulses to LEIR (Low Energy Ion Ring). LEIR not only accelerates the ions, but it creates shorter and denser bunches of heavy ions. With bunches of ions with desired properties, the acceleration continues in PS (Proton Synchrotron), SPS
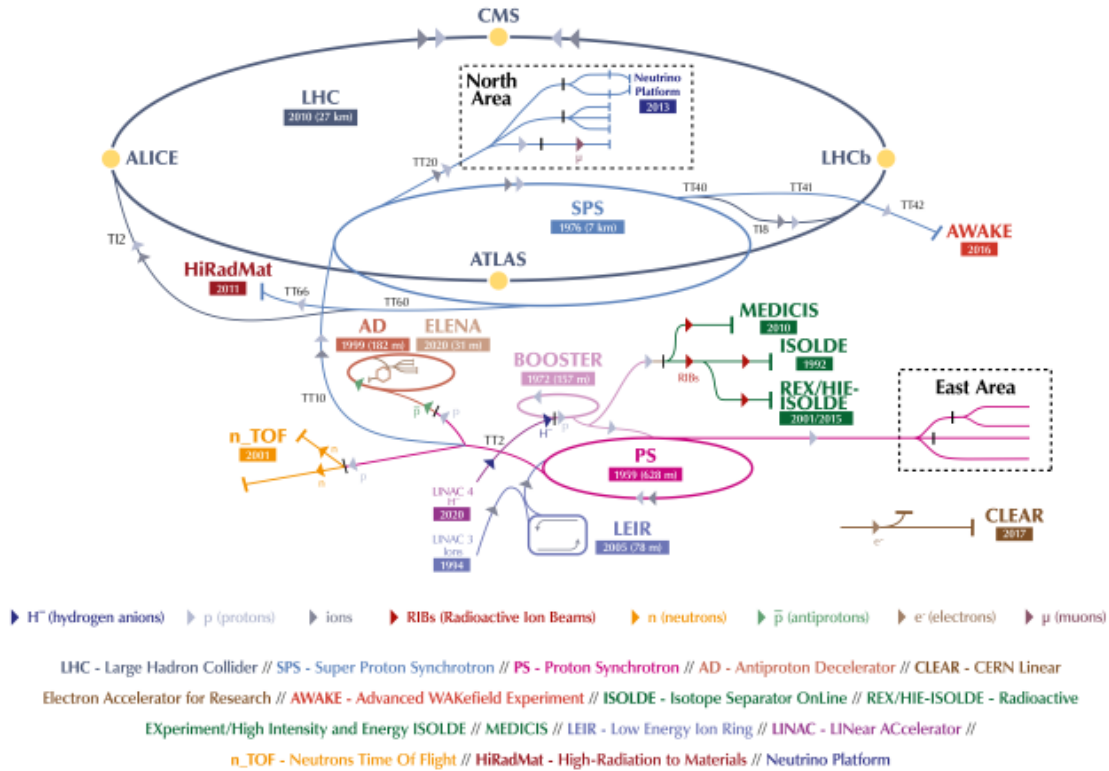
**Figure 5.1:** Display of the CERN accelerator complex showing various experiments and accelerators described in text [38].

(Super Proton Synchrotron) and finally in LHC. Particles in LHC are accelerated in opposite directions and when they acquire desired energy, they are collided in one of the experiments.

Fixed-target experiments at CERN research wide area of new physics phenomena such as the interaction between visible and dark matter (NA64), phase transition of matter (NA61/SHINE) or decays of kaons (NA62). Furthermore, there are several antimatter experiments, e.i. AEGIS, ALPHA or ASACUSA. There are also several facilities focusing on neutrinos (n-TOF) or medicine (MEDICIS).

Regarding the collider experiments, there are in total 9 experiments at LHC, 5 small and 4 large experiments. Small experiments such as TOTEM and LHCf are focusing on forward physics. The FASER and SND@LHC are focusing on studies of light particles and neutrinos and MoEDAL-MAPP on the search of magnetic monopoles.

Large experiments are focusing on a variety of phenomena. ATLAS and CMS are general-purpose detector systems oriented for example on the search for the Higgs boson. The LHCb experiment, on the other hand, is focusing on the CP violation and studies of the difference between matter and antimatter through the b quark. The last large experiment is the ALICE experiment.

## 5.2 ALICE experiment

ALICE (A Large Ion Collider Experiment) is a general-purpose detector system focusing on the study of strongly interacting matter together with the properties of QGP in nucleus-nucleus collisions. Furthermore, ALICE takes data during pp runs and cosmics in order to get reference data not only for collisions of heavy ions but for complementary reasons to the other experiment on the LHC.

The overall design of the experiment depends on the desirable performance and physics observables. In order to measure medium at high energy densities, ALICE focuses on physics in the vicinity of midrapidity. The number of particles observed at midrapidity for heavy ions is large. This high multiplicity is one of the most important aspects when designing the ALICE experiment. The precise measurement of multiplicity allows for the determination of the geometry of the collision, which furthermore results in the impact parameter or orientation of the collision volume determination. It also puts large demands on the speed of data acquisition that reaches up to 1.3 GB/s [39].

Other crucial observables are for example nuclear modification factors or studies of jets and heavy flavour production. These need accurate measurements of parton energy loss and kinematics in QGP together with a large acceptance. This calls for precise tracking. On ALICE the tracking is measured using information about hits in three dimensions in a large dynamic range to observe the collective behaviour of the medium. The density of tracks reaches high values that put high requirements on the tracking system such as high granularity of the detector or on the outer magnetic field, that is expected to be low. The acceptance is large enough to measure jets and resonance decays even at low momenta while having a low material thickness to decrease multiple scattering.

The ALICE experiment is situated underground with a beamline at 44 m [39]. The size of the experiment is predominantly determined by a large L3 solenoid magnet. This magnet houses central barrel detectors. In the vicinity of the solenoid is a dipole magnet placed 7 m from the interaction vertex. The dimensions of ALICE experiments are $16 \times 16 \times 26$ m$^3$ with the weight of 10 000 t [39]. The details on ALICE subdetectors and data acquisition for Run2 are given in further text.

### 5.2.1 Inner Tracking System

The Inner Tracking System (ITS) of the ALICE detector is the innermost detector in the central barrel. It consists of six cylindrical layers of coordinate-sensitive silicon detectors whose position is determined by the layout of other detectors, expected particle density, requested track efficiency and impact parameter resolution. The innermost layer is located around the beampipe whereas the position of the outermost layer is given by the TPC (Time Projection Chamber) in order to be able to perform track matching of ITS and TPC. For low-momentum particles, the ITS takes over the particle identification (via $\mathrm{d}E/\mathrm{d}x$ measurement) from the TPC as well as at small radii where the track densities reach up to 90 cm$^{-2}$ [41].

The high density of tracks can result in a large effect from multiple scattering. The ITS lowers these effects by having truly two-dimensional devices in the four

# THE ALICE DETECTOR

1. ITS
2. FMD, T0, V0
3. TPC
4. TRD
5. TOF
6. HMPID
7. EMCal
8. DCal
9. PHOS, CPV
10. L3 Magnet
11. Absorber
12. Muon Tracker
13. Muon Wall
14. Muon Trigger
15. Dipole Magnet
16. PMD
17. AD
18. ZDC
19. ACORDE

a. ITS SPD (Pixel)
b. ITS SDD (Drift)
c. ITS SSD (Strip)
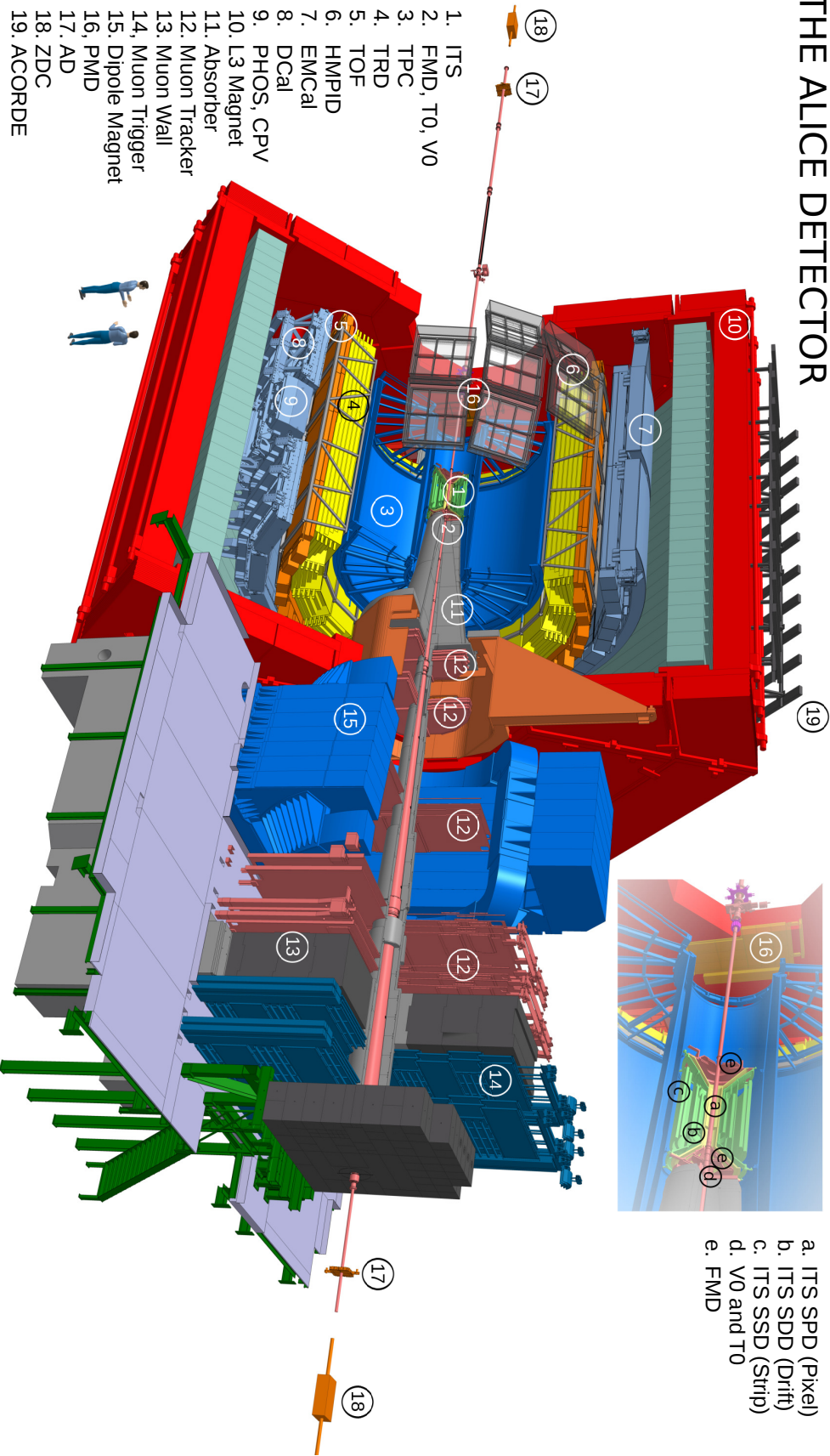d. V0 and T0
e. FMD

**Figure 5.2:** Schematics of the ALICE experiment for Run2 [40].

42

innermost layers. Due to its ability to measure low-momentum particles, the ITS enables the widening of the momentum range of measured particle spectra.

Another application of the ITS is vertex determination. ITS is capable of measuring not only primary vertices, which together with the first track point improve momentum angle measurements of the TPC, but also secondary vertices. Secondary vertex identification allows for the detection of charm and hyperon decays, for example, the $D$ mesons by reconstruction of their full decay topology.

The ITS layers can be divided into pairs, each pair of a different type. The inner pair is SPD (Silicon Pixel Detector), the middle is SDD (Silicon Drift Detector) and the last pair is SSD (Silicon Strip Detector) [41]. The choice of silicon detectors was based on desired high granularity and good spatial resolution of the detector. This further affects the resolution of impact parameter measurement.

### 5.2.2 Time Projection Chamber

The Time Projection Chamber (TPC) is a crucial detector of the ALICE experiment for particle identification. The design of the detector allows the handling of several hundred events per second even for an interaction rate of 8 kHz which is the maximum interaction rate for Pb-Pb in Run2. It surrounds the previously mentioned ITS detector, which allows it to match its acceptance in pseudorapidity ($|\eta| < 0.9$ [42]), furthermore it covers the full $2\pi$ angle in azimuth.

The layout of the TPC is shown in Figure 5.3. As shown, the TPC has a cylindrical shape with an inner radius given by the ITS (80 cm) and an outer radius is about 250 cm [42]. The field cage of the TPC consists of 4 vessels, that in two pairs create the outer and inner field cages. These field cages are designed with low overall thickness in order to optimize detector performance while providing a stable structure for other detector elements. This stability is calibrated by lasers.
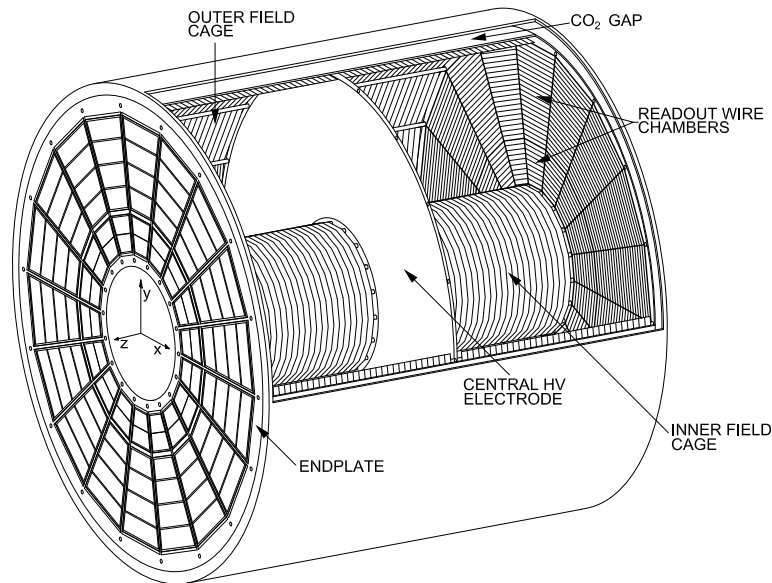


**Figure 5.3:** The layout of the TPC detector [43].

In the middle of the detector, a high voltage electrode that provides a uniform field parallel to the detector axis is placed. Uniformity of the electric field is essential as electrons forming the signal drift through this field to the endplates with installed readout chambers.

The large volume of the TPC has filled with Ne-C0$_2$-N$_2$ gas mixture. This mixture was chosen according to several aspects. Neon showed good diffusion abilities of the drifting electrons and thus was chosen as a main component. CO$_2$ plays the role of a quenching gas and the small addition of N$_2$ yields a more stable readout operation. The whole mixture was fine-tuned to keep multiple coulomb scattering to a minimum while keeping good diffusion and high positive ions mobility abilities. However, it needs to be kept at low temperatures (0.1 K [43]) in order to avoid temperature dependence of the mixture.

As mentioned, the main task of the TPC is particle identification. Its performance is shown in Figure 5.4. The resolution of measured energy loss (that can be seen in Figure 5.4) needs to be very good even in high multiplicities that are measured in Pb-Pb collision. With this precision, the TPC allows for even-by-event studies of fluctuations in hadronic observables and provides information about the composition of the dense medium created in a collision.



ALI-PUB-26808
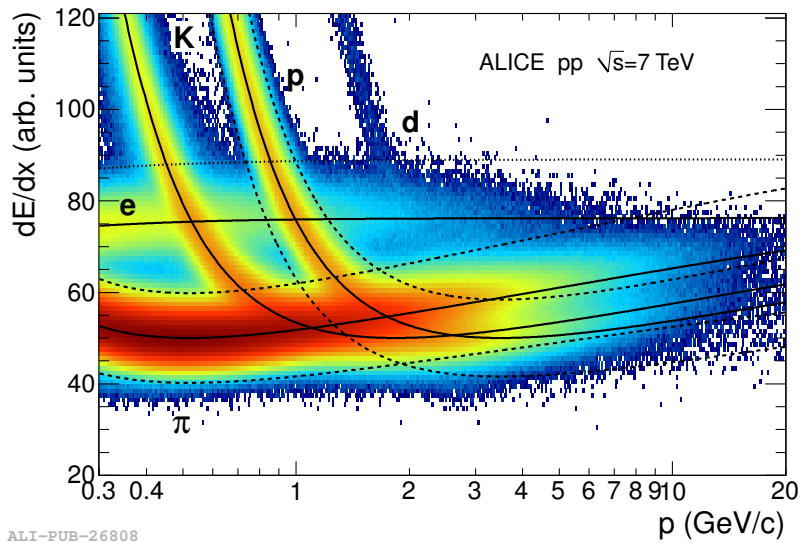
**Figure 5.4:** Specific energy loss in the TPC as a function of momentum with superimposed Bethe-Bloch lines for various particle species [44].

### 5.2.3 Time-of-Flight

Another crucial detector for particle identification is the Time-of-Flight detector (TOF), especially for even-by-event identification of pions, kaons and protons in the intermediate momentum range for high multiplicities that are observed in Pb-Pb interactions. Similarly to TPC or ITS, it covers pseudorapidity region $|\eta| \leq 0.9$ [39]. Due to the large areas, that the TOF needs to cover (length of 741 cm and internal and external radii 370 cm and 399 cm, respectively [39]), gaseous Multigap Resistive Plate Chambers (MRPC's) were used. MRPCs are known for their good

time resolution that has a great influence on TOF particle identification at high momenta.

The TOF has a cylindrical geometry and it surrounds the Transition Radiation Detector (TRD) and TPC. The measurement of time is triggered by the T0 detector which has two sets of Cherenkov detectors at each side of the interaction point (T0A, T0C). The time measurement is connected to tracks going through the TOF. The tracks are extrapolated from the TPC outer wall to the inner radius of TOF. The TRD between TPC and TOF causes multiple scattering of particles and may cause deviation of tracks, for correct tracking, it associates reconstructed tracks to correct TOF signal.

The performance of the TOF can be seen in Figure 5.5. It shows the distribution of $\beta$ velocity on momentum, that is measured by the TPC. The figure shows a good separation of pion, kaon and proton tracks even for high multiplicity measurements. The velocity is obtained from the known time of flight and length of reconstructed tracks. These also provide information about the mass of the particle thanks to known momentum from the TPC.
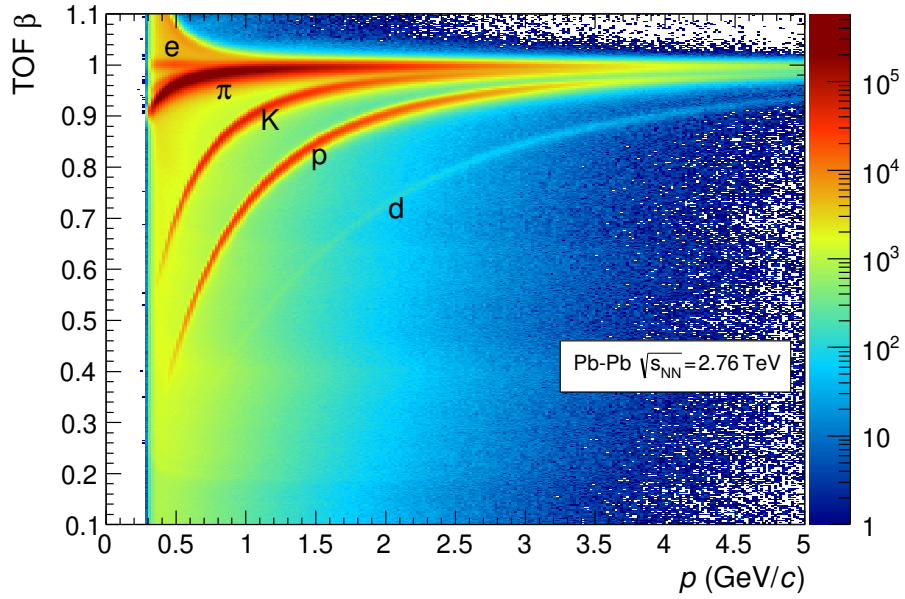


**Figure 5.5:** Distribution of $\beta$ as measured by the TOF detector as a function of momentum for particles reaching the TOF in Pb-Pb interactions [45].

### 5.2.4 Detectors for Data Selection and Triggers

**V0 Detector**

The V0 detector is a scintillator detector consisting of 2 arrays (V0A, V0C), each mounted on a different side of the interaction point on the beampipe. One of the disks is shown on the left-hand side of Figure 5.6. The arrays are small angle detectors with pseudorapidity coverage $2.8 < \eta < 5.1$ and $-3.7 < \eta < -1.7$ for V0A and V0C respectively [46]. The signal from scintillators is collected and converted by wavelength shifting fibres (WLS), that send the signal further to photomultiplier

tubes using optical fibres. The WLS can be seen on the left-hand side of Figure 5.6, where one of the sectors of V0 is illuminated by UV light and causes them to glow in blue and green colours.

The V0 detector serves as a minimum-bias trigger for both pp and Pb-Pb collisions and a centrality trigger for Pb-Pb collisions, using the forward multiplicities. The detector measures particles not only from the initial collision but also from secondary interactions with residual gas that is present in the LHC vacuum chamber. The number of primary particles and number of measured hits is monotone, thus, together with recorded multiplicity, providing information about the centrality of the collision.

The V0 decisions can be used for the rejection of beam-gas or fake signals. The beam-gas event is recognized from the beam-beam event by measuring the time of arrival of particles in each V0 array. These will differ in the case of beam-beam and beam-gas interaction. Furthermore, the V0 participates in luminosity measurement both for pp and heavy ion collisions.
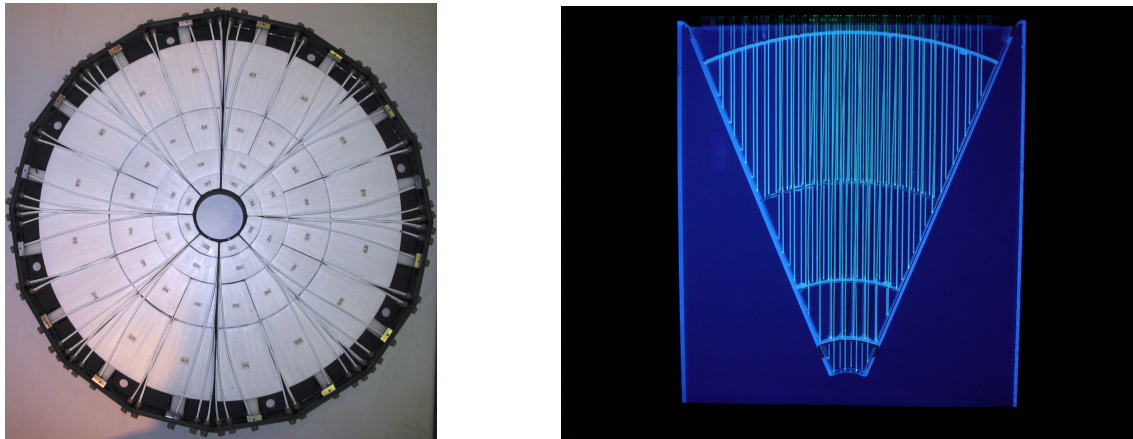


**Figure 5.6:** Left: One of the V0 detector disks [47]. Right: One of the 8 sectors of V0A illuminated with UV light [48].

**AD detector**

The ALICE Diffractive Detector (AD) is, similar to V0, a scintillation detector. It consists of 2 modules, each placed at either side of the interaction point, denoted ADA and ADC, with pseudorapidity coverage of -7.0 $< \eta <$ -4.9 and 4.8 $< \eta <$ 6.3 [49] for ADA and ADC respectively. The AD thus expands the coverage of Minimum Bias Trigger. The design of one of the modules is displayed in Figure. 5.7. The scintillation plastic is divided into 8 modules that are placed around the beampipe in two layers.

The signal from scintillation material is transferred through WLS to optical fibres and PMTs. The readout electronics are the same as those of the V0 detector. Furthermore, the AD provides an extended centrality trigger using its ability to trigger on the deposition of charge. In total, the measured signal of AD is split into two signals, one to measure said deposited charge and the other, similarly to V0, measure

the time of arrival of particles.
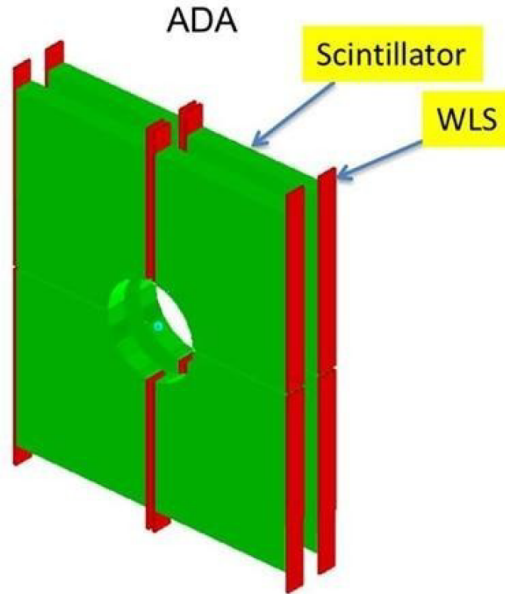


**Figure 5.7:** Design of the ALICE Diffractive Detector (AD) [49].

**Zero-Degree Calorimeter**

The ALICE experiment utilises several types of calorimeters in order to detect the energy of particles and their type. A calorimeter used for data selection in the following analysis is the Zero-Degree Calorimeter (ZDC). The ZDC is placed along the LHC beam axis ($\approx$100 m from IP) where the distance between two beampipes reaches maximum.

After a collision takes place, the particles in the medium can be divided into two groups, spectators and participants. ZDCs measure the energy of spectators, that are created in non-central collisions, thus improving the centrality determination of a collision. The measured energy is expected to decrease with increasing centrality. It consists of a two-piece set of detectors (ZDA, ZDC), one collecting spectator neutrons and the other protons, in positive and negative pseudorapidities, respectively. The spectator nucleons are deflected by the magnets used for beam deflection, which poses a limitation on ZDC's position along the beampipe and constrains its dimensions.

The detection is based on a combination of passive and active material. The passive absorber has to be dense due to limited dimensions and it is used for particle shower generation which further creates Cherenkov radiation in quartz fibres, that act as an active material. These are fully sensitive to electromagnetic showers, unfortunately, they are less sensitive to low energy pions.

## 5.2.5  Forward Muon Spectrometer

The Forward Muon Spectrometer is a crucial detector for heavy quarkonia measurements. Its ability to measure with an invariant mass resolution of 100 MeV/$c^2$ [39] allows precise measurements even of $\Upsilon$ meson. The measurements of muons are vital for quarkonia $\mu^+\mu^-$ decay channel. A great advantage of the muon spectrometer is the ability to make a comparison of several quarkonia species using their simultaneous measurement.

The detector consists of several parts, the first one is a passive absorber placed in L3 solenoid. This section absorbs hadrons and photons coming from the interaction. In order to reduce multiple scattering effects, the absorber was made mostly from carbon and concrete. The absorber is followed by a tracking system and a large dipole magnet placed outside the solenoid. The last part is a passive muon filter wall and trigger chambers.

## 5.2.6  Trigger System

The ALICE trigger system is a key system for data readout. The system provides event selection for specific event readout and also for limited bandwidth of data acquisition. It also enhances the detector cooperation as each detector works with different dead times, it appears as busy for different time intervals. The performance of detectors is different for different multiplicities, that are affected by colliding particles. The selection criteria are thus defined by running modes: heavy ion, pA, pp.

The trigger system has 3 levels. The first one (Level 0, L0) is a fast trigger, the first one to reach the detector (1.2 $\mu$m, [39]). It is accompanied by a Level 1 (L1) trigger level arriving later (6.5 $\mu$m, [39]) with additional trigger inputs not picked up by L0. The third is Level 2 (L2) which verifies the acceptance of an event following a past-future protection interval (88 $\mu$m, [39]).

The past-future protection interval is applied due to large multiplicities resulting in a pile-up of events in the detector. The pile-up could spoil recorded events and these should be rejected. The rejection is done using event classification based on centrality (peripheral and semi-central) with different criteria in each class.

Trigger decisions are logically denoted as asserted, negated and not relevant and are further coupled by ANDs into 50 trigger classes. These classes are defined keeping in mind the detector requirements, past-future protection requirements and possible scaling factors. These scaling factors affect the amount of readout data by, for example, choosing every $n$-th event to keep.

## 5.2.7  Data Flow in ALICE

After receiving trigger information from Central Trigger Processor (CTP), the measured signals from detectors are sent to the Detector Data Links (DDL). The DDl is an interface connecting the detector front-end electronics and the Data AcQuisition

system (DAQ). The data is further processed and transmitted using optical fibres in computing centres. The data is further processed both online and offline.

The online processing is managed by High-Level Trigger (HLT) which can be categorized into several processing layers. The first layer is the acquirement of raw data from detectors. The following layer is dedicated to the basic calibration and extraction of clusters and hits. The first two layers are ongoing simultaneously. The next step is data reconstruction followed by event reconstruction using both processed and calibrated inputs. The last layer is focused on event selection for given physics regions. Data is further sent to algorithms for compression to reduce the amount of data.

More time-challenging tasks of data processing are handled offline. These tasks include for example detector response simulations, alignment, data visualization or analysis. The offline tasks are aimed to result at interpreting data and required physics content.

Similarly to online computing, offline computing can be also divided into several categories. The first is distributed computing. This part utilizes the distribution of data processing into multiple computing servers that are situated worldwide. This distribution is enabled using Grid Middleware providing services such as authentication or data management and its set is called AliEn. The second category is offline data processing using the AliRoot framework. AliRoot is an ALICE offline framework using Object-Oriented techniques for programming in C++ and it is complimented the AliEn for gaining access to the computing grid. AliRoot provides tools for Monte Carlo simulations, detector alignments, data reconstruction and visualization and analysis. Furthermore, it enables the simulation of detector response or event simulation for determining the detector performance.

# Chapter 6

# Analysis of Monte Carlo Data

The Monte Carlo (MC) data sample was generated for comparison of the measured sample with an ideal case. The events were generated using the AliRoot framework and the EvtGen generator.

The AliRoot framework is built on the ROOT system and is used for data reconstruction, analysis or MC data simulation. The simulation is carried out by various types of event generators such as Pythia [50] or Herwig [51]. Each generated event carries information about a created particle (mother particle) and its vertex. Generated particles are further propagated through a set of detectors inside the experiment and generate a response inside the detector, hits. After considering the response of the detector, hits are converted to digits. The created digits are then used for reconstruction and analysis. For detailed information about the ALICE analysis framework see [52].

The EvtGen generator [53] is an MC generator for simulations of particle decays incorporating models for decays of $B$ mesons and other vector, scalar or tensor resonances, e.g. J/$\psi$. Apart from the possibility of simulating a decay of a particle, it allows adding the option of accounting for the possible radiation in the final state. This is implemented using the PHOTOS [54] algorithm for QED radiation.

Simulated events in the following analysis are used for studying of decay of vector meson J/$\psi$ to leptons $\mu$ with radiation of photons in the final state. The decay is simulated with the VLL algorithm. This algorithm uses an amplitude $A = \varepsilon^\mu L_\mu$ where $\varepsilon$ denotes a polarization vector of the mother particle allowing the used set a preferred polarization.

For the purposes of this thesis the events were generated for Pb-Pb collisions with energy $s_{\sqrt{NN}} = 5.02$ TeV with 100 000 events for both coherent or incoherent production with three possible polarizations of J/$\psi$, e.i. transversal, longitudinal or no polarization.

## 6.1   Quantum Tomography Procedure

The quantum tomography procedure begins with the determination of the angular distribution of the generated sample in the CS frame. The angular distribution

is described by a distribution in $\cos\theta, \phi$ coordinates. These are inferred from the $\hat{ell}_J$ vector $\hat{\ell}_J = (\sin\theta\cos\phi, \sin\theta\sin\phi, \cos\theta)$ calculated by a procedure described in Chapter 3. The two-dimensional distribution is further fitted with angular distribution prescription (3.22) in order to determine the full density matrix of the J/$\psi$ state. The fit was performed on an unbinned dataset using the MLM fit for parameter estimation.

Even though there are 9 parameters $m_i$ in the Cholesky decomposition, there are only 8 parameters in the (3.22) function, $m_1$ is missing. In order to complete the density matrix, the $m_1$ parameter is given from the normalisation of density matrix $1 = m_1^2 + m_2^2 + ... + m_9^2$. The density matrices together with visualization of the two-dimensional distribution and its projections onto the $\phi$ and $\cos\theta$ axes together with fit function.

For the purposes of verification of quantum tomography procedure for polarization determination, the fit of simplified distribution 3.23 together with the determination of polarization parameters. The choice of 3.23 to infer the polarization state comes from the fact, that it can be directly compared to 2.6 term-by-term to yield parameters $\lambda_\theta, \lambda_\phi, \lambda_{\theta\phi}$.

### 6.1.1 Coherent Photoproduction

The two-dimensional dimuon distributions are shown in Figure 6.1. The top figure shows the shape of a distribution coming from transversely polarized J/$\psi$, middle longitudinally polarized. It is clear and expected, that transverse and longitudinal polarization show opposite shapes to each other, whereas the unpolarized case shows no specific shape.

The two-dimensional distribution was fitted with (3.22) with projections shown in Figure 6.3. Each fit shows reasonable $\chi^2/ndf$ values with rather good results of fits. Figure (a) once again refers to transversely polarized J/$\psi$, (b) longitudinally and (c) unpolarized. These fits allowed the determination of density matrices for each state, matrix (6.1) for transverse polarization, (6.2) for longitudinal and (6.3) for no polarization. These density matrices can be further used for the study of properties of the J/$\psi$ state.

$$\rho_{fit}^{trans} = \begin{pmatrix} 0.011944 & -0.00603284 - i0.0028999 & -0.0044235 + i0.0053469 \\ -0.00603284 + i0.0028999 & 0.49539 & -0.00022768 + i0.007488 \\ -0.0044235 - i0.0053469 & -0.00022768 - i0.007488 & 0.49267 \end{pmatrix}, \quad (6.1)$$

$$\rho_{fit}^{long} = \begin{pmatrix} 0.97006 & 0.006287 - i0.0017765 & 0.0063804 + i0.013923 \\ 0.006287 + i0.0017765 & 0.015679 & -0.0052653 + i0.0038775 \\ 0.0063804 - i0.013923 & -0.0052653 - i0.0038775 & 0.014262 \end{pmatrix}, \quad (6.2)$$

$$\rho_{fit}^{unpol} = \begin{pmatrix} 0.33116 & 0.0050805 - i0.014932 & -0.0020985 - i0.00057901 \\ 0.0050805 + i0.014932 & 0.34554 & -0.0014467 + i0.0044864 \\ -0.0020985 + i0.00057901 & -0.0014467 - i0.0044864 & 0.3233 \end{pmatrix}. \quad (6.3)$$
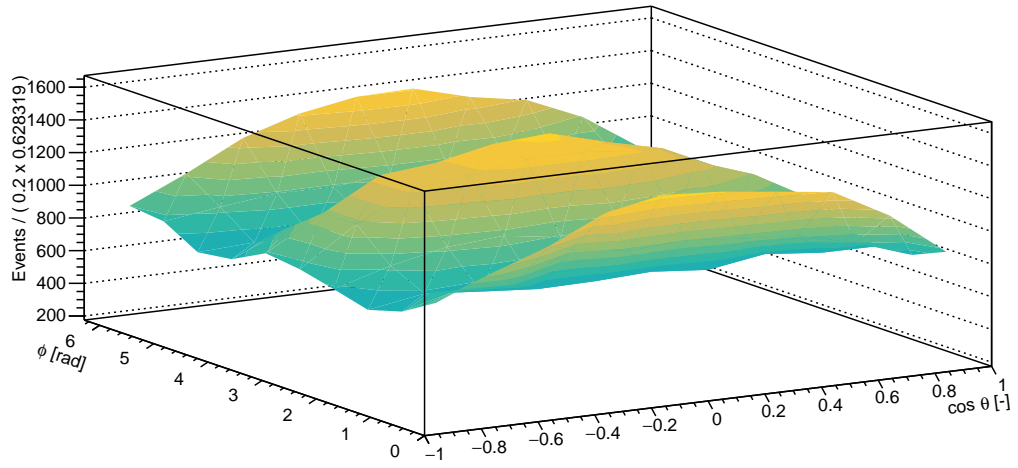
**(a)**
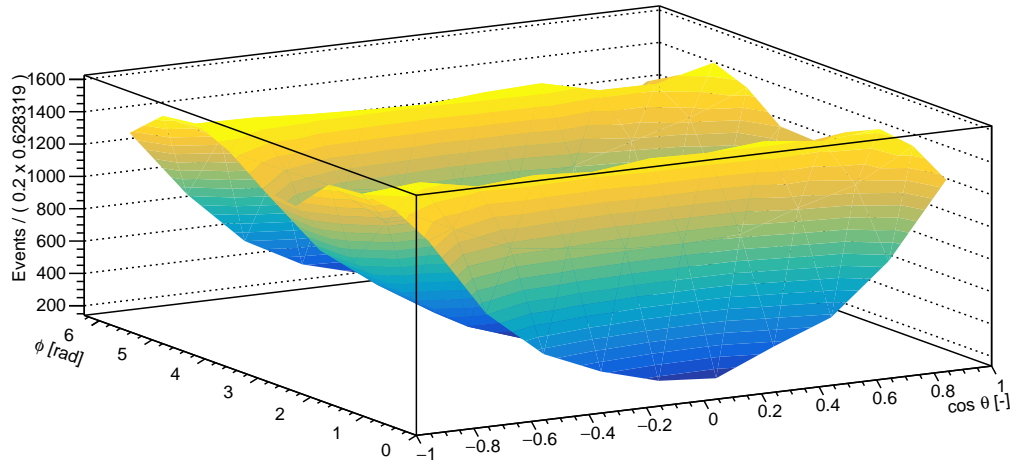


**(b)**
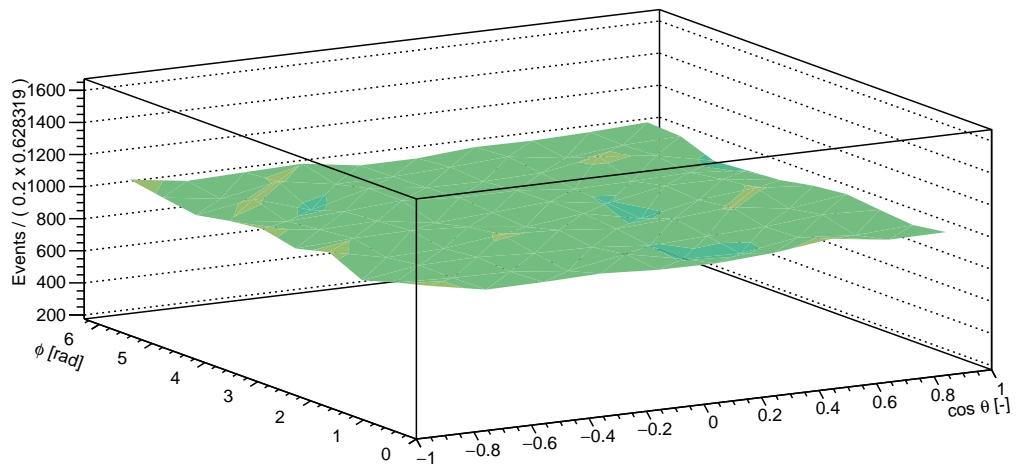


**(c)**

**Figure 6.1:** Two-dimensional $(\cos\theta, \phi)$ distributions of the final state muon pairs from the decay of coherently produced J/$\psi$ polarized transversely (a), longitudinally (b) and unpolarized (c).
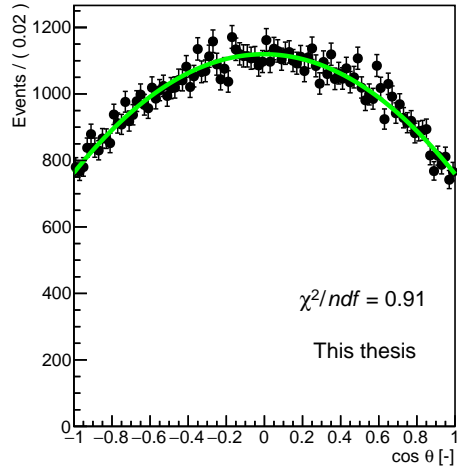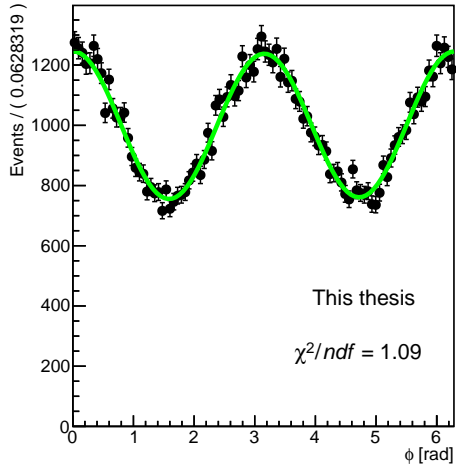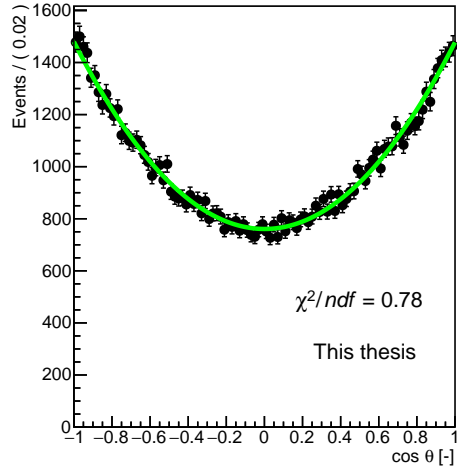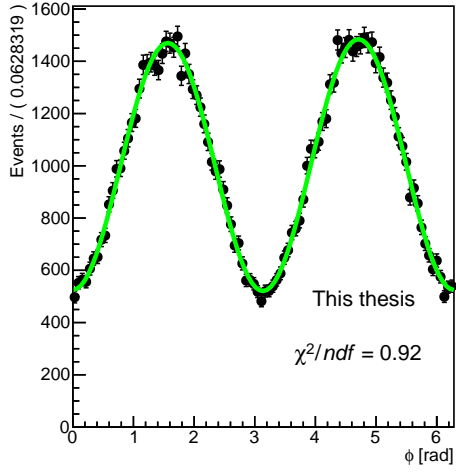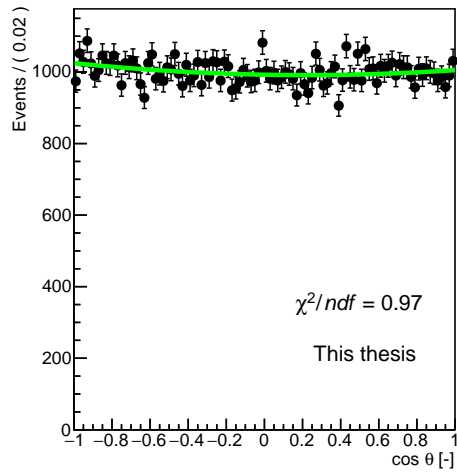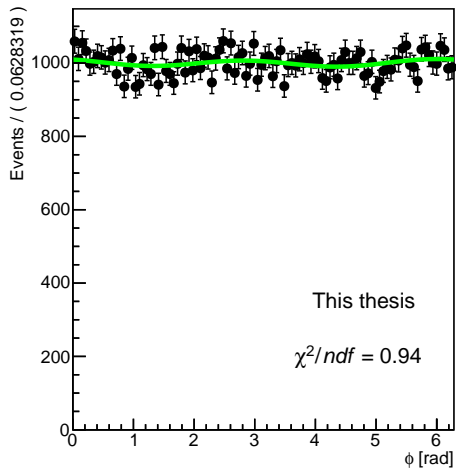
**Figure 6.2:** Projection of two-dimensional final state distribution from the decay of coherent J/$\psi$ that is (a) transversely or (b) longitudinally polarized or (c) unpolarized into $\phi$ axis (left) and $\cos\theta$ (right) axis together with the fitted function (3.22).
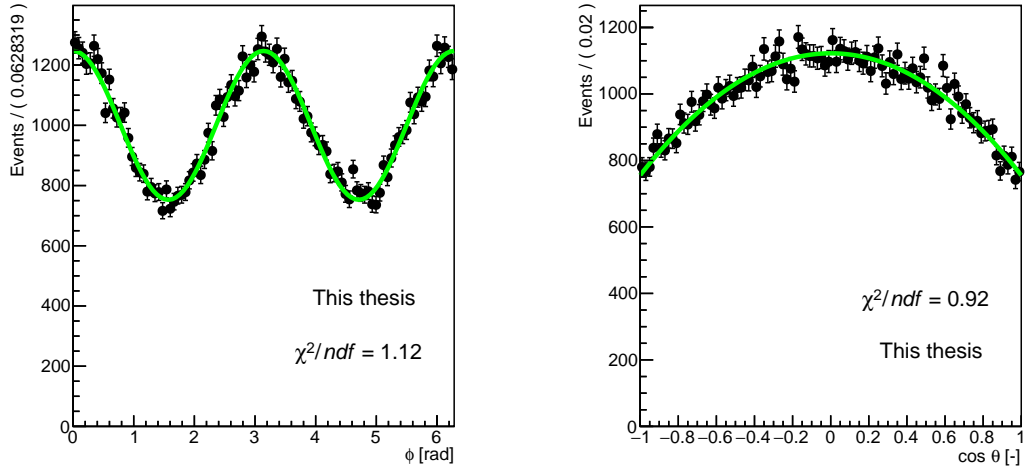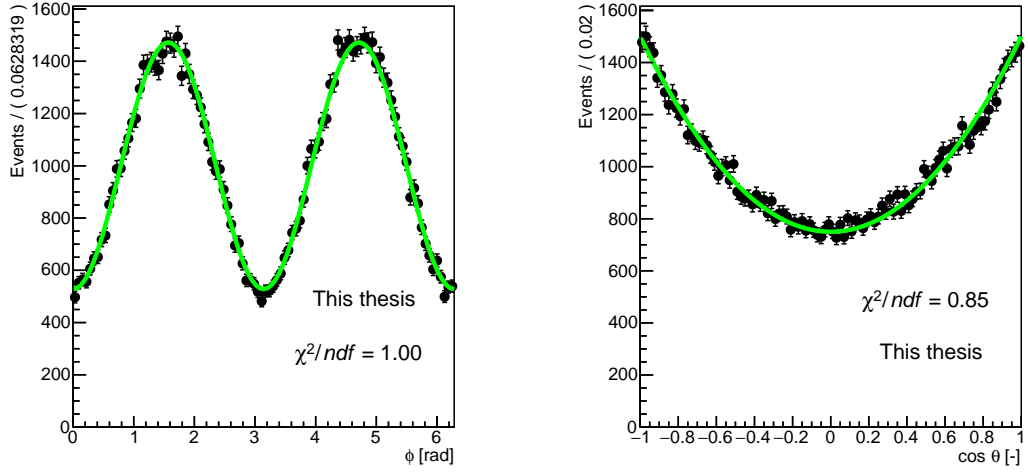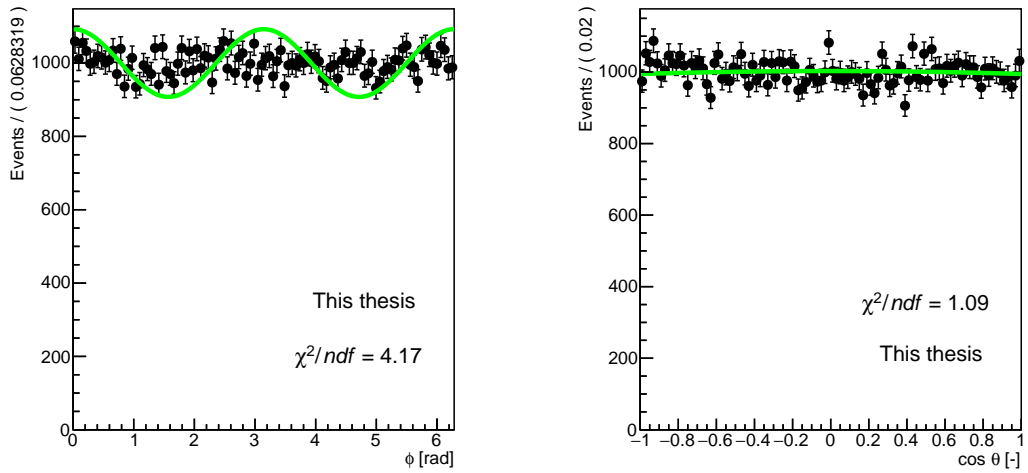
**Figure 6.3:** Projection of two-dimensional final state distribution from the decay of coherent J/$\psi$ that is (a) transversely or (b) longitudinally polarized or (c) unpolarized into $\phi$ axis (left) and $\cos\theta$ (right) axis together with the fitted function (3.23).

The fits for determination of $\lambda_\theta, \lambda_\phi, \lambda_{\theta\phi}$ and $\tilde{\lambda}$. The first three parameters are expected to be frame-dependent, however, the $\tilde{\lambda}$ is frame independent, calculated as (6.4). We expect that for longitudinal polarization the calculation yields $\tilde{\lambda} = -1$, for transversal $\tilde{\lambda} = 1$. The values of $\lambda_\theta, \lambda_\phi, \lambda_{\theta\phi}$ are taken from the reduced density matrix, considering the parity conservation, as in equation (3.27).

$$\tilde{\lambda} = \frac{\lambda_\vartheta + 3\lambda_\varphi}{1 - \lambda_\varphi} \, . \tag{6.4}$$

The fit of distribution (3.23) shows similar goodness-of-fit as in the fit of full distribution for longitudinal and transverse, whereas for the unpolarized the goodness-of-fit in $\phi$ has decreased. This is further propagated into $\tilde{\lambda}$ value.

The overall results are listed in Table 6.1. The longitudinal and transverse polarization display expected results, whereas the unpolarized case is highly affected by the quality of fit.

| Transverse | | Longitudinal | | Unpolarized | |
|---|---|---|---|---|---|
| $\lambda_\theta$ | -0.3269 | $\lambda_\theta$ | 0.9998 | $\lambda_\theta$ | -0.0083 |
| $\lambda_\phi$ | 0.3304 | $\lambda_\phi$ | -0.9429 | $\lambda_\phi$ | 0.1382 |
| $\lambda_{\theta\phi}$ | -0.0638 | $\lambda_{\theta\phi}$ | -0.0131 | $\lambda_{\theta\phi}$ | -0.4246 |
| $\tilde{\lambda}$ | 0.9922 | $\tilde{\lambda}$ | -0.9424 | $\tilde{\lambda}$ | 0.4716 |

**Table 6.1:** Polarization parameters $\lambda_\theta, \lambda_\phi, \lambda_{\theta\phi}$ and $\tilde{\lambda}$ calculated from fit parameters as in (3.27) with frame invariant parameter $\tilde{\lambda}$ for coherent J/$\psi$.

## 6.1.2   Incoherent Production

Similarly to the coherent case, the two-dimensional dimuon distributions are shown in Figure 6.4. The top figure shows the shape of a distribution coming from transversely polarized J/$\psi$, middle longitudinally polarized. Together with the unpolarized case in the bottom figure the incoherently produced J/$\psi$ shows no significant deviation from the coherent production, thus similar results are expected.

The two-dimensional distribution was again fitted with (3.22) with projections shown in Figure 6.3. Each fit shows reasonable $\chi^2/ndf$ values with rather good results of fits. Figure (a) once again refers to transversely polarized J/$\psi$, (b) longitudinally and (c) unpolarized all for incoherent production. These fits allowed the determination of density matrices for each state, matrix (6.5) for transverse polarization, (6.6) for longitudinal and (6.7) for no polarization. These density matrices can be further used for the study of properties of the J/$\psi$ state. Even though there are slight differences in the density matrices, they are again distinguishable for different polarization states.

$$\rho_{fit}^{trans} = \begin{pmatrix} 0.045539 & 0.0016594 - i0.00035997 & 0.0024985 + i0.0038046 \\ 0.0016594 + i0.00035997 & 0.50005 & 0.0034643 + i0.0098857 \\ 0.0024985 - i0.0038046 & 0.0034643 - i0.0098857 & 0.45441 \end{pmatrix}, \quad (6.5)$$

$$\rho_{fit}^{long} = \begin{pmatrix} 0.8939 & 0.0017197 + i0.0040953 & 0.0050063 - i0.0029578 \\ 0.0017197 - i0.0040953 & 0.016984 & 0.0034953 - i0.00030982 \\ 0.0050063 + i0.0029578 & 0.0034953 + i0.00030982 & 0.089118 \end{pmatrix}, \quad (6.6)$$

$$\rho_{fit}^{unpol} = \begin{pmatrix} 0.33762 & -0.0018794 - i0.018923 & 0.00054111 + i0.0015243 \\ -0.0018794 + i0.018923 & 0.33894 & -0.0058301 + i0.0049973 \\ 0.00054111 - i0.0015243 & -0.0058301 - i0.0049973 & 0.32344 \end{pmatrix}. \quad (6.7)$$

The fits for determination of $\lambda_\theta, \lambda_\phi, \lambda_{\theta\phi}$ and $\tilde{\lambda}$. The polarization parameters are calculated using the same procedure as in the coherent production with similar expectations for results.

The fit of distribution (3.23) shows similar goodness-of-fit as in the fit of full distribution for transverse polarization, whereas for the unpolarized the goodness-of-fit in $\phi$ has decreased. These are comparable to the coherent case. However, in the incoherent polarization, there is a decrease in goodness-of-fit for longitudinal polarization affecting the results of $\lambda$ parameters. This is further propagated into $\tilde{\lambda}$ value.

The overall results are listed in Table 6.2. The transverse polarization display expected results, whereas the unpolarized and longitudinal case is affected by the quality of fit.

For further analysis and comparison of data see 7.

| Transverse | | Longitudinal | | Unpolarized | |
|---|---|---|---|---|---|
| $\lambda_\theta$ | -0.2642 | $\lambda_\theta$ | 0.9998 | $\lambda_\theta$ | -0.0067 |
| $\lambda_\phi$ | 0.3274 | $\lambda_\phi$ | -0.8253 | $\lambda_\phi$ | 0.1300 |
| $\lambda_{\theta\phi}$ | -0.1601 | $\lambda_{\theta\phi}$ | -0.0120 | $\lambda_{\theta\phi}$ | -0.4296 |
| $\tilde{\lambda}$ | 1.0672 | $\tilde{\lambda}$ | -0.8087 | $\tilde{\lambda}$ | 0.4408 |

**Table 6.2:** Polarization parameters $\lambda_\theta, \lambda_\phi, \lambda_{\theta\phi}$ and $\tilde{\lambda}$ calculated from fit parameters as in (3.27) with frame invariant parameter $\tilde{\lambda}$ for coherent $J/\psi$.
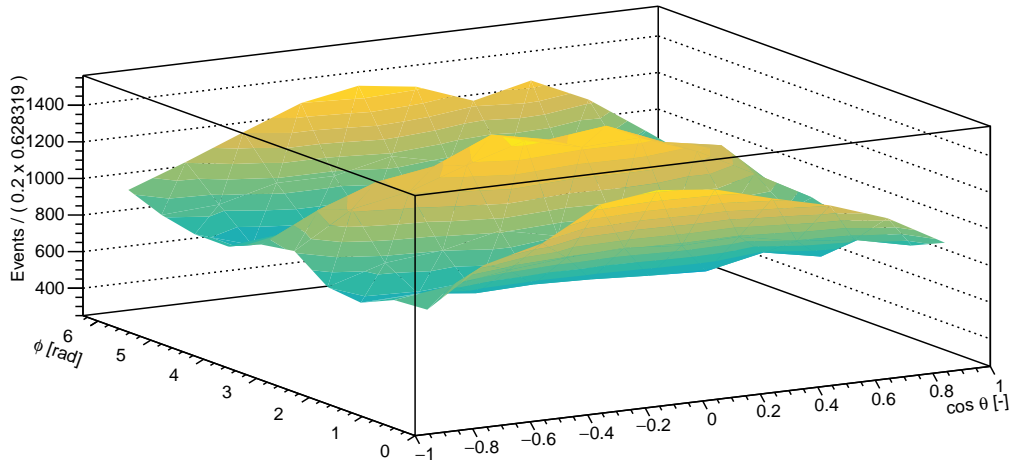
**(a)**
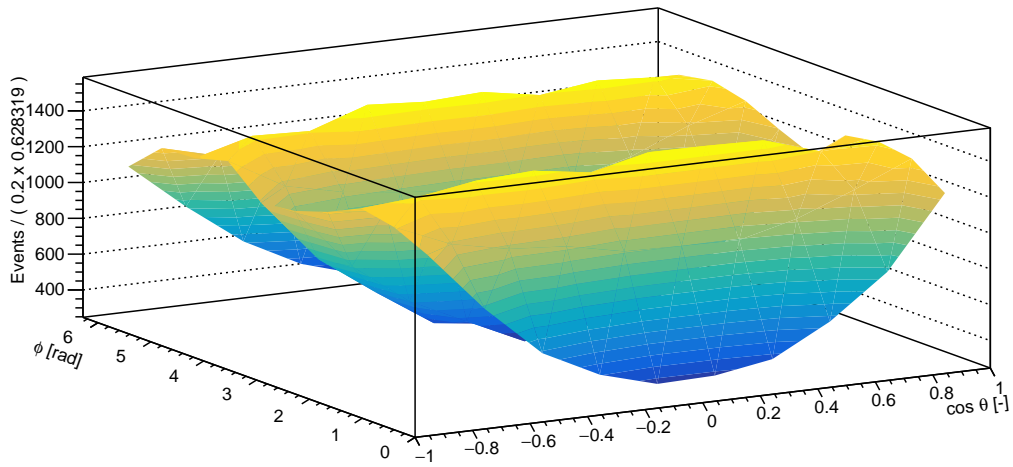


**(b)**
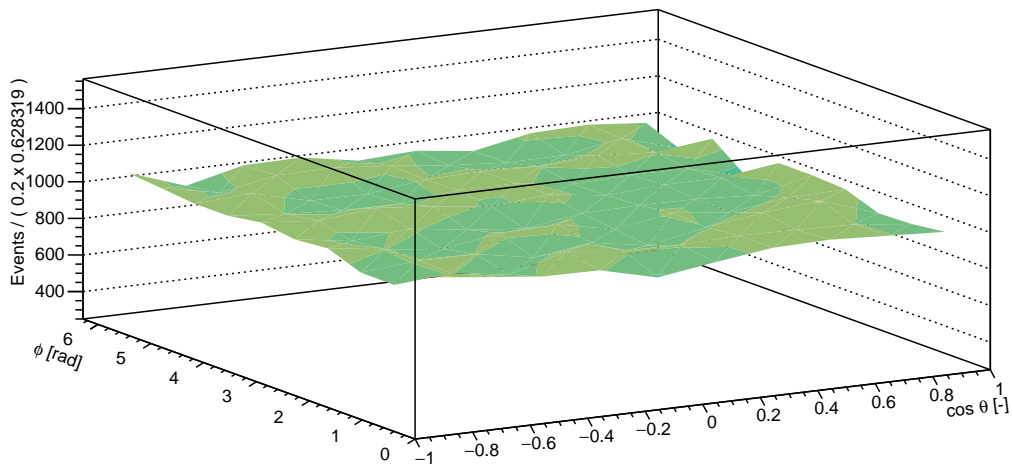


**(c)**

**Figure 6.4:** Two-dimensional $(\cos\theta, \phi)$ distribution of the final state muon pairs from the decay of incoherently produced J/$\psi$ polarized transversely (a), longitudinally (b) and unpolarized (c).
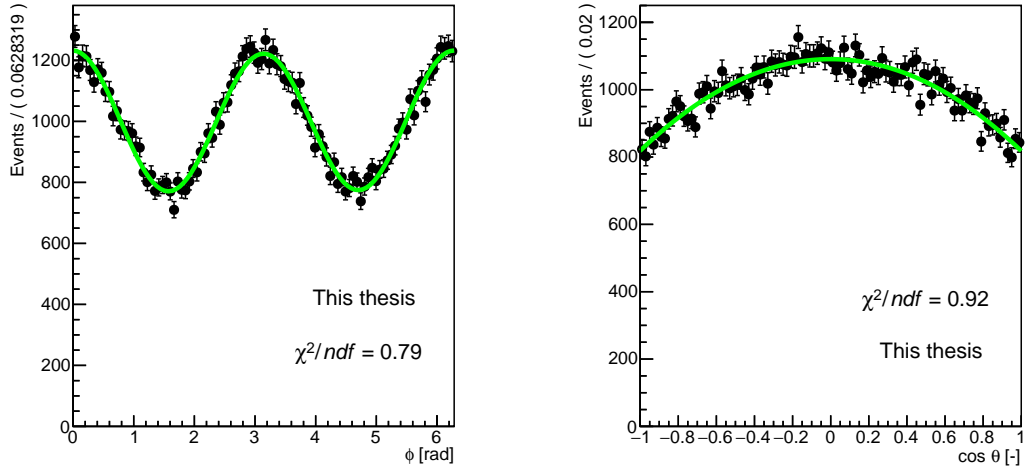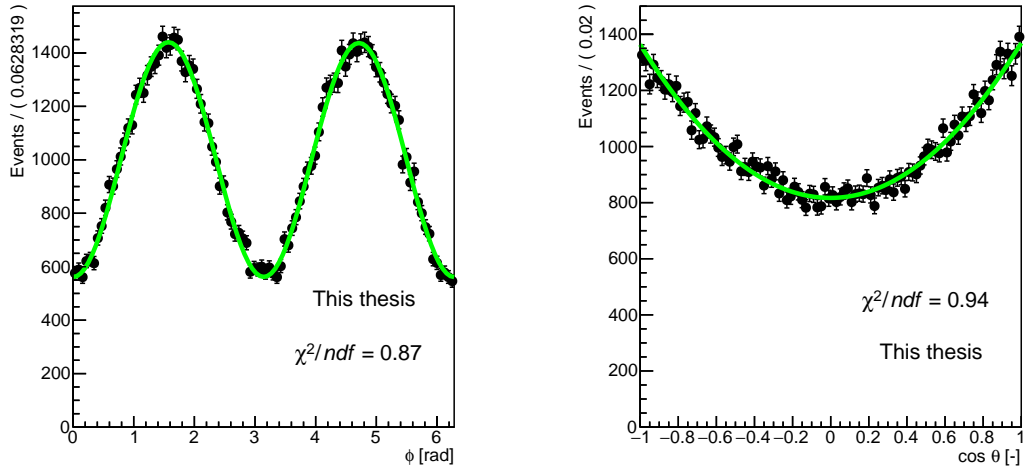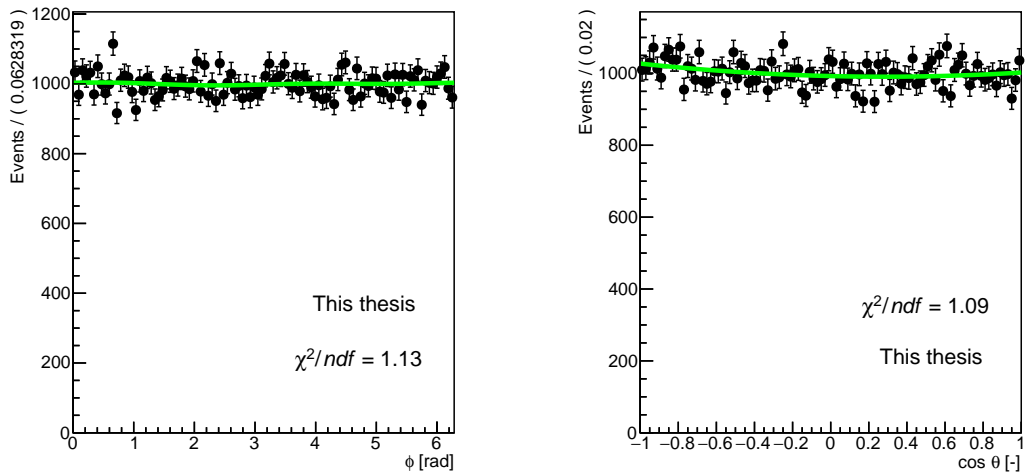
**Figure 6.5:** Projection of two-dimensional final state distribution from the decay of incoherent $J/\psi$ that is (a) transversely or (b) longitudinally polarized or (c) unpolarized into $\phi$ axis (left) and $\cos\theta$ (right) distribution together with the fitted function (3.22).
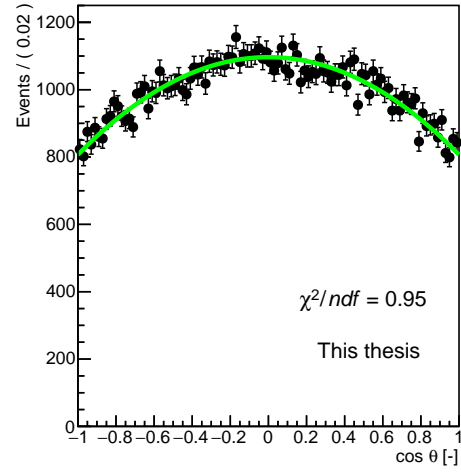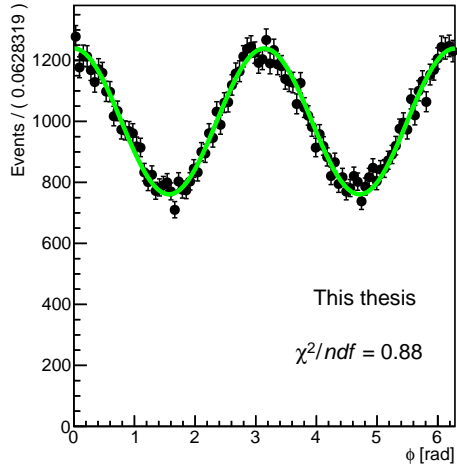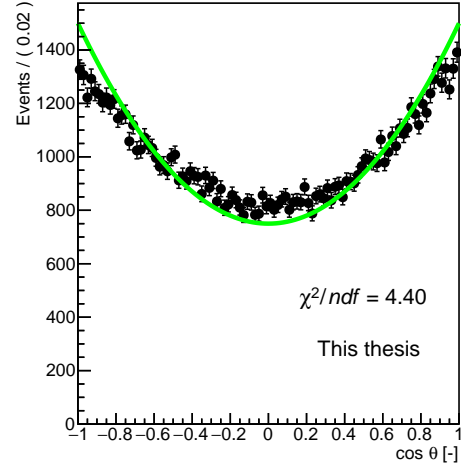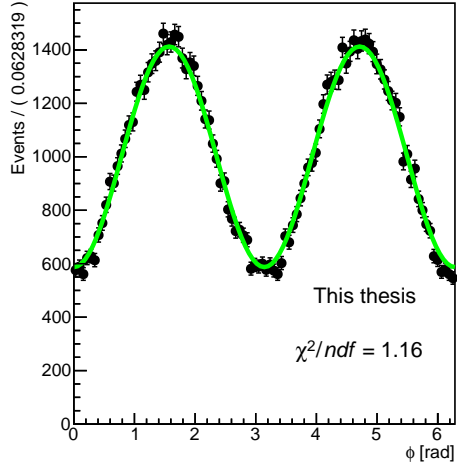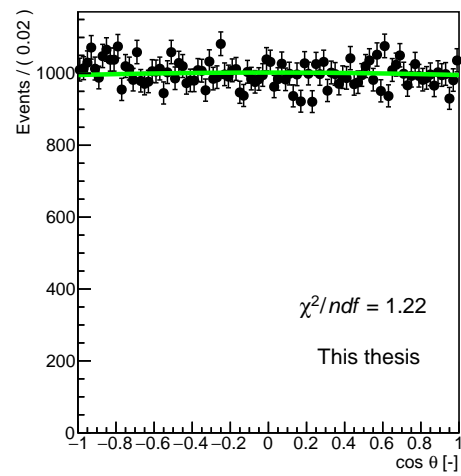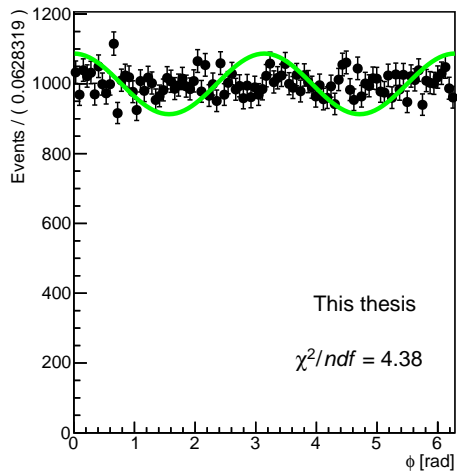
**Figure 6.6:** Projection of two-dimensional final state distribution from the decay of incoherent J/$\psi$ that is (a) transversely or (b) longitudinally polarized or (c) unpolarized into $\phi$ axis (left) and $\cos\theta$ (right) distribution together with the fitted function (3.23).

# Chapter 7

# Analysis of Measured Data

The analysis of polarization of both coherent and incoherent $J/\psi$ is performed on the data sample measured in the 2018 data taking measured by the ALICE collaboration at the LHC collider. Considered events were measured during the Pb-Pb run, at midrapidity with centre-of-mass energy $\sqrt{s_{NN}} = 5.02$ TeV. The sample for this analysis was merged from two periods LHC2018q and LHC2018r corresponding to two different polarities of the solenoid magnet, positive and negative respectively.

## 7.1   UPC Triggers in 2018

Triggers are used for the selection of events and are necessary for the filtration of data. This is crucial for correctly acquiring the data with respect to the desired properties and limitations of detectors and readout. Triggers are usually built from several logical inputs from several detectors.

In order to choose only UPC events, the analysed data were triggered with CCUP31 UPC trigger in the central barrel. In order to account for the possible need for past-future protection, the trigger CCUP31-B-SPD2-CENTNOTRD was used from run number 295881. Run numbers up to 295880 did not require this protection and CCUP31-B-NOPF-CENTNOTRD was used. The difference is denoted by SPD2 for past-future protection and NOPF for no past-future protection. These triggers are defined by combining simple detector outputs, i.e.

- 0VBA (0VBC) = signal in the V0A (V0C) detector in a beam-beam window,

- 0UBA (0UBC) = signal in the ADA (ADC) detector in a beam-beam window,

- 0STG = topological trigger of the SPD detector with optional opening angle,

- 0OMU = trigger to choose only events with between 2 and 6 hits in the TOF detector.

There are more trigger elements that are required for the muon spectrometer or control triggers, but these are not required for this analysis. The 0STG trigger has been set to 36 degrees from the beginning of 2018 data taking and it was changed

from run 295753 to 144 degrees. The CCUP31-B-NOPF-CENTNOTRD is defined as !0VBA !0VBC !0UBA !0UBC 0STG 0OMU.

## 7.2   Event Selection

The primary selection of events lies in choosing only events with two good central tracks. The quality of tracks is determined by criteria set by the TPC and the SPD detectors. The TPC detector has 159 points in total. The criterion to choose two good tracks is called TestFilterBit($1\ll5$) requiring each track to have at least 70 TPC points and $\chi^2/ndf$ of the Kalman fit better than 4. The Kalman fit is a procedure widely used in detector physics for the fitting of tracks. The SPD requires at least clusters from each track in the two innermost layers. These criteria are denoted as HasPointOnITSLayer(0) && HasPointOnITSLayer(1).

The secondary selection of events is applied to yield only UPC events at midrapidity around the mass of J/$\psi$, which is decaying into muons with opposite charges. The list of applied cuts is listed below:

Sel1  CCUP31 trigger (for run number below 295881 CCUP31-B-NOPF-CENTNOTRD, for higher run numbers CCUP31-B-SPD2-CENTNOTRD),

Sel2  invariant mass of the dilepton pair is between 2.2 and 4.5 GeV/$c^2$,

Sel3  AD offline veto (requiring empty ADA and ADC detectors) for suppression of hadronic events,

Sel4  V0 offline veto (requiring empty V0A and V0C detectors) for suppression of hadronic events (like in AD),

Sel5  rapidity of dilepton is |y| < 0.8 (to exclude potential border effects,

Sel6  both tracks have pseudorapidity $|\eta|$ < 0.8 for limited area of the cylindrical detector,

Sel7  the tracks have opposite charges,

Sel8  cut on transverse momentum to choose coherent (or incoherent) events is $p_T$ < 0.2 GeV ($p_T$ > 0.2 GeV),

Sel9  criterion to choose only dimuon pairs $\sigma^2_{\mu,1} + \sigma^2_{\mu,2} < \sigma^2_{e,1} + \sigma^2_{e,1}$, where $\sigma^2_{\mu(e),1}$ is the distance between the energy loss expected and measured for lepton tracks,

Sel10  matching hits in the SPD detector.

The list of all criteria with a number of remaining events after each cut is displayed in 7.1 both for coherent and incoherent dimuon events.

| Selection | Number of events |
|---|---|
| CCUP31 trigger | 2134187 |
| Invariant mass in the interval of (2.2; 4.5) GeV/$c^2$ | 55878 |
| ADA offline veto | 55680 |
| ADC offline veto | 55535 |
| V0A offline veto | 48170 |
| V0C offline veto | 43553 |
| Dilepton rapidity $y < |0.8|$ | 42944 |
| Track pseudorapidity $\eta < |0.9|$ | 41270 |
| Tracks have opposite charges | 37055 |
| Dimuon pairs only | 23866 |
| Transverse momentum cut $p_t < 0.2$ GeV/$c$ ($p_t > 0.2$ GeV/$c$) | 15174 (8692) |
| Matching SPD | 13730 (5513) |
| Invariant mass in the interval of (3.0; 3.2) GeV/$c^2$ | 4397 (993) |

**Table 7.1:** Table listing the number of remaining events passing the criteria Sel1 - Sel10 mentioned above. Values in brackets refer to the number of remaining events for incoherent production.

## 7.3 Data Corrections

### 7.3.1 Acceptance

To infer the acceptance and later acceptance and efficiency corrections for the study of J/$\psi$, it is necessary to study the MC reconstructed and simulated data. These were generated by STARLIGHT. The analysis of corrections is provided both for coherent and incoherent samples.

The first step was the determination of acceptance of the detector. This can be determined by studying the fraction of generated events in the pseudorapidity region of the central barrel out of all generated events at midrapidity. This fraction is given as

$$Acc = \frac{N_{gen}(\text{Sel5}, \text{Sel6})}{N_{gen}(\text{Sel5})}. \tag{7.1}$$

The resulting acceptances are shown in Figure 7.1. The top left plot displays acceptance in the two-dimensional $(\cos\theta, \phi)$ distribution for coherent photoproduction, bottom left for incoherent. There is a slight decrease in the number of events in the incoherent production, however, both distributions show large holes in the acceptance of the detector. In order to make further analysis effective, together with the choice of binning, the data are rotated in $\phi$ by $0.25\pi$ in order to observe two holes. Shifted distributions are shown in the right panel of Figure 7.1.

### 7.3.2 Choice of Binning

The choice of binning is a crucial step in further analysis. The chosen number of bins in each axis is affected by two factors, that is the number of events that would be in each bin and the resolution of the detector. The resolution is determined
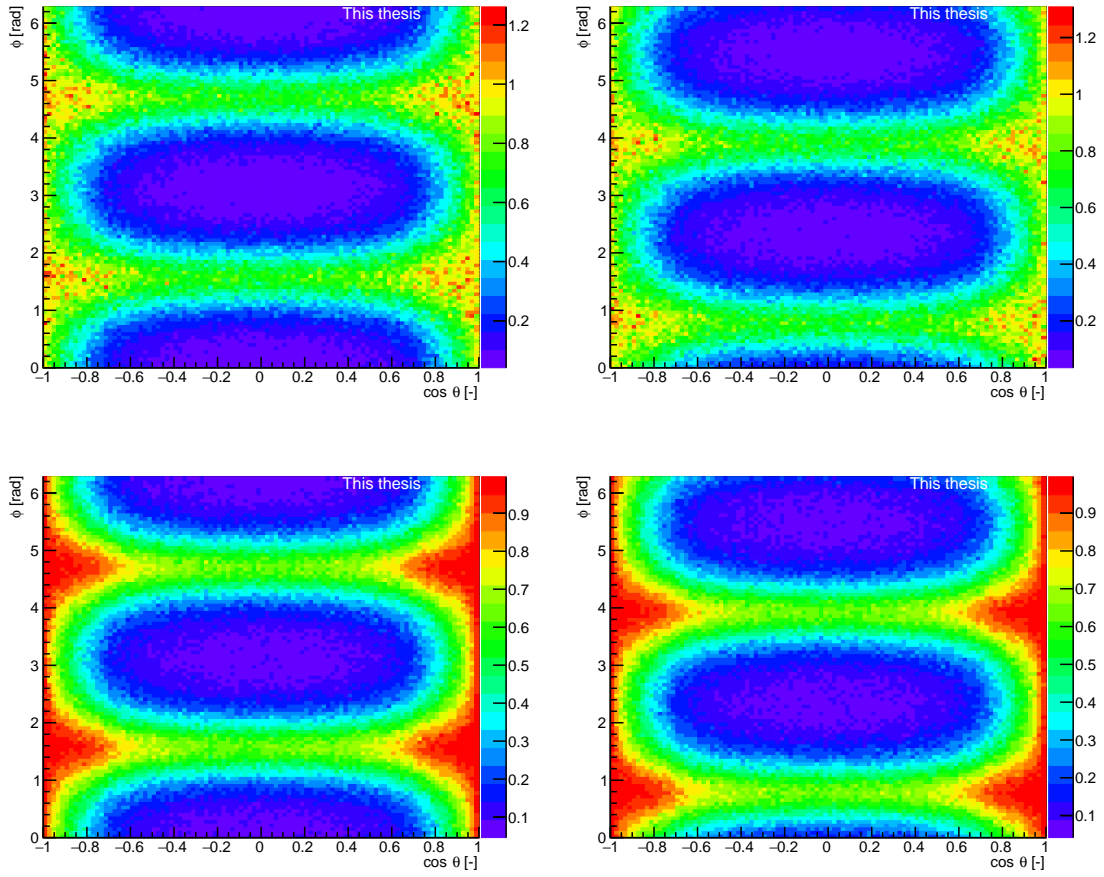
**Figure 7.1:** Two-dimensional $(\cos\theta, \phi)$ distribution of acceptance *Acc* for coherent (top line) and incoherent (bottom line) photoproduction before (left side) and after shift (right side) of $0.25\pi$ in $\phi$ (see text).

by finding a difference between reconstructed and generated events in $\cos\theta$ and $\phi$ distributions. Afterwards, the binning should be chosen based on the resolution that is equal to FWHM of the distribution which is the width of the distribution at half of its magnitude. Resulting plots for resolution determination are shown in Figure 7.2 for coherent photoproduction and Figure 7.3 for incoherent photoproduction. Both types of photoproduction in both distributions show good resolution, the choice of binning is thus not limited by insufficient resolution.
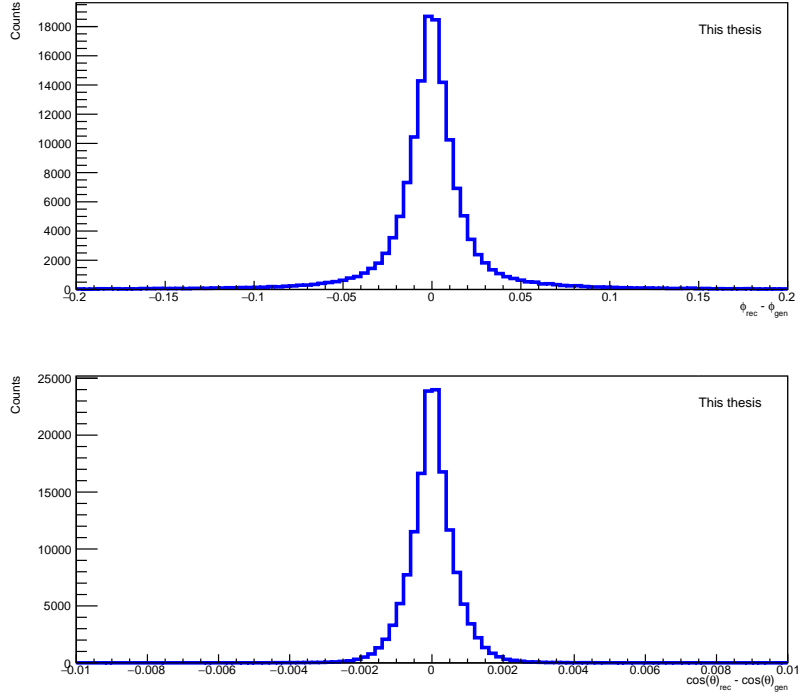


**Figure 7.2:** Resolution in $\phi$ (top) and $\cos\theta$ (bottom) for the coherent photoproduction.

However, binning is significantly influenced by the number of measured events. In order to be able to provide sufficient fits in the mass distribution, there has to be a reasonable amount of events in each bin. The decreased amount of events in incoherent production reduces the number of chosen bins. For coherent production, four bins with equal widths in each distribution were chosen, resulting in sixteen bins in total. For the incoherent productions were chosen four bins in the $\phi$ distribution and three bins in $\cos\theta$ distribution. The reduction in $\cos\theta$ bins is due to preserved shape of the distribution that would be limited for a reduction in bins in $\phi$. Furthermore, bins in the area of decreased acceptance of the detector will be omitted from further analysis. For coherent photoproduction this areas are for $\cos\theta \in (-0.5; 0.5) \cap \phi \in \left(\frac{\pi}{2}; \pi\right)$ and $\cos\theta \in (-0.5; 0.5) \cap \phi \in \left(\frac{3\pi}{2}; 2\pi\right)$. For incoherent the choice is modified due to a different number of bins, thus excluding $\cos\theta \in (-0.33; 0.33) \cap \phi \in \left(\frac{\pi}{2}; \pi\right)$ and $\cos\theta \in (-0.33; 0.33) \cap \phi \in \left(\frac{3\pi}{2}; 2\pi\right)$.
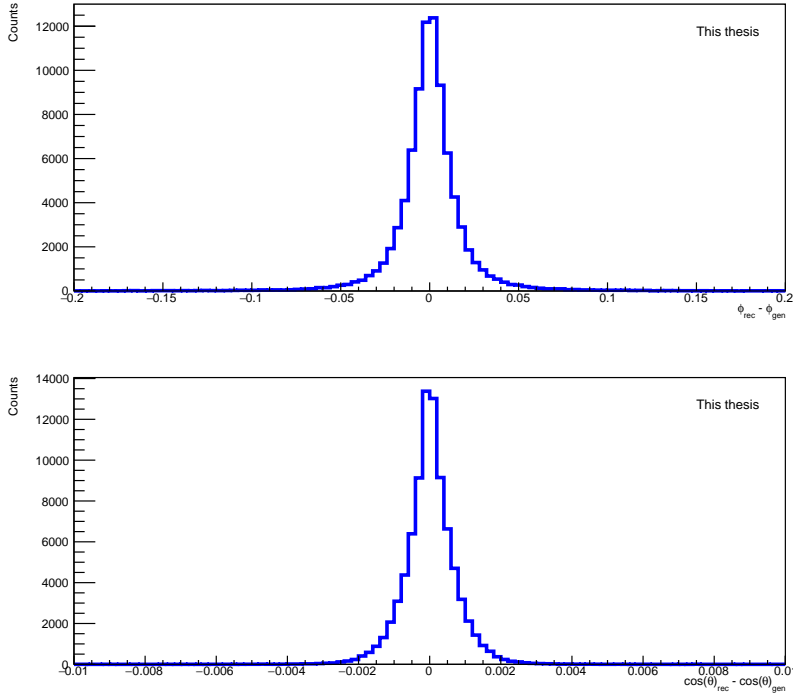
**Figure 7.3:** Resolution in $\phi$ (top) and $\cos\theta$ (bottom) for the incoherent photoproduction.

### 7.3.3 Acceptance and Efficiency

The acceptance and efficiency ($Acc \times \varepsilon$) is determined by the determination of a fraction of reconstructed events to generated events, i.e.

$$(Acc \times \varepsilon) = \frac{N_{rec}(\text{Sel1} - \text{Sel10})}{N_{gen}(\text{Sel5})}. \tag{7.2}$$

These corrections are crucial due to the limited performance of the detector both due to geometrical limitations (as shown in acceptance determination) and the limited performance of detectors. Detectors are affected by the conditions of the collisions, which influences their performance and might cause a decrease in the available number of detector elements. For the purposes of ($Acc \times \varepsilon$) determination, the criterion Sel2 is modified to (3.0; 3.2) GeV/$c^2$ in order to determine correction in the J/$\psi$ peak.

The ($Acc \times \varepsilon$) for both the coherent and incoherent photoproduction is determined in bins chosen above and shown in Figure 7.4. The left-hand side plot shows the ($Acc \times \varepsilon$) distribution with respect to two-dimensional distribution ($\cos\theta, \phi$) for coherent photoproduction, whereas the right-hand side plot shows the same distribution for incoherent photoproduction. Both types of photoproduction show a strong dependence on both $\cos\theta$ and $\phi$ distribution. The empty bins correspond to holes observed in the acceptance of the detector. The overall ($Acc \times \varepsilon$) for coherent production was determined as ($Acc \times \varepsilon$)$_{coh} = 0.042$ and for incoherent ($Acc \times \varepsilon$)$_{incoh}$ = 0.022.
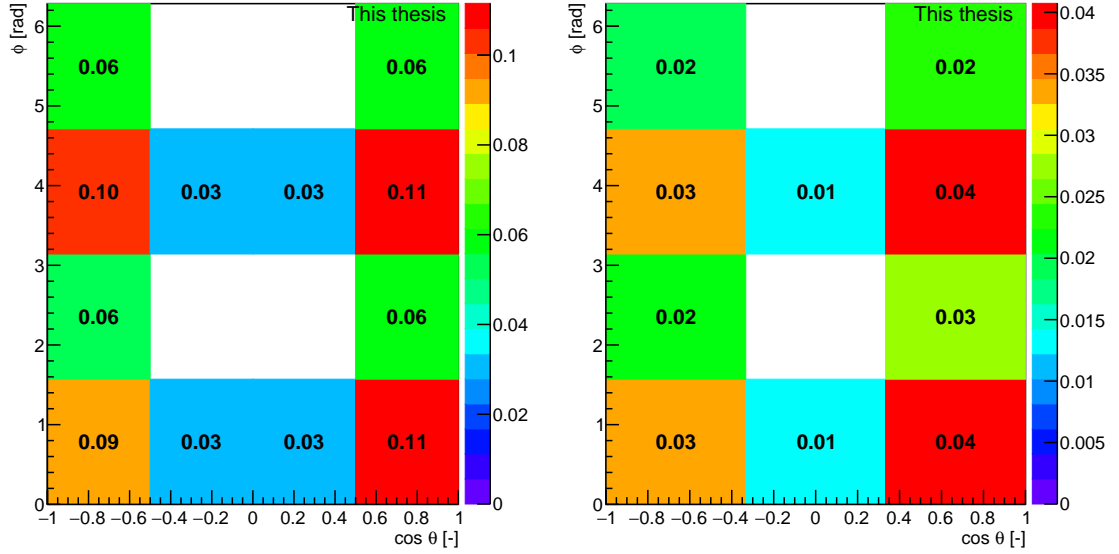
**Figure 7.4:** The $(Acc \times \varepsilon)$ distribution in the two-dimensional plane $(\cos\theta, \phi)$ for coherent (left) and incoherent (right) photoproduction.

## 7.4 Invariant Mass Distribution

The raw distribution of the invariant mass spectrum of $J/\psi$ both for coherent and incoherent events is determined by the Crystal Ball (CB) function fitted to the peak of $J/\psi$ resonance and exponential function was fitted to the background coming from two-photon processes. The CB function resembles a Gaussian distribution with an added power-law tail. The CB function [55] is defined in (7.3). The power law tail is added in a way that keeps the possibility of a continuous first derivative. In total there are 4 parameters $\bar{x}, \sigma, \alpha, n$. The parameters $\alpha$ and $n$ are parameters of the tail, the first determines a threshold for the tail to appear and the second is the parameter of the power law. These parameters are determined by a fit of invariant mass distribution of MC reconstructed data sample and are set to be fixed for the fit of measured data sample using the MLM parameter estimation.

$$f(x; \alpha, n, \bar{x}, \sigma) = e^{-\frac{1}{2}\left(\frac{x-\bar{x}}{\sigma}\right)^2} \quad \text{for} \quad \frac{x-\bar{x}}{\sigma} > -\alpha \tag{7.3}$$

$$= \left(\frac{n}{|\alpha|}\right)^n e^{-\frac{|\alpha|^2}{2}} \left(\frac{n}{|\alpha|} - |\alpha| - \frac{x-\bar{x}}{\sigma}\right)^{-n} \quad \text{for} \quad \frac{x-\bar{x}}{\sigma} \leq -\alpha.$$

The fit of the coherent data sample is shown in Figure 7.5, for incoherent in Figure 7.6. The plots show the invariant mass fit of full distributions in $\cos\theta$ and $\phi$. Resulting number of $J/\psi$s of coherent sample is $N_{J/\psi}^{coh} = 3034.4 \pm 60.1$ and of the incoherent $N_{J/\psi}^{incoh} = 559.6 \pm 27.4$. In the Appendix are shown invariant mass fits for each bin of studied distribution excluding those discussed above.
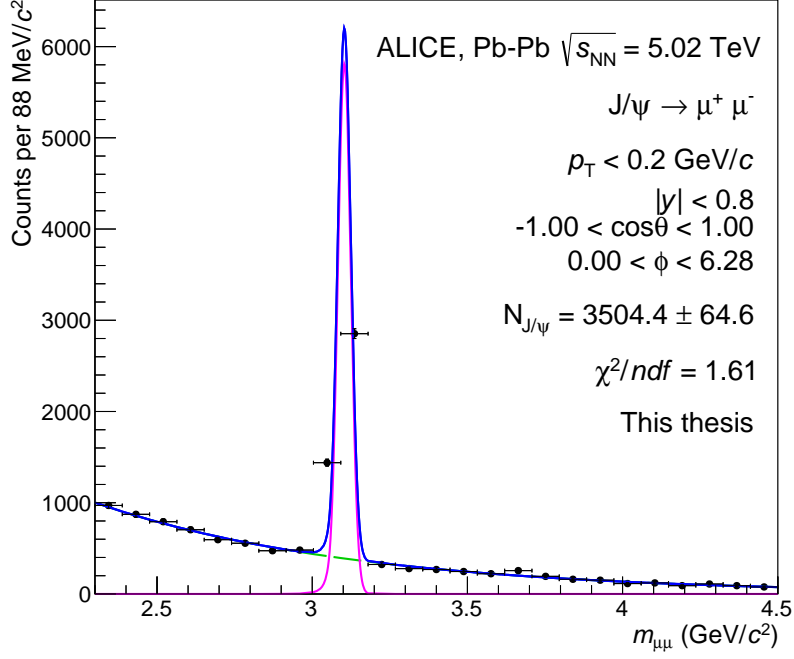
**Figure 7.5:** Fit of the invariant mass distribution of dimuon pairs from the coherent sample. The magenta line shows the CB function, green displays the exponential function describing the background and blue shows the model for full distribution.
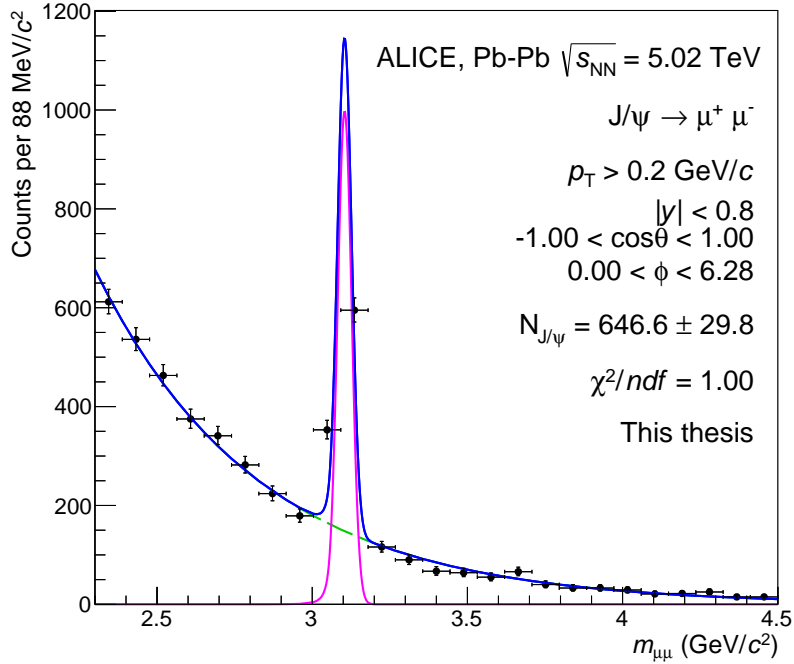


**Figure 7.6:** Fit of the invariant mass distribution of dimuon pairs from the incoherent sample. The magenta line shows the CB function, green displays the exponential function describing the background and blue shows the model for full distribution.

## 7.5 Coherent and Incoherent Contamination

The coherent and incoherent events are chosen based on a cut in $p_T$ of 0.2 GeV. Even though this cut provides a reasonable cut for the determination of the type of photo-

production, it is possible to observe contamination of coherent sample by incoherent events and vice versa. A detailed study of all possible sources of contamination for coherent photoproduction is given in [56].

The incoherent contamination of coherent sample $f_I$ is determined as a fraction of incoherent events to coherent events with $p_T < 0.2$ GeV. For the coherent contamination of the incoherent sample, $f_C$ is given as a fraction of coherent events to the incoherent sample with $p_T > 0.2$ GeV. The final yield is given as

$$N_{coh} = \frac{N_{yield}^{coh}}{1 + f_I} \qquad N_{incoh} = \frac{N_{yield}^{incoh}}{1 + f_C}, \tag{7.4}$$

where $N_{yield}^{coh}$ and $N_{yield}^{incoh}$ are yields obtained from mass fit and corrected for acceptance and efficiency effects. The overall incoherent contamination in the coherent data sample was calculated as $f_I = 0.061$. The overall coherent contamination of the sample was calculated as $f_C = 0.012$. These contaminations were calculated in each bin of the $(\cos\theta, \phi)$ distribution with results for $f_I$ shown in the top of Figure 7.8 and for $f_C$ shown in the bottom.
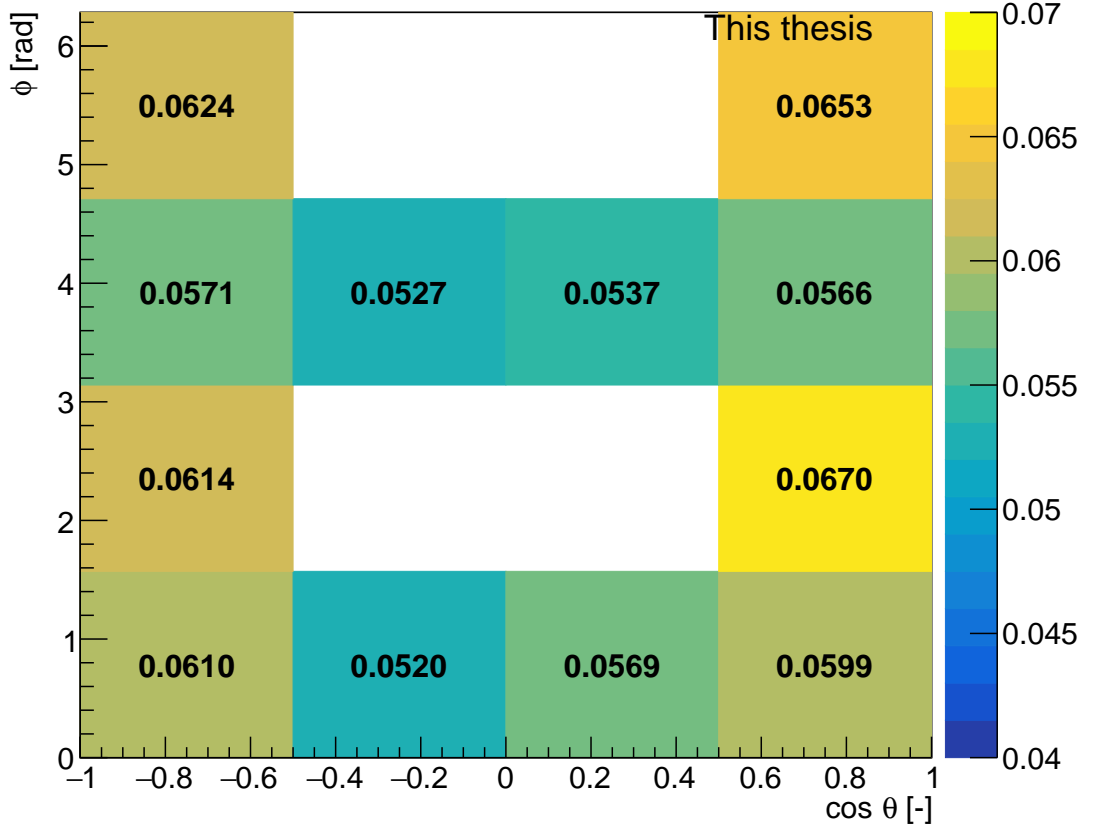


**Figure 7.7:** The two-dimensional distribution of incoherent contamination $f_I$ of coherent sample in the $(\cos\theta, \phi)$ plane.
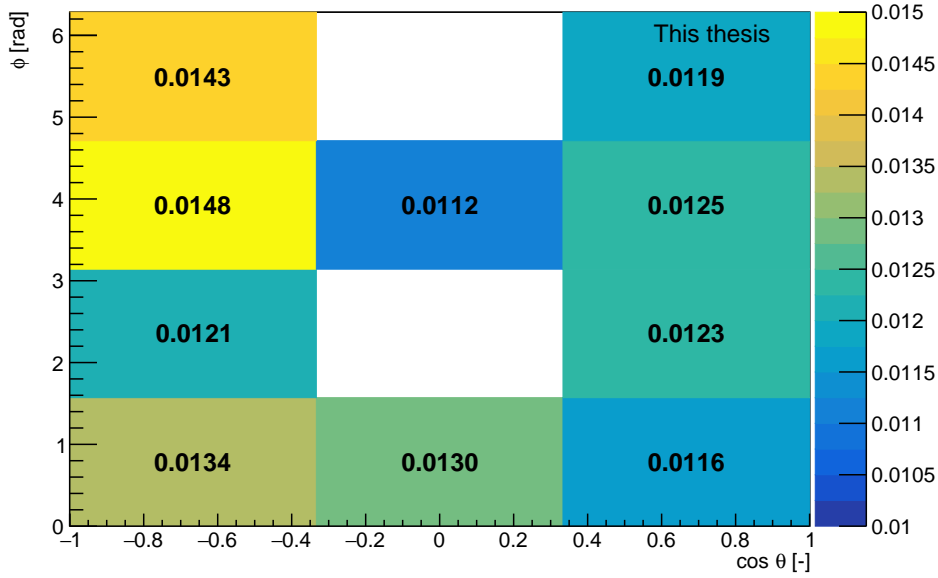
**Figure 7.8:** The two-dimensional distribution of coherent contamination of incoherent sample $f_C$ in the $(\cos\theta, \phi)$ plane.

# 7.6   Quantum Tomography Procedure

The first step of the quantum tomography procedure, the determination of $\hat{\ell}_J$ is performed on raw data that passed event selections Sel1 - Sel10. Before the determination of density matrices, the data was corrected, as described above, for the effect of the detector and possible contaminations of samples and for the exclusion of empty areas in the data. Resulting distributions in the two-dimensional plane $(\cos\theta, \phi)$ for coherent and incoherent distribution are shown.

The corrected yield incorporates above mentioned excluded areas. Before creating a model to describe angular distribution with such specific properties, the first step is to verify the procedure on a one-dimensional fit.

The function for fitting of one-dimensional distribution in $\cos\theta$ and $\phi$ is determined by integrating the $\frac{dN}{d\Omega}$ distribution with a reduced number of parameters (3.23) in given areas. The $\phi$ distribution takes into account two continuous stripes for $\cos\theta \in (-1.0, -0.5) \cup (0.5, 1.0)$. Due to different choices of binning in the incoherent sample, the continuous stripes are $\cos\theta \in (-1.0, -0.3) \cup (0.3, 1.0)$. The $\frac{dN}{d\phi}$ for coherent photoproduction is given as a sum of two integrals of $\frac{dN}{d\Omega}$ over $\sin\theta$ $0 < \theta < 0.25\pi$ and $0.75\pi < \theta < \pi$. For the incoherent photoproduction intervals for integration are $0 < \theta < -0.39\pi$ and $0.6\pi < \theta < \pi$. The distribution in $\cos\theta$, i.e. $\frac{dN}{d\cos\theta}$, is determined by integrating over $\phi$ in the intervals of $0 < \phi < 0.5\pi$ and $\pi < \phi < 1.5\pi$ both for coherent and incoherent distribution. The distributions are formulated in (7.5) for $\frac{dN}{d\phi}$ of coherent production, (7.7) for $\frac{dN}{d\cos\theta}$ for both coherent and incoherent production and (7.6) for incoherent $\frac{dN}{d\phi}$.
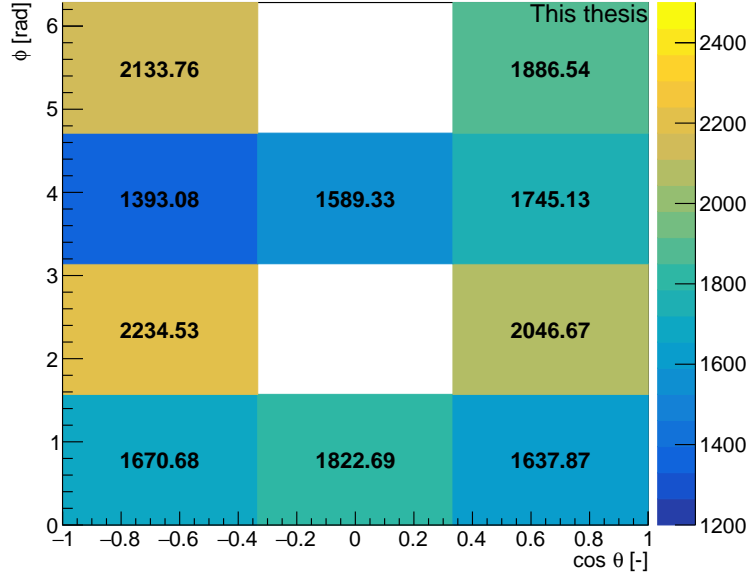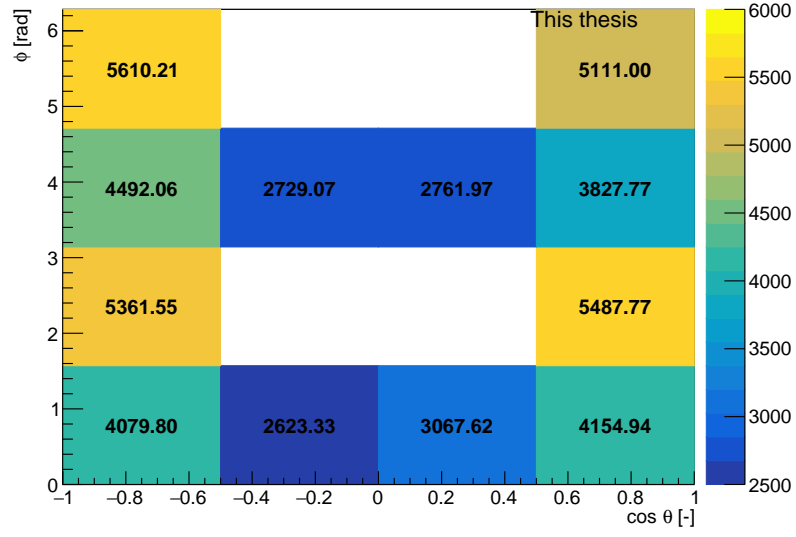
**Figure 7.9:** The corrected yield of coherent (top) and incoherent (bottom) photoproduction in the $(\cos\theta, \phi)$ plane.

$$\frac{dN}{d\phi}_c = N_c \cdot (0.146(1 + m_3^2)$$
$$+ 0.108(1 - 3m_3^2)$$
$$+ 0.039(2m_2^2 + m_3^2 - 1)\cos{(2\phi + 0.5\pi)}), \qquad (7.5)$$

$$
\begin{aligned}
\frac{dN}{d\phi}_i =& N_i \cdot (0.338(1 + m_3^2) \\
& + 0.161(1 - 3m_3^2) \\
& + 0.009 m_3 (\sqrt{1 - m_3^2 - m_2^2}) \cos{(\phi + 0.25\pi)} \\
& + 0.177(2m_2^2 + m_3^2 - 1)cos(2\phi + 0.5\pi)),
\end{aligned}
\tag{7.6}
$$

$$
\begin{aligned}
\frac{dN}{d\cos\theta}_i =& N \cdot (0.785(1 + m_3^2) \\
& + 0.785(1 - 3m_3^2)\cos^2\theta \\
& - 0.5(2m_2^2 + m_3^2 - 1)\sin^2\theta \\
=& \frac{dN}{d\cos\theta}_c.
\end{aligned}
\tag{7.7}
$$

The one-dimensional distributions are fitted both to the measured data sample as well as to the MC-generated sample that was already studied in Chapter 6. The MC sample is treated exactly the same way as the measured data in order to obtain comparable results.

### 7.6.1 MC Parameter Estimation

MC data sample studied in Chapter 6 is filled into two one-dimensional histograms in $\cos\theta$ and $\phi$. The distributions are afterwards fitted using a simultaneous fit of the two distributions. The distributions share two parameters $m_2$ and $m_3$ with factor $N$ corresponding to a normalization of a given sample.

**Coherent Production**

Fitted distributions by a method described above are shown in Figure 7.10. The top figure displays the fit of distribution of transversely ($\chi^2/ndf = 1.69$) polarized mother particle, the middle longitudinal ($\chi^2/ndf = 4.5$) and the bottom shows a sample without polarization ($\chi^2/ndf = 0.9$). Even after projecting only two strips of the distribution, each of the polarizations kept its distinguishable shape, or for the unpolarized case no specific shape. Blue line in the histograms displays fitted $\frac{dN}{d\phi}$ distribution, red the $\frac{dN}{d\cos\theta}$ distribution. Similarly to the case of full distribution, even here were calculated density matrices for each polarization state together with the $\lambda$ parameters for polarization state determination.

The resulting density matrices are simplified in comparison with those in Chapter 6, however, it is still possible to observe similar values of the diagonal elements of each matrix. The same applies to the $\lambda$ parameters. These are highly affected by goodness-of-fit, however comparing the invariant $\tilde{\lambda}$ with previously yielded results, we observe expected behaviour. The values are listed in Table 7.2.
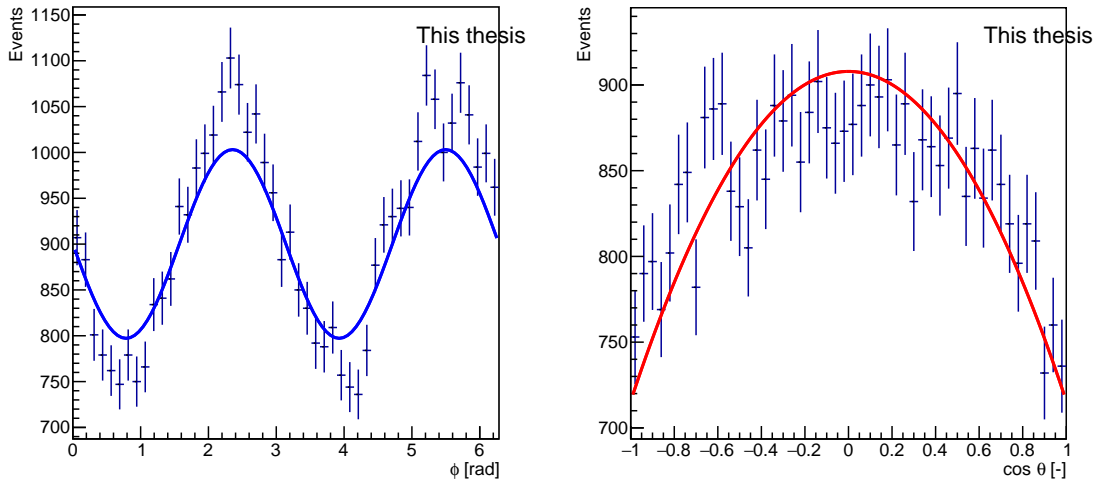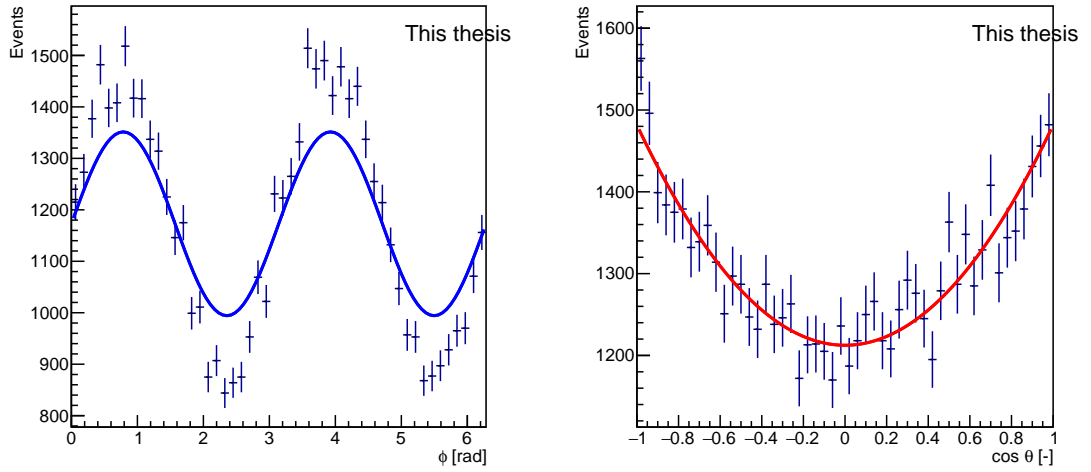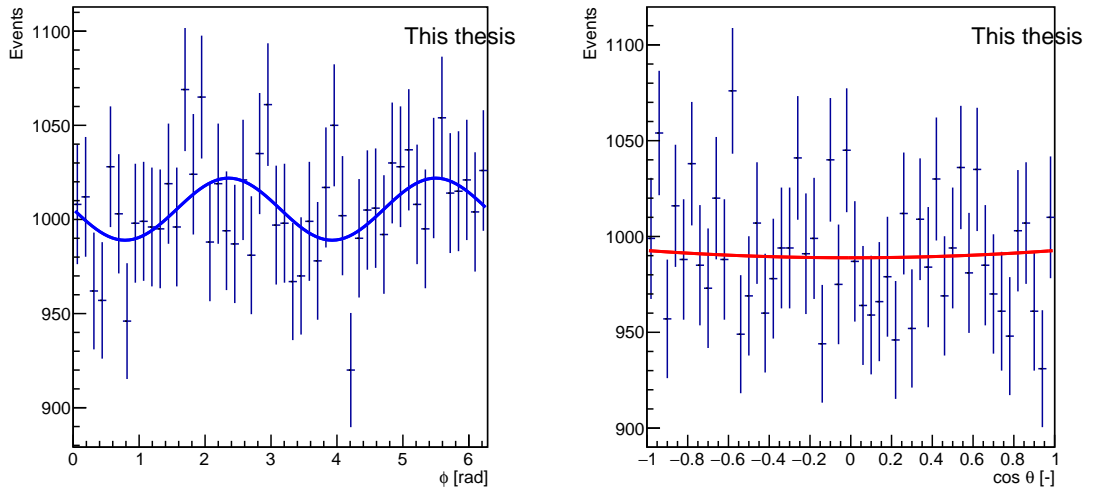
**Figure 7.10:** Simultaneously fitted distributions of MC data sample of coherently pro-
duced J/$\psi$ in $\cos\theta$ and $\phi$ with the fitting functions (7.7) on the right-hand size (red) and
(7.5) on the left-hand side (blue).

$$\rho_{fit}^{trans} = \begin{pmatrix} 0.000044 & 0 & 0.004807 \\ 0 & 0.479137 & 0 \\ 0.004807 & 0 & 0.520819 \end{pmatrix}, \tag{7.8}$$

$$\rho_{fit}^{long} = \begin{pmatrix} 1 & 0 & 0.00018 \\ 0 & 0 & 0 \\ 0.00018 & 0 & 0 \end{pmatrix}, \tag{7.9}$$

$$\rho_{fit}^{unpol} = \begin{pmatrix} 0.28471 & 0 & 0.31521 \\ 0 & 0.36629 & 0 \\ 0.31521 & 0 & 0.53357 \end{pmatrix}, \tag{7.10}$$

| Transverse | | Longitudinal | | Unpolarized | |
|---|---|---|---|---|---|
| $\lambda_\theta$ | -0.3698 | $\lambda_\theta$ | 1 | $\lambda_\theta$ | -0.0348 |
| $\lambda_\phi$ | 0.3150 | $\lambda_\phi$ | -1 | $\lambda_\phi$ | 0.0605 |
| $\lambda_{\theta\phi}$ | -0.3698 | $\lambda_{\theta\phi}$ | -0.00036 | $\lambda_{\theta\phi}$ | -0.4773 |
| $\tilde{\lambda}$ | 0.8397 | $\tilde{\lambda}$ | -1 | $\tilde{\lambda}$ | 0.1560 |

**Table 7.2:** Polarization parameters $\lambda_\theta, \lambda_\phi, \lambda_{\theta\phi}$ and $\tilde{\lambda}$ calculated from fit parameters as in (3.27) with frame invariant parameter $\tilde{\lambda}$ for coherent J/$\psi$ with MC treated the same as data.

**Incoherent production**

A similar discussion as in the coherent production can be applied here. The incoherent data sample also kept its original shape of a distribution. The goodness-of-fit in all three polarization states is reasonable and can be considered better than in the coherent case. This is caused by a smaller reduction of data in $\phi$ distribution. The goodness-of-fit parameters are $\chi^2/ndf = 0.76$ for the transverse polarization, $\chi^2/ndf = 1.04$ for longitudinal and for the unpolarized state $\chi^2/ndf = 0.71$. The $\lambda$ parameters are shown in Table 7.3 showing expected results based on a full MC data sample.

$$\rho_{fit}^{trans} = \begin{pmatrix} 0.0432 & 0 & 0.1400 \\ 0 & 0.5035 & 0 \\ 0.1400 & 0 & 0.4533 \end{pmatrix}, \tag{7.11}$$

$$\rho_{fit}^{long} = \begin{pmatrix} 0.8870 & 0 & 0.2958 \\ 0 & 0.01434 & 0 \\ 0.2958 & 0 & 0.0986 \end{pmatrix}, \tag{7.12}$$

$$\rho_{fit}^{unpol} = \begin{pmatrix} 0.3030 & 0 & 0.3327 \\ 0 & 0.3513 & 0 \\ 0.3327 & 0 & 0.3457 \end{pmatrix}, \tag{7.13}$$
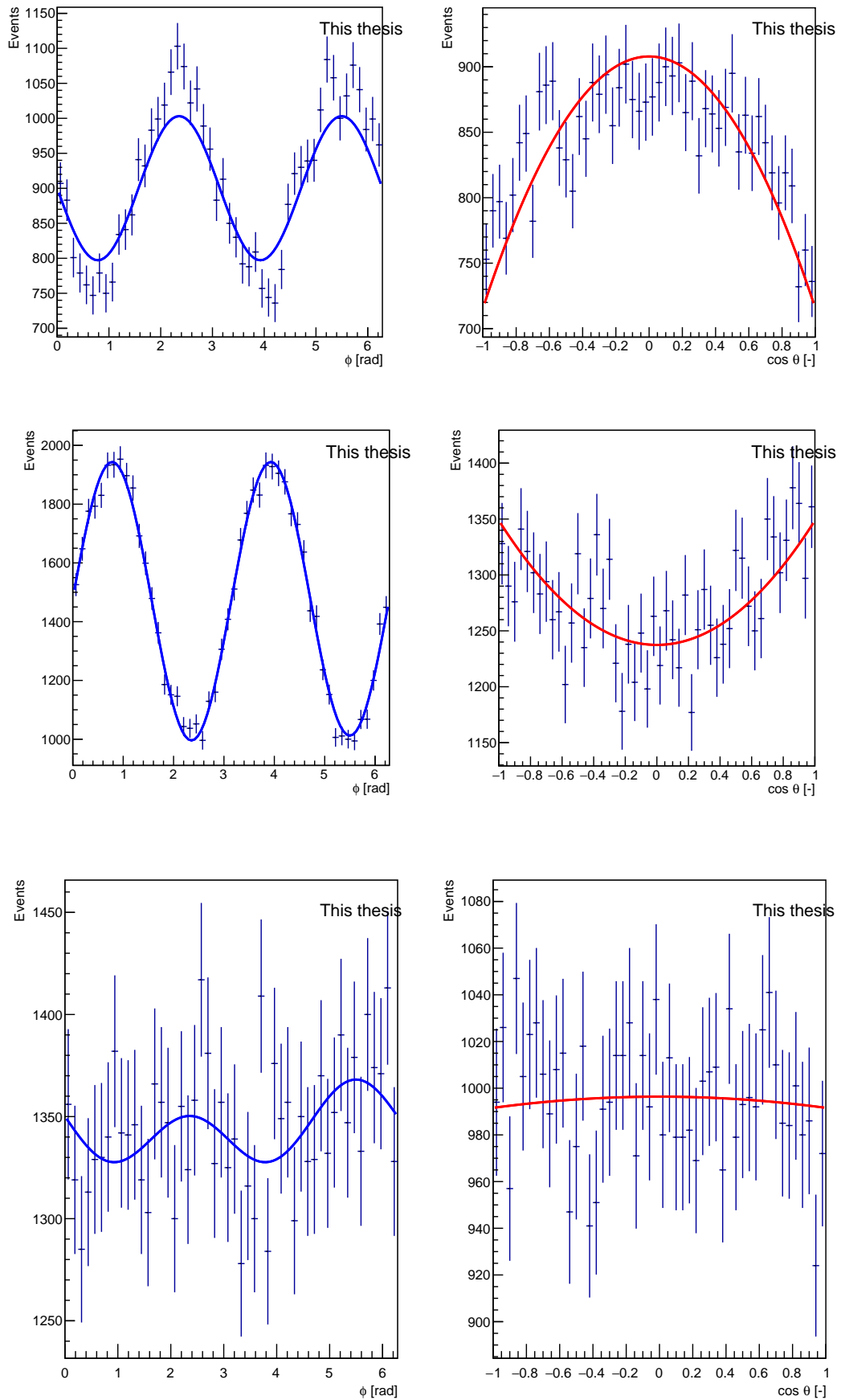
**Figure 7.11:** Simultaneously fitted distributions of MC data sample of coherently produced J/ψ in cos θ and φ with the fitting functions (7.7) on the right-hand size (red) and (7.5) on the left-hand side (blue).

| Transverse | | Longitudinal | | Unpolarized | |
|---|---|---|---|---|---|
| $\lambda_\theta$ | -0.2475 | $\lambda_\theta$ | 0.6410 | $\lambda_\theta$ | -0.02755 |
| $\lambda_\phi$ | 0.3167 | $\lambda_\phi$ | -0.7934 | $\lambda_\phi$ | 0.03587 |
| $\lambda_{\theta\phi}$ | -0.1927 | $\lambda_{\theta\phi}$ | -0.5384 | $\lambda_{\theta\phi}$ | -0.48102 |
| $\tilde{\lambda}$ | 1.0280 | $\tilde{\lambda}$ | -0.9709 | $\tilde{\lambda}$ | 0.0830 |

**Table 7.3:** Polarization parameters $\lambda_\theta, \lambda_\phi, \lambda_{\theta\phi}$ and $\tilde{\lambda}$ calculated from fit parameters as in (3.27) with frame invariant parameter $\tilde{\lambda}$ for incoherent J/$\psi$ with MC treated the same as data.

## 7.6.2   Data Parameter Estimation

The corrected data sample both for coherent and incoherent photoproduction is fitted with the same functions as the MC data sample. Resulting fits are shown in Figure 7.12 for coherent production and Figure 7.13 for incoherent.
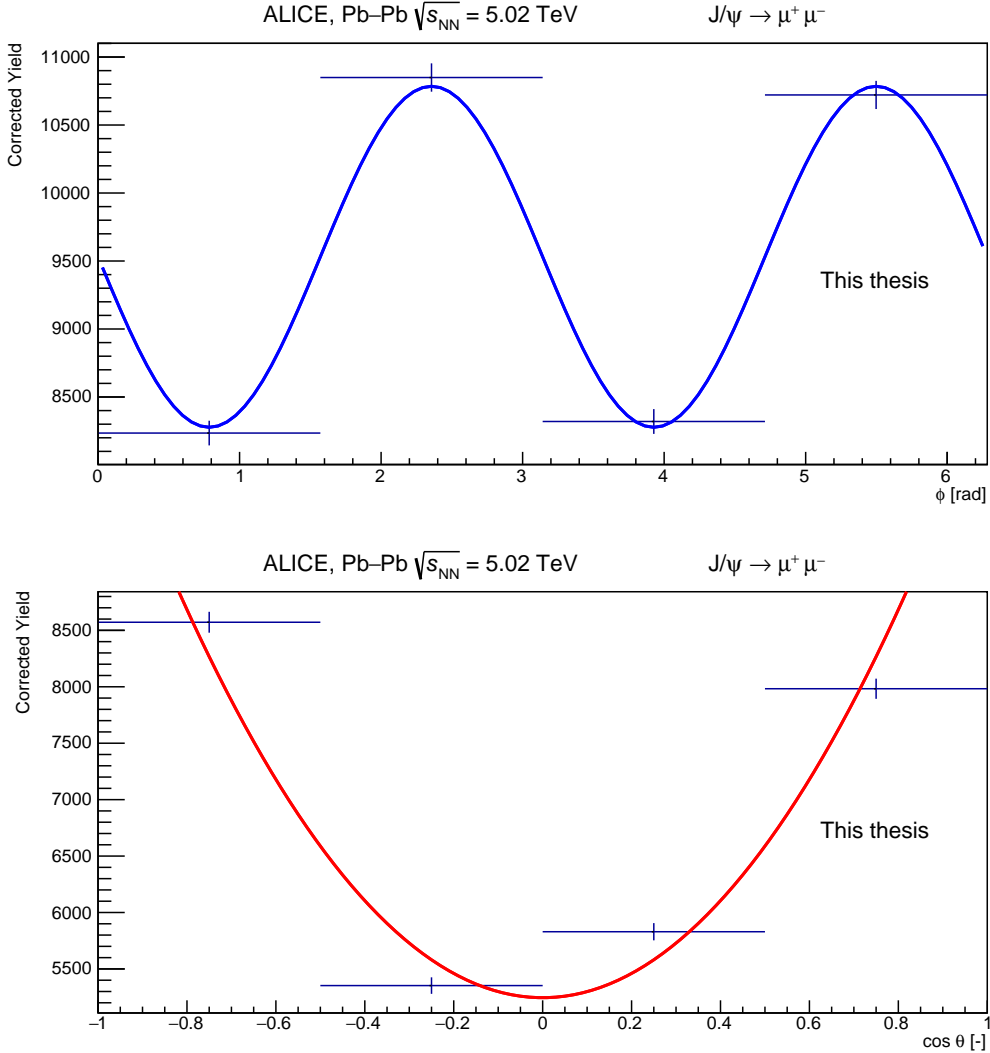


**Figure 7.12:** Corrected yield of the coherent data sample. Plots show projections of strips of two-dimensional distribution (see text) fitted with (7.5) (top) and (7.7) (bottom).
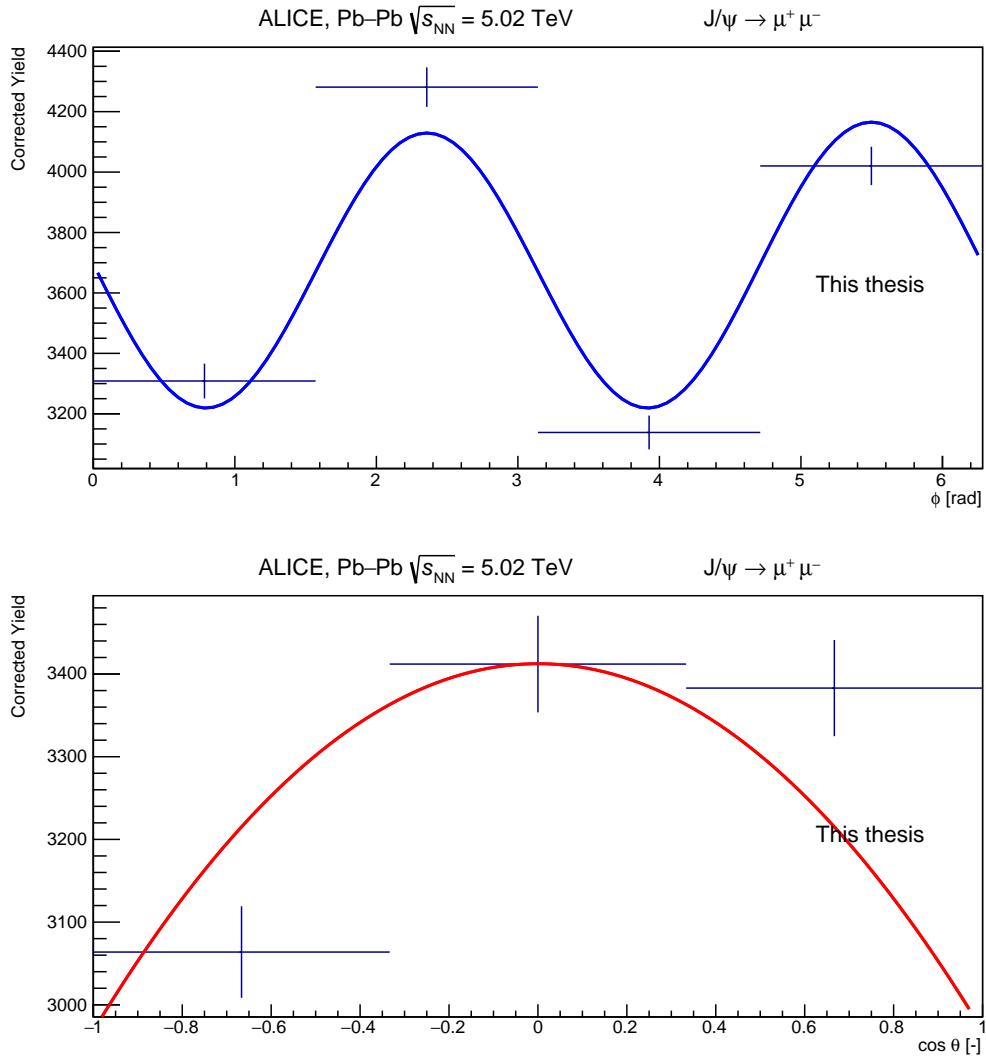
**Figure 7.13:** Corrected yield of the coherent data sample. Plots show projections of strips of two-dimensional distribution (see text) fitted with (7.5) (top) and (7.7) (bottom).

The coherent data sample shows the distribution in $\phi$ comparable to the MC transverse polarization. However, the distribution in $\cos\theta$ resembles the one for longitudinal polarization. On the MC data sample, there is an obvious reduction in the number of events with the exclusion of strips based on detector inefficiencies. This results in a slight flattening of the $\cos\theta$ distribution shape. This flattening behaviour is observed solely for a larger number of bins than in the available data sample.

The determination of the source of this strange behaviour of data is a complex problem. There were several corrections applied to the data beginning with the invariant mass fit. The next step was the acceptance and efficiency correction to account for any detector effects. The distribution of $(Acc \times \varepsilon)$ shows significant angular dependence of the detector performance around the beam pipe ($\phi$ dependence) and in the perpendicular direction (cos). Even though the $(Acc \times \varepsilon)$ accounts for the detector inefficiencies, in the area of $\cos\theta \in (-0.5; 0.5)$ they increase by approximately 60% - 80% in comparison with the side-band areas.

The second correction is the correction for the incoherent contamination. As well as

($Acc \times \varepsilon$) This distribution shows angular dependence, however with significantly smaller fluctuations with respect to $\cos\theta$. The $\cos\theta$ distribution also has slight asymmetry around $\cos\theta = 0$ introduced by the raw data while none of the corrections managed to account for that. The nonphysical results of the density matrix together with polarization parameters will not be mentioned.

The incoherent data sample shows an interesting distribution in $\cos\theta$ while again showing similar distribution in $\phi$ as the transversely polarized MC data sample. The distribution in $\cos\theta$ shows desired concave shape as observed in the transversely polarized MC. Resulting density matrix of incoherent $J/\psi$ is given as

$$\rho_{fit}^{incoh} = \begin{pmatrix} 0.12 & 0 & 0.23 \\ 0 & 0.43 & 0 \\ 0.23 & 0 & 0.453 \end{pmatrix} \pm \begin{pmatrix} 0.03 & 0 & 0.03 \\ 0 & 0.03 & 0 \\ 0.03 & 0 & 0.018 \end{pmatrix} \text{(stat.)}, \qquad (7.14)$$

with matrix element errors calculated by error propagation from errors of fit parameters. Comparing this result to MC results, the measured $\rho_{fit}^{incoh}$ is, within uncertainties, approaching $\rho_{fit}^{trans}$ of the incoherent data sample. Calculated $\lambda$ parameters are shown in 7.4. The frame dependent parameters $\lambda_\phi, \lambda_\theta, \lambda_{\phi\theta}$ are again approaching values of transverse MC incoherent sample. The errors are calculated using error propagation from errors of fit parameters. The errors are fluctuating around 10% of the calculated value, whereas the invariant variable $\tilde{\lambda}$ shows uncertainty around 20%.

| Incoherent Yield | |
|---|---|
| $\lambda_\theta$ | -0.25 $\pm$ 0.03 |
| $\lambda_\phi$ | 0.212 $\pm$ 0.019 |
| $\lambda_{\theta\phi}$ | -0.31 $\pm$ 0.02 |
| $\tilde{\lambda}$ | 0.49 $\pm$ 0.09 |

**Table 7.4:** Calculated values of $\lambda$ polarization parameters from fit parameters as for the MC data sample for measured incoherently produced $J/\psi$.

The incoherent sample of measured data provides us with results in approaching results of the MC data sample of incoherent transversely polarized. This is in agreement with the assumption from helicity conservation expecting the vector meson to be transversely polarized.

Comparing coherent and incoherent data, the coherent sample shows stronger sensitivity to low acceptance in $\cos\theta \in (-0.5; 0.5)$. Even though the incoherent sample is also affected, the distribution is flatter than for coherent data. The specific shape of the distribution is most likely given by chosen reference CS frame. While the tomography procedure is independent of the reference frame, the observed distributions are not, thus in another reference frame, the coherent sample could provide desirable results, however, this has not been studied.

# Summary

The study of the structure of hadrons and elementary particles has occupied scientist for decades and yet, this journey is nowhere close to its end. Chapter 1 briefly introduces the long journey from the pioneering experiments on elastic scattering of electron on protons to the formulation of evolution equations based on the theory of Quantum Chromodynamics.

The inner structure and properties of hadrons can be probed through variety of tools, one of which is the polarization of intermediate state created in collision of said hadrons. The polarization is sensitive not only on the production process behind the creation of an intermediate state, but also on the kinematics of such process and of an event in general. Aim of this thesis is the study of polarization of J/$\psi$ vector meson and short introduction into classical procedure of polarization studied of quarkonia is presented in Chapter 2.

The traditional studies of quarkonium polarization show significant results, however they are limited by its formalism and bases on reference frames. A unique opportunity for studies of quarkonium polarization and other crucial observables independent of reference frames and scattering models is the quantum tomography. The idea of quantum tomography came together with invention of quantum mechanical theories. However, it was limited by a lack of experimental methods to determine a quantum state and accompanying quantum process. Chapter 3 introduces basics of quantum mechanics in order to define density matrices. The density matrices describe a quantum state while carrying information about it various properties.

Following an introduction into a theory of applied procedure, an overview of studied events is presented. Chapter 4 introduces the theory of ultra-peripheral collisions together with their properties. It introduces basics of cross-section determination of such processes based on photon flux and photonuclear cross-section. In addition it mentions two-photon processes that create a small irreducible background in invariant mass distribution of exclusive J/$\psi$ photoproduction.

Studied data sample is measured on the ALICE experiment at the LHC at CERN. Chapter 5 presents several crucial discoveries and experiments at the LHC and it further focuses on the ALICE experiment and its detectors crucial for measurement of quarkonium production and triggers.

Last two chapters focus on the analysis of polarization of the J/$\psi$ vector meson. The first part, Chapter 5, focuses on application of quantum tomography procedure on Monte Carlo data generated by the EvtGen generator for decays of vector mesons with adjustable polarization state, together with PHOTOS for simulation of final state gamma radiation and Pythia for event simulation. Generated MC samples

include coherently and incoherently produced J/$\psi$ in three possible polarization states. An angular dependence of final state decay products is shown together with determination of density matrices and polarization parameters of each state.

Chapter 6 focuses on application of quantum tomography procedure on measured data. Data were measured during 2018 data taking of Pb-Pb collisions with centre-of-mass energy $\sqrt{s_{NN}} = 5.02$ TeV. A list of applied trigger and event selection criteria is presented together with correction on detector inefficiencies and possible coherent or incoherent contamination of incoherent-enriched or coherent-enriched sample. Final step is the application of quantum tomography on both MC and measured data, in similar fashion, in order to compare measured results with an ideal example. Even though coherent data sample shows no physical results, the incoherent data sample is in agreement with results of transversely polarized MC generated data. This finding could lead to further applications of quantum tomography procedures in variety of particle physics fields.

# Bibliography

[1] Jiri Chyla. "Quarks, partons and Quantum Chromodynamics". In: (Feb. 2004).

[2] Mark Thomson. *Modern particle physics*. New York: Cambridge University Press, 2013. ISBN: 978-1-107-03426-6. DOI: `10.1017/CBO9781139525367`.

[3] Robert Hofstadter. "Electron scattering and nuclear structure". In: *Rev. Mod. Phys.* 28 (1956), pp. 214–254. DOI: `10.1103/RevModPhys.28.214`.

[4] S. Chekanov et al. "A ZEUS next-to-leading-order QCD analysis of data on deep inelastic scattering". In: *Phys. Rev. D* 67 (2003), p. 012007. DOI: `10.1103/PhysRevD.67.012007`. arXiv: `hep-ex/0208023`.

[5] S. Chekanov et al. "ZEUS next-to-leading-order QCD analysis of data on deep inelastic scattering". In: *Physical Review D* 67.1 (Jan. 2003). ISSN: 1089-4918. DOI: `10.1103/physrevd.67.012007`. URL: `http://dx.doi.org/10.1103/PhysRevD.67.012007`.

[6] Nestor Armesto. "Nuclear shadowing". In: *J. Phys. G* 32 (2006), R367–R394. DOI: `10.1088/0954-3899/32/11/R01`. arXiv: `hep-ph/0604108`.

[7] Michal Krelina and Jan Nemchik. "Nuclear shadowing in DIS at electron-ion colliders". In: *Eur. Phys. J. Plus* 135.6 (2020), p. 444. DOI: `10.1140/epjp/s13360-020-00498-2`. arXiv: `2003.04156 [hep-ph]`.

[8] Dmitri Diakonov. *QCD scattering: From DGLAP to BFKL*. July 2010. URL: `https://cerncourier.com/a/qcd-scattering-from-dglap-to-bfkl/`.

[9] Pietro Faccioli et al. "Towards the experimental clarification of quarkonium polarization". In: *Eur. Phys. J. C* 69 (2010), pp. 657–673. DOI: `10.1140/epjc/s10052-010-1420-5`. arXiv: `1006.2738 [hep-ph]`.

[10] Andrea Bianconi and Marco Radici. "Monte Carlo simulation of events with Drell-Yan lepton pairs from antiproton-proton collisions: The Fully polarized case". In: *Phys. Rev. D* 72 (2005), p. 074013. DOI: `10.1103/PhysRevD.72.074013`. arXiv: `hep-ph/0504261`.

[11] J. Alcaraz Maestre. *Details on the Collins-Soper reference frame and lepton angular distributions in electroweak vector boson production at hadron colliders*. Madrid: Center for Energy, Environmental and Technological Research (CIEMAT), 2020.

[12] J.B. Altepeter, E.R. Jeffrey, and P.G. Kwiat. "Photonic State Tomography". In: ed. by P.R. Berman and C.C. Lin. Vol. 52. Advances In Atomic, Molecular, and Optical Physics. Academic Press, 2005, pp. 105–159. DOI: `https://doi.org/10.1016/S1049-250X(05)52003-2`. URL: `https://www.sciencedirect.com/science/article/pii/S1049250X05520032`.

[13]   John C. Martens, John P. Ralston, and J. D. Tapia Takaki. "Quantum to-
       mography for collider physics: Illustrations with lepton pair production". In:
       *Eur. Phys. J. C* 78.1 (2018), p. 5. DOI: `10.1140/epjc/s10052-017-5455-8`.
       arXiv: `1707.01638 [hep-ph]`.

[14]   Samia Ainouz et al. "Physical interpretation of polarization encoded image by
       color preview". In: *Optics express* 14 (June 2006), pp. 5916–27. DOI: `10.1364/
       OE.14.005916`.

[15]   U. Fano. "A Stokes-Parameter Technique for the Treatment of Polarization in
       Quantum Mechanics". In: *Phys. Rev.* 93 (1954), pp. 121–123. DOI: `10.1103/
       PhysRev.93.121`.

[16]   George Gabriel Stokes. "On the Composition and Resolution of Streams of
       Polarized Light from different Sources". In: *Mathematical and Physical Papers.*
       Vol. 3. Cambridge Library Collection - Mathematics. Cambridge University
       Press, 2009, pp. 233–258. DOI: `10.1017/CBO9780511702266.010`.

[17]   A. Bisio et al. "Optimal Quantum Tomography". In: *IEEE Journal of Selected
       Topics in Quantum Electronics* 15.6 (2009), pp. 1646–1660. DOI: `10.1109/
       jstqe.2009.2029243`. URL: `https://doi.org/10.11092Fjstqe.2009.
       2029243`.

[18]   D. T. Smithey et al. "Measurement of the Wigner distribution and the density
       matrix of a light mode using optical homodyne tomography: Application to
       squeezed states and the vacuum". In: *Phys. Rev. Lett.* 70 (1993), pp. 1244–
       1247. DOI: `10.1103/PhysRevLett.70.1244`.

[19]   Jaroslav Rehacek et al. "Surmounting intrinsic quantum-measurement uncer-
       tainties in Gaussian-state tomography with quadrature squeezing". In: *Scien-
       tific Reports* 5 (July 2015). DOI: `10.1038/srep12289`.

[20]   Eitan Av et al. "Direct reconstruction of the quantum-master-equation dy-
       namics of a trapped-ion qubit". In: *Physical Review A* 101 (June 2020). DOI:
       `10.1103/PhysRevA.101.062305`.

[21]   J. F. Poyatos, J. I. Cirac, and P. Zoller. "Complete Characterization of a
       Quantum Process: The Two-Bit Quantum Gate". In: *Phys. Rev. Lett.* 78 (2
       Jan. 1997), pp. 390–393. DOI: `10.1103/PhysRevLett.78.390`. URL: `https:
       //link.aps.org/doi/10.1103/PhysRevLett.78.390`.

[22]   Manuel Vogel. "Quantum Computation and Quantum Information, by M.A.
       Nielsen and I.L. Chuang". In: *Contemporary Physics* 52.6 (2011), pp. 604–605.
       DOI: `10.1080/00107514.2011.587535`. eprint: `https://doi.org/10.1080/
       00107514.2011.587535`. URL: `https://doi.org/10.1080/00107514.2011.
       587535`.

[23]   Isaac L. Chuang and M. A. Nielsen. "Prescription for experimental determi-
       nation of the dynamics of a quantum black box". In: *J. Mod. Opt.* 44 (1997),
       p. 2455. DOI: `10.1080/09500349708231894`. arXiv: `quant-ph/9610001`.

[24]   G. M. D'Ariano and P. Lo Presti. "Quantum Tomography for Measuring Ex-
       perimentally the Matrix Elements of an Arbitrary Quantum Operation". In:
       *Physical Review Letters* 86.19 (May 2001), pp. 4195–4198. DOI: `10.1103/
       physrevlett.86.4195`. URL: `https://doi.org/10.11032Fphysrevlett.
       86.4195`.

[25]  J. B. Altepeter et al. "Ancilla-Assisted Quantum Process Tomography". In: *Physical Review Letters* 90.19 (May 2003). DOI: `10.1103/physrevlett.90.193601`. URL: `https://doi.org/10.11032Fphysrevlett.90.193601`.

[26]  Giacomo Mauro D'Ariano and Paoloplacido Lo Presti. "Imprinting Complete Information about a Quantum Channel on its Output State". In: *Physical Review Letters* 91.4 (July 2003). DOI: `10.1103/physrevlett.91.047902`. URL: `https://doi.org/10.11032Fphysrevlett.91.047902`.

[27]  K J le Couteur. "The Dirac density matrix". In: *Proceedings of the Physical Society* 84.6 (Dec. 1964), p. 837. DOI: `10.1088/0370-1328/84/6/301`. URL: `https://dx.doi.org/10.1088/0370-1328/84/6/301`.

[28]  Nicholas Higham. "Analysis of the Cholesky Decomposition of a Semi-Definite Matrix". In: (Mar. 2000).

[29]  J. G. Contreras. "Gluon shadowing at small $x$ from coherent J/$\psi$ photoproduction data at energies available at the CERN Large Hadron Collider". In: *Phys. Rev. C* 96.1 (2017), p. 015203. DOI: `10.1103/PhysRevC.96.015203`. arXiv: `1610.03350 [nucl-ex]`.

[30]  Carlos A. Bertulani, Spencer R. Klein, and Joakim Nystrand. "Physics of ultra-peripheral nuclear collisions". In: *Ann. Rev. Nucl. Part. Sci.* 55 (2005), pp. 271–310. DOI: `10.1146/annurev.nucl.55.090704.151526`. arXiv: `nucl-ex/0502005`.

[31]  J. G. Contreras and J. D. Tapia Takaki. "Ultra-peripheral heavy-ion collisions at the LHC". In: *Int. J. Mod. Phys. A* 30 (2015), p. 1542012. DOI: `10.1142/S0217751X15420129`.

[32]  E. Iancu, K. Itakura, and S. Munier. "Saturation and BFKL dynamics in the HERA data at small x". In: *Phys. Lett. B* 590 (2004), pp. 199–208. DOI: `10.1016/j.physletb.2004.02.040`. arXiv: `hep-ph/0310338`.

[33]  G. Soyez. "Saturation QCD predictions with heavy quarks at HERA". In: *Phys. Lett. B* 655 (2007), pp. 32–38. DOI: `10.1016/j.physletb.2007.07.076`. arXiv: `0705.3672 [hep-ph]`.

[34]  T. Lappi and H. Mantysaari. "*J/|psi* production in ultraperipheral Pb+Pb and $p$+Pb collisions at energies available at the CERN Large Hadron Collider". In: *Phys. Rev. C* 87.3 (2013), p. 032201. DOI: `10.1103/PhysRevC.87.032201`. arXiv: `1301.4095 [hep-ph]`.

[35]  Gerhard Baur et al. "Coherent gamma gamma and gamma-A interactions in very peripheral collisions at relativistic ion colliders". In: *Phys. Rept.* 364 (2002), pp. 359–450. DOI: `10.1016/S0370-1573(01)00101-6`. arXiv: `hep-ph/0112211`.

[36]  Xabier Cid Vidal and Ramon Cid Manzano. *Taking a closer lok at LHC - CERN in short.* `http://www.lhc-closer.es/taking_a_closer_look_at_lhc/0.cern_in_short`. [Online; accessed 11/03/2023].

[37]  Jorg Wenninger. "Operation and Configuration of the LHC in Run 2". In: (2019). URL: `https://cds.cern.ch/record/2668326`.

[38]  Ewa Lopienska. "The CERN accelerator complex, layout in 2022. Complexe des accélérateurs du CERN en janvier 2022". In: (2022). General Photo. URL: `https://cds.cern.ch/record/2800984`.

[39] K. Aamodt et al. "The ALICE experiment at the CERN LHC". In: *JINST* 3 (2008), S08002. DOI: 10.1088/1748-0221/3/08/S08002.

[40] Arturo Tauro. "ALICE Schematics". General Photo. 2017. URL: https://cds.cern.ch/record/2263642.

[41] *ALICE Inner Tracking System (ITS): Technical Design Report*. Technical design report. ALICE. Geneva: CERN, 1999. URL: https://cds.cern.ch/record/391175.

[42] G Dellacasa et al. *ALICE time projection chamber: Technical Design Report*. Technical design report. ALICE. Geneva: CERN, 2000. URL: https://cds.cern.ch/record/451098.

[43] J. Alme et al. "The ALICE TPC, a large 3-dimensional tracking device with fast readout for ultra-high multiplicity events". In: *Nucl. Instrum. Meth. A* 622 (2010), pp. 316–367. DOI: 10.1016/j.nima.2010.04.042. arXiv: 1001.1950 [physics.ins-det].

[44] Bjorn S. Nilsen. "Heavy-flavor production in LHC pp interactions using the ALICE detector". In: *Nucl. Phys. B Proc. Suppl.* 233 (2013). Ed. by Marco Bozzo et al., pp. 201–206. DOI: 10.1016/j.nuclphysbps.2012.12.077. arXiv: 1210.7847 [hep-ex].

[45] Betty Bezverkhny Abelev et al. "Performance of the ALICE Experiment at the CERN LHC". In: *Int. J. Mod. Phys. A* 29 (2014), p. 1430044. DOI: 10.1142/S0217751X14300440. arXiv: 1402.4476 [nucl-ex].

[46] P Cortese et al. "ALICE technical design report on forward detectors: FMD, T0 and V0". In: (Sept. 2004).

[47] Jean-Yves Grossiord. "The V0 detector is two disks of counters in both sides of the interaction point." ALICE Collection. 2006. URL: https://cds.cern.ch/record/1045976.

[48] "One of the eight sectors of the V0A trigger hodoscope." ALICE Collection. 2005. URL: https://cds.cern.ch/record/975945.

[49] G. Herrera Corral. "Diffractive Physics with ALICE at the LHC: the control of quantum collisions". In: *J. Phys. Conf. Ser.* 624.1 (2015). Ed. by Nora Bretón, David Fernández, and Piotr Kielanowski, p. 012008. DOI: 10.1088/1742-6596/624/1/012008.

[50] Christian Bierlich et al. "A comprehensive guide to the physics and usage of PYTHIA 8.3". In: (Mar. 2022). DOI: 10.21468/SciPostPhysCodeb.8. arXiv: 2203.11601 [hep-ph].

[51] Johannes Bellm et al. "Herwig 7.0/Herwig++ 3.0 release note". In: *Eur. Phys. J. C* 76.4 (2016), p. 196. DOI: 10.1140/epjc/s10052-016-4018-8. arXiv: 1512.01178 [hep-ph].

[52] A. Gheata. "ALICE analysis framework". In: *PoS* ACAT08 (2008). Ed. by Thomas Speer, Federico Carminati, and Monique Werlen, p. 028. DOI: 10.22323/1.070.0028.

[53] Anders Ryd et al. "EvtGen: A Monte Carlo Generator for B-Physics". In: (May 2005).

[54]  Elisabetta Barberio and Zbigniew Was. "PHOTOS: A Universal Monte Carlo for QED radiative corrections. Version 2.0". In: *Comput. Phys. Commun.* 79 (1994), pp. 291–308. DOI: 10.1016/0010-4655(94)90074-4.

[55]  Souvik Das. "A simple alternative to the Crystal Ball function". In: (Mar. 2016). arXiv: 1603.08591 [hep-ex].

[56]  Shreyasi Acharya et al. "Coherent $J/\psi$ and $\psi'$ photoproduction at midrapidity in ultra-peripheral Pb-Pb collisions at $\sqrt{s_{\mathrm{NN}}}$ = 5.02 TeV". In: *Eur. Phys. J. C* 81.8 (2021), p. 712. DOI: 10.1140/epjc/s10052-021-09437-6. arXiv: 2101.04577 [nucl-ex].

# Appendix A

# Invariant Mass Fits for 2D Signal Extraction

The invariant mass fit was performed in bins chosen according to the limitation of the acceptance of the detector. The choice of binning is explained in Chapter 7. The following figures show fitted bins for signal extraction. Presented fits include only bins used for analysis excluding areas $\cos\theta \in (-0.5; 0.5) \cap \phi \in \left(\frac{\pi}{2}; \pi\right)$ and $\cos\theta \in (-0.5; 0.5) \cap \phi \in \left(\frac{3\pi}{2}; 2\pi\right)$ for the coherent photoproduction and $\cos\theta \in (-0.33; 0.33) \cap \phi \in \left(\frac{\pi}{2}; \pi\right)$ and $\cos\theta \in (-0.5; 0.5) \cap \phi \in \left(\frac{3\pi}{2}; 2\pi\right)$ for the incoherent photoproduction.
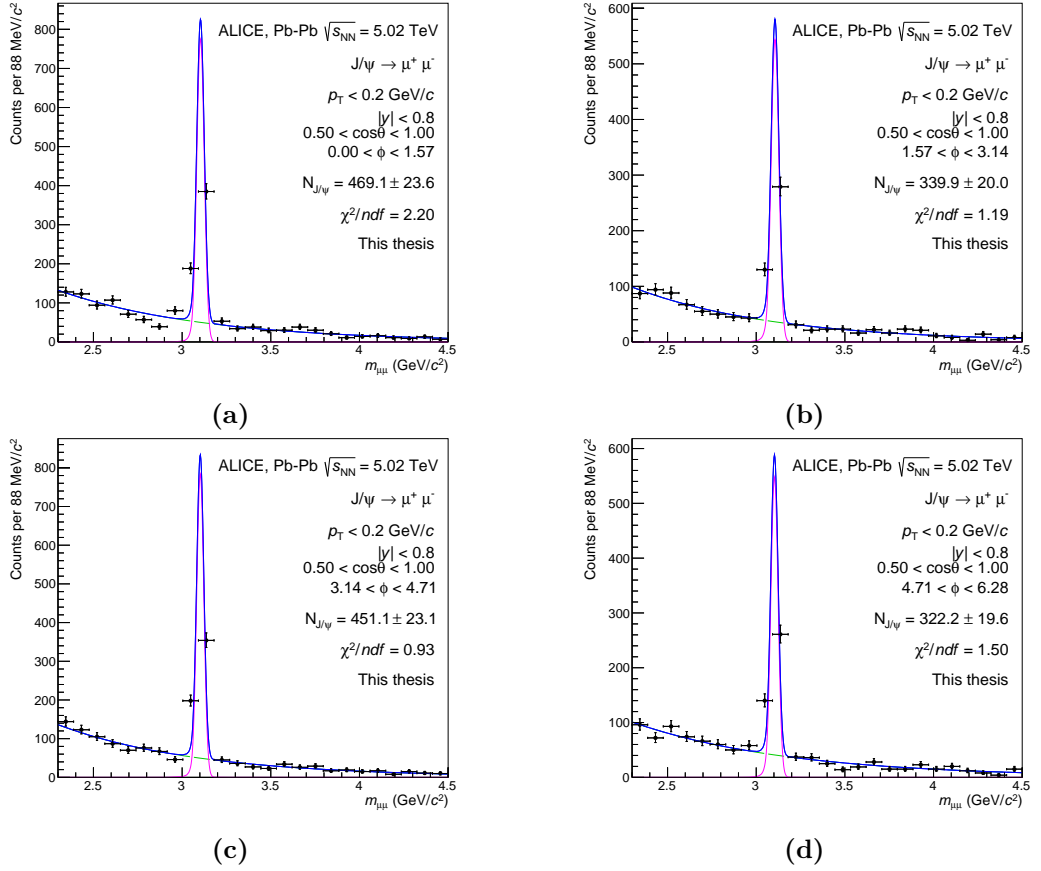
**(a)**



**(b)**



**(c)**



**(d)**
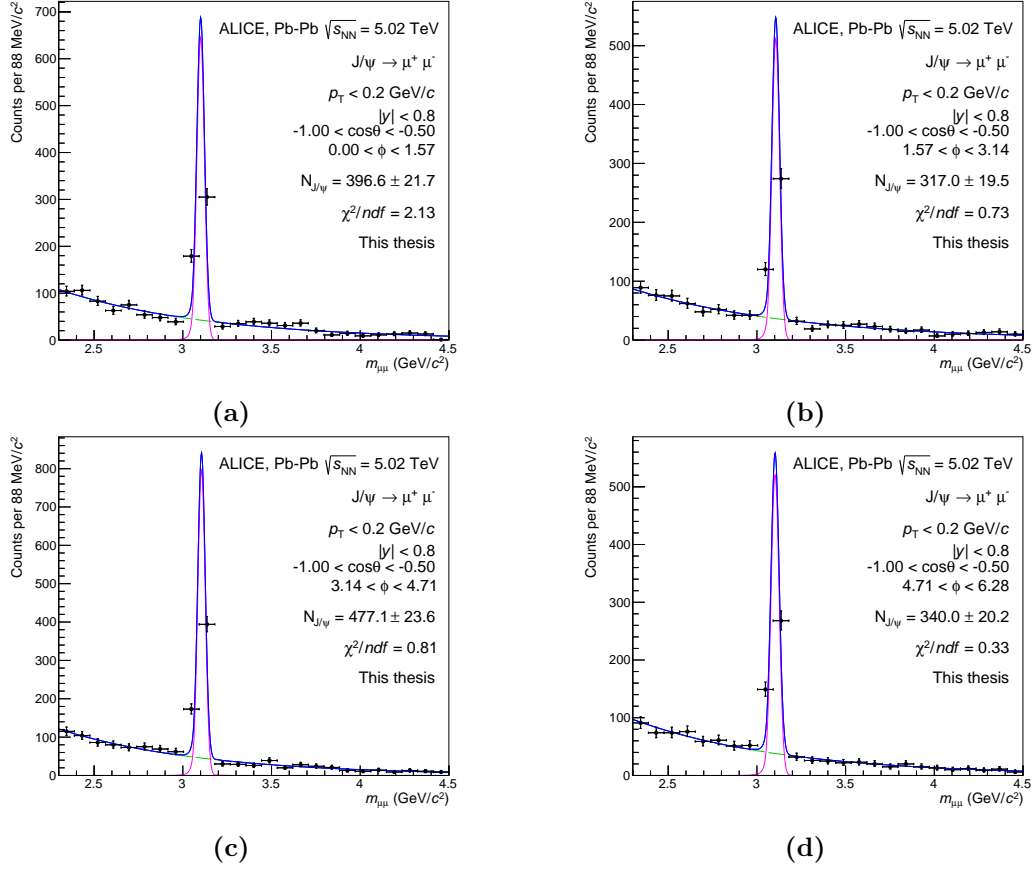
**Figure A.1:** Signal extraction for coherent photoproduction in $(-1.0; -0.5)\cos\theta$ bin and four bins in increasing $\phi$ from 0 to $\pi$ (a - d).
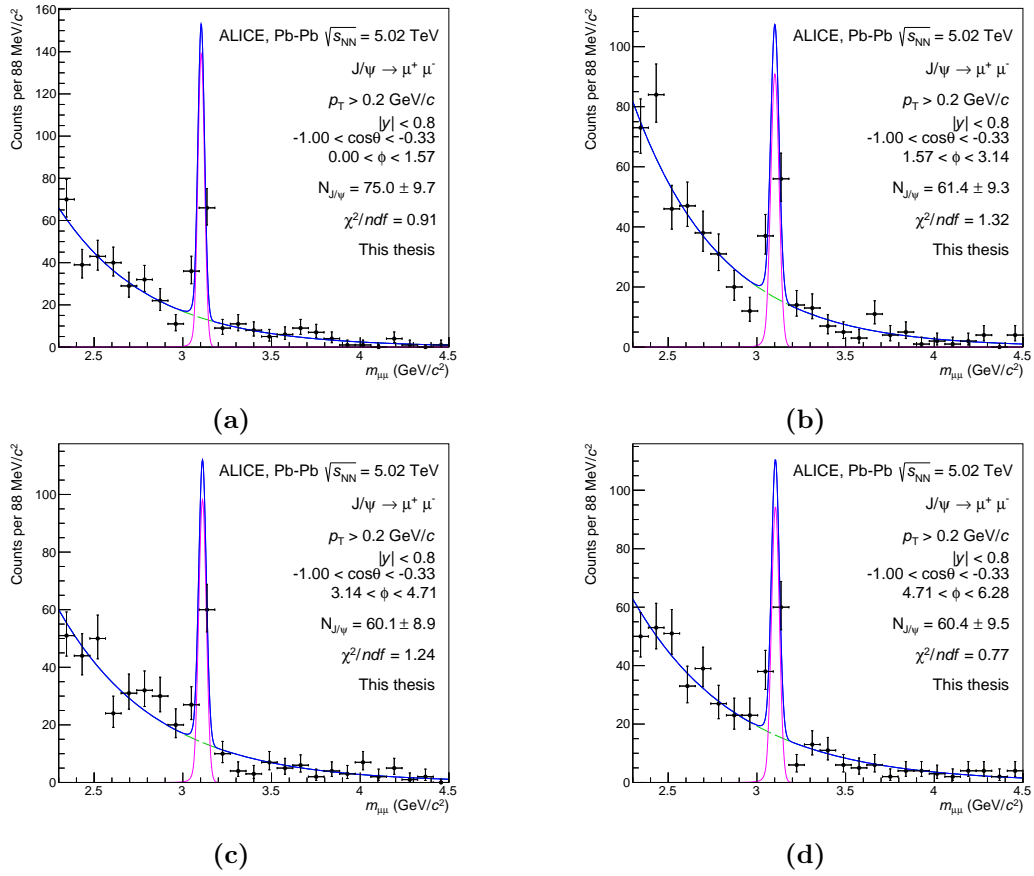


**(a)**



**(b)**
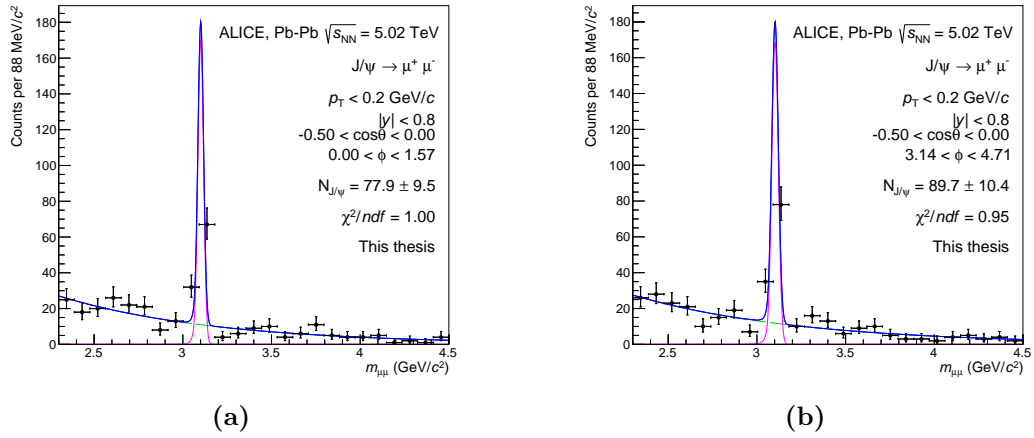
**Figure A.2:** Signal extraction for coherent photoproduction in $(-0.5; 0.0)\cos\theta$ bin and two bins for $\phi$ $(0; 0.5\pi)$ and $(\pi; 1.5\pi)$.
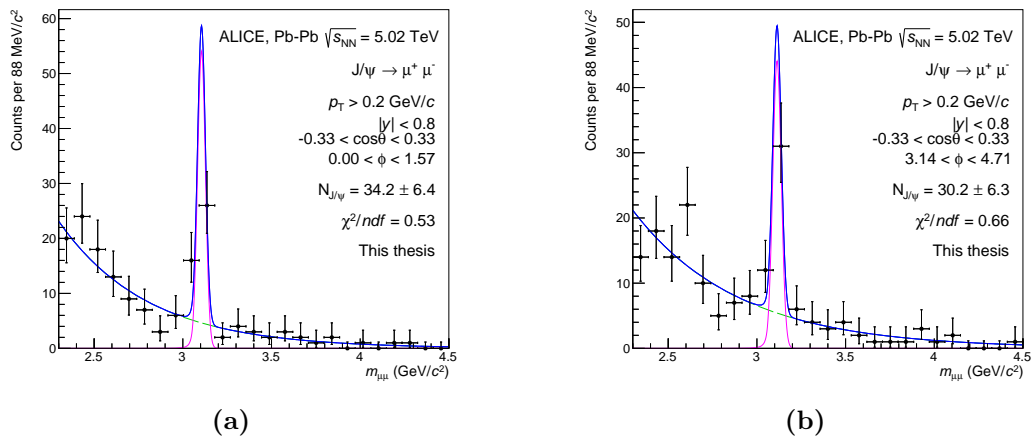
**(a)**           **(b)**
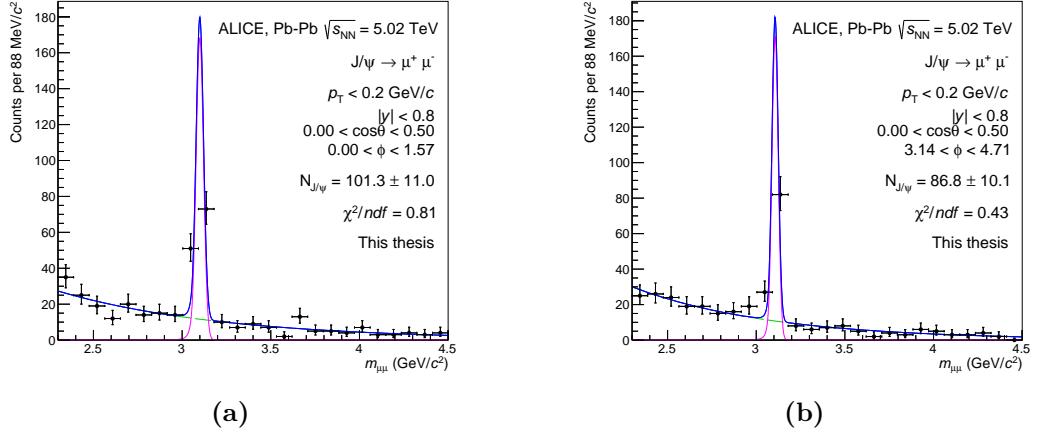
**Figure A.3:** Signal extraction for coherent photoproduction in $(0.0; 0.5)$ $\cos\theta$ bin and two bins for $\phi$ $(0; 0.5\pi)$ and $(\pi; 1.5\pi)$.



**(a)**           **(b)**
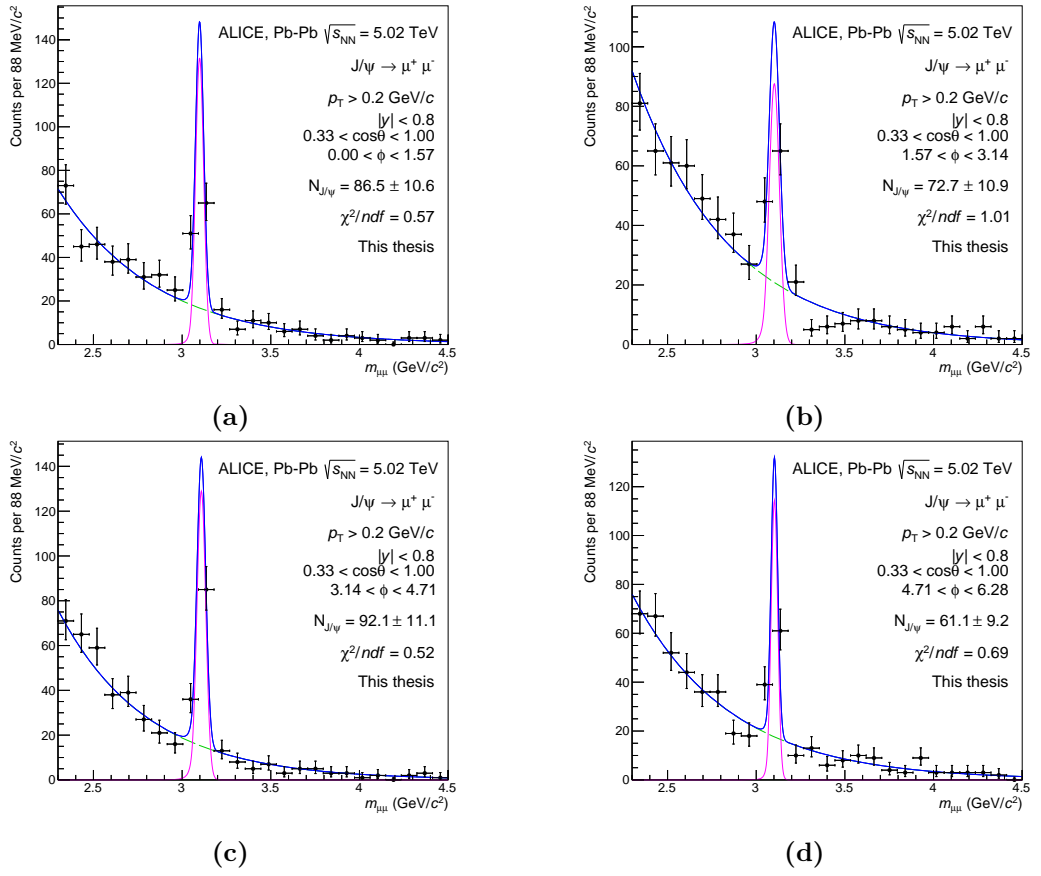
**(c)**           **(d)**

**Figure A.4:** Signal extraction for coherent photoproduction in $(0.5; 1.0)$ $\cos\theta$ bin and four bins in increasing $\phi$ from 0 to $\pi$ (a - d).

**(a)**



**(b)**



**(c)**



**(d)**

**Figure A.5:** Signal extraction for the incoherent photoproduction in $(-1.0; -0.33) \cos\theta$ bin and four bins in increasing $\phi$ from 0 to $\pi$ (a - d).



**(a)**



**(b)**

**Figure A.6:** Signal extraction for the incoherent photoproduction in $(-0.33; 0.33) \cos\theta$ bin and two bins for $\phi$ $(0; 0.5\pi)$ and $(\pi; 1.5\pi)$.

**Figure A.7:** Signal extraction for the incoherent photoproduction in $(0.33; 1.0) \cos\theta$ bin and four bins in increasing $\phi$ from 0 to $\pi$ (a - d).